Università degli Studi di Torino
Facoltá di Scienze Matematiche Fisiche e Naturali
Dipartimento di Fisica Teorica

Université de Savoie
École Doctorale - DCT Physique Théorique

Dottorato di Ricerca in Fisica Fondamentale, Applicata ed Astrofisica

CICLO XXI

NEUTRINO OSCILLATIONS IN GALLIUM AND REACTOR EXPERIMENTS AND COSMOLOGICAL EFFECTS OF A LIGHT STERILE NEUTRINO

Tesi prsentata da
Mario Andrés Acero Ortega

Relatore: Dott. Carlo Giunti
co-Relatore: Dott. Julien Lesgourgues

Contro Relatori: Dott. Thomas Schwetz
Dott. Sergio Pastor

Coordinatore del Dottorato: Prof. Stefano Sciuto

Anni Accademici: 2005 - 2008
Settore Scientifico-Disciplinare di Afferenza: FIS/02, FIS/05

"Try to imagine a spaceship that could pass right through the Earth without even noticing it was there; a spaceship that could cross the vastness of the space at the speed of light, and then penetrate into the very heart of subatomic matter to seek out its fundamental structure. Imagine, then, a particle that is almost nothing that can tell you almost everything about the structure of the matter and the evolution of the Universe. Impossible?."

From: *Spaceship neutrino*, by Christine Sutton.
Cambridge University Press, Cambridge (1992)

Publication type: Doctoral thesis.

Author: Mario Andrés Acero Ortega.

Title: Neutrino oscillations in Gallium and reactor experiments and cosmological effects of a light sterile neutrino.

Department: University of Turin, Theoretical Physics Department.

Advisors: Professor Carlo Giunti (INFN and U. Torino) and Professor Julien Lesgourgues (PH-TH CERN and EPFL).

Opponents: Professor Sergio Pastor (U. Valencia, IFIC.) and Professor Thomas Schwetz (MPI Heildelberg).

Defense: January 27, 2009.

Keywords: neutrino oscillations, sterile neutrino, neutrino cosmology.

ArXiv: xxxx.xxxx

ACKNOWLEDGMENTS

First of all, I thank my two advisors, Carlo Giunti and Julien Lesgourgues. Without them, this work would have not been possible. They really were guides for me during the last three years, they were very close to me and to the progress of my (our) work. I thank them for all their help, interest, patient and comprehension during the time I worked with them. They were much closer to me than I was expecting and it made me work much better and more confident. They were great Professors to me and I am very grateful for this.

Many thanks to Marco Laveder, who encouraged and helped me to complete an important part of my work. Also to Sergio Pastor and Thomas Schwetz, for taking part in the evaluation of this Thesis, as well as for their stimulant comments and suggestions.

My acknowledgments also to the *Università di Torino*, the International Doctorate of AstroParticle Physics (IDAPP), the *Laboratorie d'Annecy–le–Vieux de Physique Théorique* (LAPTH): the institutions which gave me the necessary resources to carry out my studies and my reseach work. In particular, the *Università di Torino* with its Scholarship program, which allowed me to live under good conditions during all the PhD period in the beautiful city of *Torino*. On the other hand, the IDAPP gave me the great opportunity of doing the PhD also with a French institution (*Université de Savoie*), an excellent opportunity to increase my experience and knowledge, to be in contact with a larger part of the world of Physics. Inside the IDAPP program I had the opportunity of visiting the LAPTH, where I met great people and I enjoyed a lot all the time I stayed there.

Many people were close to me during this time, helping to make better the life here. Living far form your home, far from your Family, becomes easy if good friends are around you, and I had the possibility of finding great people. Roberto, Hamed, Alejandra, Antonio, Mari, Georgia, Diogo, John, Darío, Carolina, Alessandro, Fabio, Paola, Camilo, Alberto, Sabine, John, Daniel..., and the list continues. Colleagues and not. Inside and outside research and academic life. *Friends*.

The most important part of my life: My Family. My parents, Mario and Stella; my brothers, Mauricio and Diego, and my sisters Paola and Johana; my little loved nephews, Nicolás and Samuel. They are my strongest impulse, my biggest love. Thanks to them, even being that far, I have been able to make my dreams real, I have been able to reach all my goals. Thanks to them I am finishing (also) this important phase of my life. Thanks to them I am giving another step in the long process I decided to follow long time ago. Thanks to them I am. Thanks to them, with my more sincere love.

Together to my family there has always been God. Our total support. Thanks to God, who has given me the power I always need in my studies, in my work, in my life. Thanks to God.

ABSTRACT

Neutrino oscillations is a very well studied phenomenon and the observations from Solar, very–long–baseline Reactor, Atmospheric and Accelerator neutrino oscillation experiments give very robust evidence of three-neutrino mixing.

On the other hand, some experimental data have shown anomalies that could be interpreted as indication of exotic neutrino physics beyond three-neutrino mixing. Furthermore, from a cosmological point of view, the possibility of extra light species contributing as a subdominant hot (or warm) component of the Universe is still interesting.

In the first part of this Thesis, we focused on the anomaly observed in the Gallium radioactive source experiments. These experiments were done to test the Gallium solar neutrino detectors GALLEX and SAGE, by measuring the electron neutrino flux produced by intense artificial radioactive sources placed inside the detectors. The measured number of events was smaller than the expected one.

We interpreted this anomaly as a possible indication of the disappearance of electron neutrinos and, in the effective framework of two-neutrino mixing, we obtained $\sin^2 2\theta \gtrsim 0.03$ and $\Delta m^2 \gtrsim 0.1\,\mathrm{eV}^2$.

We also studied the compatibility of this result with the data of the Bugey and Chooz reactor antineutrino disappearance experiments. We found that the Bugey data present a hint of neutrino oscillations with $0.02 \lesssim \sin^2 2\theta \lesssim 0.07$ and $\Delta m^2 \approx 1.95\,\mathrm{eV}^2$, which is compatible with the Gallium allowed region of the mixing parameters. Then, combining the data of Bugey and Chooz, the data of Gallium and Bugey, and the data of Gallium, Bugey and Chooz, we found that this hint persists, with an acceptable compatibility of the experimental data.

Furthermore, we analyzed the experimental data of the I.L.L., S.R.S, and Gösgen nuclear Reactor experiments.

We obtained a good fit of the I.L.L. data, showing 1 and 2σ allowed regions in the oscillation parameters space. However, the combination of I.L.L. data with the Bugey data showed a very low compatibility, so we did not use the I.L.L. data for additional analyses.

Abstract

Our fit of the S.R.S. experiment gave very small values of the goodness-of-fit, indicating that the data are incompatible with the oscillations hypothesis, as well as with the no oscillations hypothesis. We do not have any explanation for this result.

From the analysis of the Gösgen experiment, we obtained upper limits for the mixing parameters, excluding the region with $\sin^2 2\theta \geq 0.3$ and $\Delta m \geq 0.05$ eV^2 at 3σ C.L.. With the combination of these data with those of Gallium, Bugey and Chooz, we found that the hint of neutrino oscillations persists with $0.03 \lesssim \sin^2 2\theta \lesssim 0.07$ and $\Delta m^2 \approx 1.93$ eV^2, with a good compatibility of the data. However, the no oscillations hypothesis cannot be excluded.

Motivated by these results, in the second part of this work we studied cosmological constrains on a light non–thermal sterile neutrino.

We fitted up–to–date cosmological data with an extended ΛCDM model, including light relics with a mass in the range 0.1–10 eV. We obtained constrains on the current density and velocity dispersion of those relics, as well as constrains on their mass, assuming that they consist either of early decoupled thermal relics, or of non-resonantly produced sterile neutrinos. Our results are useful to constrain particle–motivated models with three active neutrinos and one extra light species.

We got, for instance, that at the 3σ confidence level, a sterile neutrino with mass $m_s = 2$ eV can be accommodated with the data provided that it is thermally distributed with $T_s/T_\nu^{\rm id} \lesssim 0.8$ (with $T_\nu^{\rm id}$ the temperature of neutrinos in the *instantaneous decoupling* limit), or is non-resonantly produced with $\Delta N_{\rm eff} \lesssim 0.5$. The bounds become dramatically tighter when the mass increases. For $m_s \lesssim 0.9$ eV and at the same confidence level, the data is still compatible with a standard thermalized neutrino.

RESUMEN

El fenómeno de Oscilación de neutrinos ha sido muy bien estudiado y las observaciones de los experimentos sobre oscilaciones de neutrinos Solares, de Reactores de longitud muy larga (*very–long–baseline Reactor*), Atmosféricos y de Aceleradores, dan evidencia muy robusta de mezcla de tres neutrinos.

Por otro lado, algunos datos experimentales han mostrado anomalías que se podrían interpretar como indicación de física de neutrinos exótica, más allá de la mezcla de tres neutrinos. Adicionalmente, desde un punto de vista cosmológico, todavía es interesante estudiar la posible existencia de especies livianas extra que contribuyan como una componente caliente (o cálida) subdominante del Universo.

En la primera parte de esta Tesis, se hace enfasis en la anomalía observada en los experimentos de Galio con fuente radioactiva. Estos experimentos se realizaron para probar los detectores de neutrinos solares GALLEX y SAGE, mediante la medición del flujo de neutrinos electrónicos producidos por fuentes radioactivas artificiales ubicadas en el interior de los detectores. El número de eventos medido fue menor que el esperado.

En el presente analisis, esta anomalía es interpretada como una posible indicación de la disaparición de neutrinos electrónicos y, en el contexto de mezcla de dos neutrinos, se obtiene una región permitida de los parametros de mezcla con $\sin^2 2\theta \gtrsim 0.03$ y $\Delta m^2 \gtrsim 0.1\,\mathrm{eV}^2$.

También se estudió la compatibilidad de este resultado con los datos de los experimentos sobre desaparición de antineutrinos electrńicos obtenidos en los reactores nucleares Bugey y Chooz. Se encontró que los datos de Bugey presentan una indicación de oscilación de neutrinos con $0.02 \lesssim \sin^2 2\theta \lesssim 0.07$ y $\Delta m^2 \approx 1.95\,\mathrm{eV}^2$, que es compatible con la región permitida de los parámetros de mezcla obtenida a partir del análisis de los experimentos de Galio. Además, con la combinación de los datos de Bugey y Chooz, de los datos de Galio y de Bugey y de los datos de Galio, Bugey y Chooz, esta indicación persiste, con una compatibilidad aceptable de los datos experimentales.

Adicionalmente, se alanizaron los datos provenientes de los experimentos de los Reactores nucleares I.L.L., S.R.S. y Gösgen.

El análisis de I.L.L. resultoó en un buen ajuste, mostrando regiones permitidas en el espacio de parametros de oscillación a 1 y 2σ, en favor de la oscilación de neutrinos. Sin embargo, la combinación de los datos de I.L.L. con los de Bugey presentan muy baja compatibilidad, por lo cual los resultados de I.L.L. no son usados en los demás análisis.

Del ajuste de los datos de S.R.S., se obtiene un valor muy pequeño para el parámetro *goodness-of-fit*, indicando que estos datos son incompatibles tanto con la hipoótesis de oscilaciones como con la de no oscilaciones de nuetrinos, resultado para el cual no se tiene ninguna explicación.

El análisis del experimento Gösgen arroja límites superiores para los parámetros de mezcla de neutrinos, excluyendo la región con $\sin^2 2\theta \geq 0.3$ y $\Delta m \geq 0.05$ eV^2 con 3σ C.L.. Al combinar estos datos con los de los experimentos de Galio, los de Bugey y los de Chooz, la pista en favor de oscilaciones de neutrinos se mantiene con $0.03 \lesssim \sin^2 2\theta \lesssim 0.07$ y $\Delta m^2 \approx 1.93$ eV^2, con una buena compatibilidad de los datos. No obstante, la hipótesis de no oscilaciones no puede ser descartada.

Motivados por estos resultados, en la segunda parte de este trabajo se estudian las restricciones cosmologicas sobre un neutrino estéril liviano no térmico.

Datos cosmológicos actualizados son ajustados con un modelo ΛCDM extendido, incluyendo reliquias livianas con masa en el rango 0.1–10 eV. Se obtuvieron restricciones de la densidad actual y de la velocidad de dispersión de estas reliquias, así como restricciones de su masa, asumiendo que éstas son formadas por reliquias térmicas tempranamente desacopladas, o por neutrinos estériles producidos no resonantemente. Estos resultados son útiles para restringir modelos de partículas con tres neutrinos activos y una especie liviana extra.

Por ejemplo, se obtuvo que, a un nivel de confianza de 3σ, un neutrino estéril con masa $m_s = 2$ eV se puede acomodar a los datos siempre que el mismo esté termalmente distribuído con $T_s/T_\nu^{\rm id} \lesssim 0.8$ (donde $T_\nu^{\rm id}$ es la temperatura de los neutrinos en el límite de *desacople instantaneo*), o sea producido no resonantemente con $\Delta N_{\rm eff} \lesssim 0.5$. Los límites se vuelven dramáticamente más fuertes cuando la masa aumenta. Para $m_s \lesssim 0.9$ eV y el mismo nivel de confianza, los datos siguen siendo compatibles con un neutrino estándar termalizado.

SINTESI

Le oscillazioni dei neutrini è un fenomeno ben studiato e le osservazioni degli sperimenti Solari, di Reattori, Atmosferici e di Acceleratori sulle oscillazione dei neutrini hanno fornito forte evidenza della mescola di tre neutrini.

Da l'altra parte, alcuni dati sperimentali hanno mostrato delle anomalie che potrebbero essere interpretate come un'indicazione di fisica di neutrini esotica al di là della mescola di tre neutrini. In più, da un punto di vista cosmologico, la possibile esistenza di specie leggere addizionale che contribuiscono come componente calda (o calida) sottodominante del Universo, è ancora interessante.

Nella prima parte di questa Tesi, ci concentriamo sulla anomalia osservata negli sperimenti di Gallio con sorgente radioattiva. Questi sperimenti furono fatti per provare i rivelatori di neutrini solari GALLEX e SAGE, il flusso di neutrini elettronici prodotto da sorgente artificiale radioattiva intensa localizzata all'interno dei rivelatori. Il numero d'eventi misurati è stato più piccolo dello aspettato.

Si interpreta questa anomalia come una possibile segnatura della sparizione de neutrini elettronici e, nel contesto di mescola di due neutrini, si ottiene $\sin^2 2\theta \gtrsim 0.03$ e $\Delta m^2 \gtrsim 0.1\,\mathrm{eV}^2$.

Si studia anche la compatibilità di questo risultato con i datti degli sperimenti su sparizione di antineutrini elettronici nei reattori Bugey e Chooz. Si trova che i dati di Bugey mostrano un indizio di oscillazione di neutrini con $0.02 \lesssim \sin^2 2\theta \lesssim 0.07$ e $\Delta m^2 \approx 1.95\,\mathrm{eV}^2$, il cuì è compatibile con la regione permesse dei parametri di mescola trovata nel analisi degli sperimenti di Gallio. Poi, combinando i dati di Bugey e Chooz, quelli di Gallio e Bugey, e quelli di Gallio, Bugey e Chooz, si trova che l'indizio rimane ancora, con una compatibilità accettabile tra i datti sperimentali.

In più, si studiano i dati degli sperimenti dei Reattori nucleari I.L.L., S.R.S. e Gösgen.

L'analisi dei dati del reattore I.L.L. mostra un buon fit, e si ottengono regioni permesse nello spazio di parametri delle oscillazioni ad 1 e 2σ. Tuttavia, la combinazione dei dati d'I.L.L. con quelli di Bugey mostrano una bassissima compatibilità, quindi

questi dati non vengono usati per altri analisi.

Il fit dello sperimento S.R.S. risulta in un valore del parametro *goodnes-of-fit* molto piccolo, il cui indica che i dati sono incompatibili sia con l'ipotesi di oscillazioni che con quella di non oscillazioni di neutrini. Non abbiamo nessuna spiegazione per questo comportamento dei dati.

Dal analisi dei dati di Gösgen si ottengono limiti superiori per i parametri di mescola di neutrini, escludendo la regione con $\sin^2 2\theta \geq 0.3$ e $\Delta m \geq 0.05$ eV^2 con 3σ C.L.. Con la combinazione dei dati di Gösgen con quelli di Gallio, Bugey e Chooz, si trova che l'indizio di l'oscillazione di neutrini rimane con $0.03 \lesssim \sin^2 2\theta \lesssim 0.07$ e $\Delta m^2 \approx 1.93$ eV^2, con una buona compatibilità dei dati. Comunque, l'ipotesi di non oscillazioni non può essere esclusa.

Incoraggiati da questi risultati, nella seconda parte di questo testo si studiano le restrizione cosmologiche su un neutrino sterile leggero non termale.

Si fittano dati cosmologici aggiornati con un modello ΛCDM esteso, aggiungendo reliquie leggere con massa nel rango 0.1–10 eV. Si ottengono delle restrizione sulla densità attuale e sulla velocità di dispersione di esse reliquie, così come restrizione sulla sua massa, assumendo che esse sono composte da reliquie termiche tempranamente disaccoppiate, oppure da neutrini sterili prodotti non resonantemente. Questi risultati sono utili per restringere modelli di particelle con tre neutrini attivi e una specie leggera addizionale.

Per esempio, si ottiene che, ad un livello di fiduccia di 3σ, un neutrino sterile con massa $m_s = 2$ eV può essere accomodato ai datti a condizione che esse sia termalmente distribuito con $T_s/T_\nu^{\rm id} \lesssim 0.8$ ($T_\nu^{\rm id}$ essendo la temperatura dei neutrini nel limite di disaccoppio istantaneo), oppure che esse sia prodotto non resonantemente con $\Delta N_{\rm eff} \lesssim 0.5$. I limiti si tornano dramaticamente più forti col incremento della massa. Per $m_s \lesssim 0.9$ eV e lo stesso livello di fiduccia, i datti sono ancora compatibili con un neutrino termalizato standard.

RÉSUMÉ

Neutrino oscillations est trés bien étudié le phénomène et des observations de Solar, très–long–base de référence du réacteur, l'atmosphère et d'accélérateur à l'oscillation des neutrinos expériences très robuste donner la preuve de trois mélange des neutrinos.

D'autre part, certaines données expérimentales ont montré des anomalies qui pourraient être interprétées comme indication de la physique des neutrinos exotique au-delà de trois mélange des neutrinos. En outre, à partir d'un point de vue cosmologiques, la possibilité d'espèces extra léger comme une contribution subdominant chaud de l'Univers est toujours intéressant.

Dans la première partie de cette thèse, nous nous sommes concentrs sur l'anomalie observée dans le Gallium source radioactive expériences. Ces expériences ont été réalisées pour tester la Gallium détecteurs de neutrinos solaires GALLEX et SAGE, en mesurant le flux de neutrinos d'électrons produit par une intense des sources radioactives artificielles placées à l'intérieur de détecteurs. Le mesurée certain nombre d'événements a été inférieur à celui attendu.

Nous avons interprété cette anomalie comme une indication possible de la disparition de neutrinos et d'électrons, dans le cadre efficace de deux de mélange des neutrinos, nous avons obtenu $\sin^2 2\theta \gtrsim 0.03$ et $\Delta m^2 \gtrsim 0.1\,\mathrm{eV}^2$.

Nous avons également étudié la compatibilité de ce rsultat avec les donnes de le réacteur Bugey et de Chooz antineutrino disparition expériences. Nous avons constaté que les données Bugey présente un indice d'oscillations de neutrinos à $0.02 \lesssim \sin^2 2\theta \lesssim 0.07$ et $\Delta m^2 \approx 1.95\,\mathrm{eV}^2$, qui est compatible avec le permis de Gallium de la rgion paramtres de mixage. Puis, en combinant les données de Bugey et de Chooz, les données de Gallium et de Bugey, et les données de Gallium, le Bugey et de Chooz, nous avons constaté que ce soupçon persiste, avec une certaine compatibilité des données expérimentales.

En outre, nous avons analysé les données expérimentales de l'ILL, SRS, Gösgen et expériences réacteur nucléaire.

Nous avons obtenu un bon ajustement de la I.L.L. données, en montrant 1 et 2σ

permis régions de l'espace des paramètres d'oscillation. Toutefois, la combinaison de I.L.L. données avec le Bugey les données ont révélé un très faible compatibilité, si nous n'avons pas utilisé l'ILL données pour les analyzes supplémentaires.

Notre ajustement de la S.R.S. expérience a donn de très petites valeurs de la qualité d'ajustement (*goodness-of-fit*), ce qui indique que les données sont incompatibles avec l'hypothèse d'oscillations, ainsi que les oscillations aucune hypothèse. Nous n'avons pas d'explication à ce résultat.

De l'analyze de la Gösgen expérience, nous avons obtenu des limites supérieures pour les paramètres de mélange, à l'exclusion de la rgion avec $\sin^2 2\theta \geq 0.3$ et $\Delta m \geq 0.05$ eV^2 à 3σ C.L.. Grâce à la combinaison de ces données avec celles de Gallium, le Bugey et de Chooz, nous avons constaté que l'indice des oscillations de neutrinos persiste à $0.03 \lesssim \sin^2 2\theta \lesssim 0.07$ et $\Delta m^2 \approx 1.93$ eV^2, avec une bonne compatibilité des données. Toutefois, les oscillations aucune hypothèse ne peut être exclue.

Motivé par ces résultats, dans la deuxième partie de ce travail nous avons étudié contraintes cosmologiques sur une lumière non–thermique neutrino stérile.

Nous aménagées—la date des données cosmologiques avec une longue ΛCDM, y compris en lumière les vestiges d'une masse dans la gamme 0.1–10 eV. Nous avons obtenu des contraintes sur la densité de courant et de la vitesse de dispersion de ces reliques, ainsi que des contraintes sur leur masse, à supposer qu'elles consistent soit découplé de la petite thermique des reliques, ou de non-resonantly produit stérile neutrinos. Nos résultats sont utiles pour peser sur des particules–motivés avec trois modèles de neutrinos actifs et un très léger espèces.

Nous avons, par exemple, que lors de la 3σ niveau de confiance, un neutrino stérile de masse $m_s = 2$ eV peuvent être logés avec les données à condition qu'il soit distribué avec thermiquement $T_s/T_\nu^{\rm id} \lesssim 0.8$ (avec $T_\nu^{\rm id}$ de la température de neutrinos dans le répertoire limite *instantane dcouplage*), est ou non resonantly produits avec $\Delta N_{\rm eff} \lesssim 0.5$. Les limites deviennent plus strictes de façon spectaculaire lorsque la masse augmente. Pour $m_s \lesssim 0.9$ eV et au même niveau de confiance, les données est toujours compatible avec une norme thermique de neutrinos.

CONTENTS

CHAPTER 1

INTRODUCTION

And Wolfang Pauli said:
Let there be Neutrinos!
And Enrico Fermi said:
Let them interact weakly!
And the sun began to shine!

Herbert Pietscmann [1]

It was Wolfgang Pauli the one who proposed the existence of Neutrinos in 1930 (he actually called them *neutrons*[1] [3]), to save the law of energy conservation and as an explanation of the observed β-spectrum in the β-decay process.

It was only in 1956, in the Savannah River Experiment conducted by F. Reines and C. Cowan, when for the first time, a neutrino signal was detected (see [4, 5]).

In 1959, the first ideas on neutrino oscillations appeared, suggested by Bruno Pontecorvo [6] in analogy to the Kaon oscillatory system. The phenomenon of neutrino oscillations is an indication of new physics beyond the Standard Model of Particle Physics, because it implies that neutrinos have a mass different from zero.

Neutrino oscillations, since that time, is an important topic of research in Physics and big efforts have been done looking for experimental evidence of this phenomenon. This evidence has arrived from a series of experiments (see section 2.3.2) which observed oscillations of neutrinos produced in the Sun and in the Atmosphere, and with the results of Accelerator and Reactor neutrino experiments, neutrino oscillations were confirmed.

[1] "(...), the possibility that in the nuclei there could exist electrically neutral particles, which I will call neutrons, that have spin 1/2 and obey the exclusion principle and that further differ from light quanta in that they do not travel with the velocity of light. (...)I admit that my remedy may seem almost improbable because one probably would have seen those neutrons, if they exist, for a long time." [2]

In this Thesis, we consider the Gallium radioactive source experiments, performed to test the Gallium detectors used in Solar neutrino experiments. They measured a number of events smaller that spected and this deficit can be interpreted as an indication of the disappearance of electron neutrinos as a result of neutrino oscillations. We analyze this anomalous result in the framework of two-neutrino mixing. We also test the compatibility of this hypothesis with the Bugey and Chooz nuclear reactor experiments.

Neutrinos have also played a relevant role in important processes during the evolution of the Universe. Considering the experimental evidence on neutrino oscillations (indicating neutrinos are massive), we know that at least two neutrino states have a large enough mass for being non-relativistic today, making up a small fraction of the dark matter of the Universe.

Here we present the study of the compatibility of cosmological experimental data (WMAP5 plus small-scale CMB data, SDSS LRG data, SNIa data from SNLS and Lya data from VHS) with the hypothesis of a non-thermal sterile neutrino with a mass of the order of the electron-Volts and with a small contribution to the effective number of neutrino species.

The Thesis is organized as follows: in Chapter 2 the basics of Neutrino physics are presented, with short review of the ingredients of the Standard Model of particle Physics concerning Neutrinos, as well as the phenomena of neutrino oscillations and mixing.

Chapter 3 contains the description of the Gallium radioactive and the Bugey and Chooz nuclear Reactor experiments, together with the method used in our analysis. In the last section of the Chapter, we present the main results of the study.

Motivated by the results of Chapter 3, after an introduction to the relevant rôle played by neutrinos in Cosmology, in Chapter 5 we present the study of the compatibility of cosmological experimental data with the hypothesis of a light non-thermal sterile neutrino, and a small contribution to the relativistic density (parametrized by an effective neutrino number $N_{\rm eff}$). A summary is presented at the end of the chapter.

Finally, in Chapter 6 we present the general conclusions of the Thesis.

CHAPTER 2

NEUTRINO PHYSICS

Neutrino Physics is largely an art of learning a great deal by observing nothing.

Haim Harari

In this chapter, the fundamentals of neutrino physics are described, presenting the characteristics of neutrinos inside the Standard Model of Particle Physics (SM), the important phenomena of neutrino oscillations and mixing, the introduction and effects of neutrino masses, and the most relevant experimental evidence on neutrinos.

2.1 The Standard Model

The Standard Model of Particle Physics (SM) [7, 8] is a very successful theory which explains the strong, electromagnetic and weak interactions of the different particles which are the matter constituents. The SM does this in the framework of Quantum Field Theory, and based on the symmetry group $SU(3)_C \times SU(2)_L \times U(1)_Y$, where C, L, and Y are for *color*, *left handed chirality* and *weak hypercharge*, respectively. This gauge group has a total of 12 generators (8 for $SU(3)_C$, 3 for $SU(2)_L$ and 1 for $U(1)_Y$), which have a correspondence with the vector gauge bosons that mediate the interactions mentioned above (8 massless gluons, 3 massive and 1 massless -$W^{\pm}$, Z, γ- bosons). The gauge group $SU(3)_C \times SU(2)_L \times U(1)_Y$ is spontaneously broken to $SU(3)_C \times U(1)_{\rm em}$ through the *Higgs mechanism* [9, 10, 11, 12, 13], giving the physical masses to the particles (see tables 2.1 and 2.2).

Inside the SM, the fundamental fermions are organized in three *families* with the only difference being the masses. Taking, for example, the first family, the structure is as follow:

$$\begin{pmatrix} \nu_e \\ e \end{pmatrix}_L, \quad e_R; \qquad \begin{pmatrix} u_i \\ d_i \end{pmatrix}_L, \quad u_{iR}, \quad d_{iR} \quad (i = 1, 2, 3). \tag{2.1}$$

Particle	Mass	Charge	Particle	Mass	Charge
u	$1.5 - 3.0$ MeV	$2/3$	e	0.511 MeV	-1
d	$3.0 - 7.0$ MeV	$-1/3$	ν_e	< 2.2 eV	0
s	95 ± 25 MeV	$-1/3$	μ	105.66 MeV	-1
c	1.25 ± 0.09 GeV	$2/3$	ν_μ	< 190 keV	0
b	4.20 ± 0.07 GeV	$-1/3$	τ	1.777 GeV	-1
t	174.2 ± 3.3 GeV	$2/3$	ν_τ	< 18.2 MeV	0

Table 2.1: Mass and charges of the spin-1/2 particles (quarks and leptons) in the SM [14, 15].

Particle	Spin	Mass	Charge
Higgs h	0	> 114.4 GeV	0
$W^\pm$	1	80.403 ± 0.029 GeV	± 1
Z^0	1	91.1876 ± 0.0021 GeV	0
γ	1	$< 6 \times 10^{-17}$ eV	0
$G^a (a = 1, ..., 8)$	1	0	0

Table 2.2: Mass and charges of the bosons in the SM [14].

Note that there is not a right handed neutrino. This is the way the SM was constructed from the very beginning, because neutrinos were considered to be massless. However, there is now evidence saying that neutrinos have (even if tiny) masses different from zero. In such a case, a right handed neutrino component could be included here, although it is not completely necessary, as we will see in section 2.2.

The neutrino SM interactions are described by the leptonic charged current (CC)

$$j^\beta_{W,L} = 2 \sum_{\alpha=e,\mu,\tau} \overline{\nu_{\alpha L}} \gamma^\beta l_{\alpha L} = \sum_{\alpha=e,\mu,\tau} \overline{\nu_\alpha} \gamma^\beta \left(1 - \gamma_5\right) l_\alpha, \tag{2.2}$$

and the leptonic neutral current (NC)

$$j^\beta_{Z,\nu} = \sum_{\alpha=e,\mu,\tau} \overline{\nu_{\alpha L}} \gamma^\beta \nu_{\alpha L} = \frac{1}{2} \sum_{\alpha=e,\mu,\tau} \overline{\nu_\alpha} \gamma^\beta \left(1 - \gamma_5\right) \nu_\alpha. \tag{2.3}$$

These currents take part in the leptonic CC and NC weak interaction Lagrangians, respectively

$$\begin{aligned} \mathcal{L}^{(CC)}_L &= -\frac{g}{2\sqrt{2}} \left(j^\beta_{W,L} W_\beta + (j^\beta_{W,L})^\dagger (W_\beta)^\dagger \right), \\ \mathcal{L}^{(NC)}_\nu &= -\frac{g}{2\cos\theta_W} j^\rho_{Z,\nu} Z_\rho. \end{aligned} \tag{2.4}$$

Charged and neutral current scattering are important interactions for the study of neutrinos, because those are the processes used to their detection (for example

$\nu_e + {}^{71}\mathrm{Ga} \rightarrow {}^{71}\mathrm{Ge} + e^-$, used in Gallium solar neutrino experiments). In addition, neutrino detection is also performed through elastic scattering processes as $\nu + e^- \rightarrow \nu + e^-$.

2.2 Masses of neutrinos

Since the very beginning of neutrino physics, with its proposal by Pauli, the investigation of neutrino masses is a very important and active research topic, from the theoretical and the experimental point of view. Neutrinos were suggested to be massless particles or to have a very small mass, smaller than the electron one. However, there is important experimental evidence that neutrinos are massive (measurement of solar and atmospheric neutrino fluxes and measurements from terrestrial experiments are explained by the neutrino oscillation phenomena, which requires neutrinos to be massive). In some theories which unify the strong, weak and electromagnetic interactions (grand unified theories, GUT) massive neutrino arise naturally (see for example [16, 17]). Certainly, massiveness of neutrinos is one of the most important manifestations of the necessity and existence of Physics Beyond the SM. See references [15, 18, 19, 20, 21] for a deeper review on neutrino masses.

Unfortunately, we do not know yet the scale of the neutrino masses; currently, we only know two squared-mass difference values coming from solar ($\Delta m^2_{\mathrm{sol}} = (7.59 \pm 0.21) \times 10^{-5}$ eV^2 [22]) and atmospheric ($\Delta m^2_{\mathrm{atm}} = (2.74^{+0.44}_{-0.26}) \times 10^{-3}$ eV^2 [23]) neutrino experiments. Limits on the neutrino mass can be obtained from different experiments:

- the *beta decay*, by observing the end-point part of the electrum spectrum in the Tritium β decay, with an upper limit of 2.2 eV at 95% C.L. for the effective mass $m_\beta = \sqrt{\sum_k |U_{ek}|^2 m_k^2}$ [24] (see also [25]);

- measuring the half-life of *neutrinoless double beta decay*, $0\nu\beta\beta$ (see for example [26, 27, 28, 29]), which is inversely proportional to the effective neutrino mass squared $\langle m \rangle^2 = \left(\sum_{i=1} U_{ei}^2 m_i\right)^2$, with m_i the mass of a Majorana neutrino. Recent results from NEMO-3 [30], on $0\nu\beta\beta$, have found $\langle m \rangle < (1.5 - 2.5)$eV and $\langle m \rangle < (4.0 - 6.3)$eV, depending on the procedure to compute the nuclear matrix elements [31];

- from cosmological measurements there are constrains on the sum of the neutrino masses due to their effect on the propagation of perturbations, on the clustering of matter, and on the expansion rate of the Universe. For instance, the five-year WMAP (Wilkinson Microwave Anisotropy Probe) [32] data gives the upper limit $\sum m_\nu < 1.3$ eV at 95% C.L. [33, 34]; however, it is important to remark that constrains from Cosmology are very dependent on the used data sets as well as on the cosmological model and the considerations on the number of neutrino species (see [35, 36, 37, 38, 39, 40, 41]).

In the SM, the absence of right-handed neutrinos prevent the writing and existence

of Dirac neutrino masses, and without Higgs triplets it is not possible to have Majorana neutrino masses.

Many ideas have been worked out extending the SM in order to include neutrino masses and to explain its origin (see reference [42]). One of the most accepted and implemented ways to do it successfully, is through the so call *see-saw mechanism* [43, 44, 45], in which neutrino masses are considered as low-energy manifestation of physics beyond the SM, and their smallness comes from a suppression generated by a new high-energy scale.

Neutrinos can be constructed to have either Dirac or Majorana masses, as well as the most general Dirac-Majorana mass type.

2.2.1 Dirac masses

Dirac neutrino masses are generated through the same Higgs mechanism used to give masses to the other leptons in the SM, by including right-handed components of the neutrino fields, $\nu_{\alpha R}$. These right-handed neutrino fields are invariant under the symmetries of the SM, that means they are singlets of $SU(3)_C \times SU(2)_L$ and have hypercharge $Y = 0$. In other words, the right-handed neutrino fields have the characteristic that, unlike left-handed neutrino fields, they do not take part in the weak interactions. This is the reason why right-handed neutrino fields are called *sterile*.

In the Minimal Extended Standard Model with three right-handed neutrino fields the Dirac neutrino mass term is

$$\mathcal{L}_D = -\overline{\nu_L}\, M_D\, \nu_R + \text{h.c.}, \tag{2.5}$$

where the right-handed neutrino is

$$\nu_R \equiv \begin{pmatrix} \nu_{eR} \\ \nu_{\mu R} \\ \nu_{\tau R} \end{pmatrix}, \tag{2.6}$$

working in the base in which the charged leptons mass matrix is diagonal. The matrix M_D can be diagonalized by,

$$V_L^{\nu\dagger} M_D V_R^{\nu} = M_D^{\nu}, \qquad \text{with} \qquad M_{Dij}^{\nu} = m_i^{\nu}\delta_{ij} \quad (i,j=1,2,3), \tag{2.7}$$

with real and positive m_i^{ν} and with unitary V_L, V_L. Then, the chiral massive neutrino arrays can be defined as

$$\mathbf{n}_L = \begin{pmatrix} \nu_{1L} \\ \nu_{2L} \\ \nu_{3L} \end{pmatrix}, \qquad \mathbf{n}_R = \begin{pmatrix} \nu_{1R} \\ \nu_{2R} \\ \nu_{3R} \end{pmatrix}, \tag{2.8}$$

so that the diagonalized Dirac neutrino mass terms become

$$\begin{aligned} \mathcal{L}_D &= -\overline{\mathbf{n}_L}\, M_D^{\nu}\, \mathbf{n}_R + \text{h.c.}, \\ &= -\sum_{k=1}^{3} m_k^{\nu}\, \overline{\nu_{k\,L}}\, \nu_{k\,R} + \text{h.c.} \end{aligned} \tag{2.9}$$

Finally, with the use of the Dirac neutrino fields

$$\nu_k \equiv \nu_{kL} + \nu_{kR}, \quad (k = 1, 2, 3), \tag{2.10}$$

one gets

$$\mathcal{L}_D = -\sum_{k=1}^{3} m_k \, \overline{\nu_k} \nu_k \tag{2.11}$$

2.2.2 Majorana masses

All the charged fermions are Dirac particles as a consequence of electric charge conservation. On the other hand, neutrinos could also be Dirac particles, but as they are chargeless, there is also the possibility that they are Majorana particles.

To derive the Majorana mass term, let us consider a Dirac neutrino $\nu = \nu_L + \nu_R$, and its Dirac mass term,

$$\mathcal{L}^D_{\text{mass}} = -m\overline{\nu}\nu = -m\left(\overline{\nu_R}\nu_L + \overline{\nu_L}\nu_R\right), \tag{2.12}$$

where we have used the relations $P_L\nu_L = \frac{1}{2}(1-\gamma_5)\nu_L = \nu_L$ and $P_R\nu_L = \frac{1}{2}(1+\gamma_5) = 0$ (P_L and P_R are the left-handed and right-handed projectors, respectively).

In order to write a Majorana mass term, it is necessary to get an expression using only ν_L, for which it is useful to use the *charge conjugated* field

$$\nu_L^C = \mathcal{C}\,\overline{\nu_L}^T, \tag{2.13}$$

which is a right-handed field.

ν_L^C has the correct properties to replace ν_R in equation (2.12), giving the Majorana mass term

$$\mathcal{L}^M_{\text{mass}} = -\frac{1}{2} m \overline{\nu_L^C} \nu_L + \text{h.c.}, \tag{2.14}$$

which can also be written as

$$\mathcal{L}^M_{\text{mass}} = -\frac{m}{2}\left(-\nu_L^T \mathcal{C}^\dagger \nu_L + \overline{\nu_L}\mathcal{C}\overline{\nu_L}^T\right). \tag{2.15}$$

2.2.3 Dirac-Majorana masses

If there exist N_s sterile (right-handed) neutrino fields ν_{sR}, in addition to the three active left-handed neutrino fields we know, the most general mass term is the *Dirac-Majorana mass term*, given by

$$\mathcal{L}^{D+M}_{\text{mass}} = \mathcal{L}^L_{\text{mass}} + \mathcal{L}^R_{\text{mass}} + \mathcal{L}^D_{\text{mass}}, \tag{2.16}$$

with two Majorana mass terms

$$\mathcal{L}^L_{\text{mass}} = \frac{1}{2} \sum_{\alpha,\beta=e,\mu,\tau} \nu^T_{\alpha L}\, \mathcal{C}^\dagger\, M^L_{\alpha\beta}\, \nu_{\beta L} + \text{h.c.}, \tag{2.17}$$

$$\mathcal{L}^R_{\rm mass} = \frac{1}{2} \sum_{s,s'=s_1,\cdots s_{N_s}} \nu^T_{sR}\, \mathcal{C}^\dagger\, M^R_{ss'}\, \nu_{s'R} + \text{h.c.}, \tag{2.18}$$

and the Dirac mass term

$$\mathcal{L}^D_{\rm mass} = \sum_{s=s_1,\cdots s_{N_s}} \sum_{\alpha=e,\mu,\tau} \overline{\nu_{sR}}\, M^D_{s\alpha}\, \nu_{\alpha L} + \text{h.c.}. \tag{2.19}$$

The left-handed Majorana mass matrix M^L is a symmetric 3×3 square matrix, the right-handed Majorana mass matrix M^R is a symmetric $N_s \times N_s$ square matrix and the Dirac mass matrix M^D is a $N_s \times 3$ rectangular matrix.

In a similar way as it is done for the Dirac mass term, it is useful to define the column matrix

$$\mathbf{N}_L \equiv \begin{pmatrix} \boldsymbol{\nu}_L \\ \boldsymbol{\nu}^C_R \end{pmatrix}, \tag{2.20}$$

of $3 + N_s$ rows, with the column matrix of three left-handed active neutrinos

$$\boldsymbol{\nu}_L \equiv \begin{pmatrix} \nu_{eL} \\ \nu_{\mu L} \\ \nu_{\tau L} \end{pmatrix}, \tag{2.21}$$

and the column matrix of N_s right-handed sterile neutrinos

$$\boldsymbol{\nu}^C_R \equiv \begin{pmatrix} \nu^C_{s_i R} \\ \vdots \\ \nu^C_{s_{N_s} R} \end{pmatrix}. \tag{2.22}$$

Then, the Dirac-Majorana mass term becomes

$$\mathcal{L}^{D+M}_{\rm mass} = \frac{1}{2}\, \mathbf{N}^T_L\, \mathcal{C}^\dagger\, M^{D+M}\, \mathbf{N}_L + \text{h.c.}, \tag{2.23}$$

with the symmetric mass matrix

$$M^{D+M} \equiv \begin{pmatrix} M^L & (M^D)^T \\ M^D & M^R \end{pmatrix}. \tag{2.24}$$

For the diagonalization of the Dirac-Majorana mass term, the left-handed field is written as linear combinations of the left-handed components of N fields of definite mass as

$$\mathbf{N}_L = V^\nu_L \mathbf{n}_L, \qquad \mathbf{n}_L = \begin{pmatrix} \nu_{1L} \\ \vdots \\ \nu_{NL} \end{pmatrix}, \tag{2.25}$$

such that the matrix V_L^ν diagonalize the mass matrix:

$$(V_L^\nu)^T \; M^{D+M} \, V_L^\nu = M, \quad \text{with} \quad M_{ij} = m_i \delta_{ij} \qquad (i,j = 1,2,\cdots,N), \tag{2.26}$$

and m_i real an positive. Then, the Dirac-Majorana mass term in equation (2.23) can be written as

$$\mathcal{L}_{\text{mass}}^{D+M} = \frac{1}{2} \, \mathbf{n}_L^T \, \mathcal{C}^\dagger \, M \, \mathbf{n}_L + \text{h.c.} = \frac{1}{2} \sum_{i=1}^{N} m_i \nu_{iL}^T \, \mathcal{C}^\dagger \, \nu_{iL} + \text{h.c.}. \tag{2.27}$$

Note that, as a result of the diagonalization of the Dirac-Majorana mass term, massive neutrinos are Majorana particles.

2.3 Neutrino Oscillations and Mixing

The first ideas on neutrino oscillations and mixing were proposed by Bruno Pontecorvo in 1957 [6], thinking that for leptons there could be a phenomenon analogous to $K^0 - \bar{K}^0$ oscillations. Since that time only the electron-neutrino was known, to develop his thoughts, Pontecorvo invented the concept of *sterile* neutrino. After 1962, when the muon-neutrino was discovered, it was understood that oscillations between different active neutrino flavors are possible if neutrinos are massive and mixed. Later on, the first model of mixing of different flavors was presented and the Solar Neutrino Problem was explained, as a result of $\nu_e \to \nu_\mu$ (or $\nu_e \to \nu_{\text{sterile}}$) transitions.

In the standard theory of neutrino oscillations, a neutrino with flavor α and momentum $\overrightarrow{p}$, identified through its charged current interactions, is described by the flavor state

$$|\nu_\alpha\rangle = \sum_i V_{\alpha i}^* |\nu_i\rangle, \qquad \alpha = e, \mu, \tau. \tag{2.28}$$

The coefficients $V_{\alpha i}$ come from the contribution of the massive neutrinos in the lepton charged current.

It is important to remark that, in equation (2.28), the sum has not an upper limit, meaning that there is the possibility to have more than three massive neutrinos, with the further consequence that the additional neutrinos in the flavor state must be sterile.

Concerning massive neutrino states, they are eigenstates of the Hamiltonian

$$\mathcal{H}|\nu_i\rangle = E_i |\nu_i\rangle, \tag{2.29}$$

with energy eigenvalues $E_i = \sqrt{|\overrightarrow{p}|^2 + m_i^2}$. Their evolution in time, dictated by the Schrödinger equation, is given by the plane wave

$$|\nu_i(t)\rangle = \exp(-iE_i t)|\nu_i\rangle. \tag{2.30}$$

Then, the time evolution of a flavor state is got by replacing (2.30) into (2.28):

$$\begin{aligned} |\nu_\alpha(t)\rangle &= \sum_i V^*_{\alpha i}|\nu_i(t)\rangle \\ &= \sum_i V^*_{\alpha i}\exp(-iE_i t)|\nu_i(t=0)\rangle \end{aligned} \tag{2.31}$$

Using the unitarity of the mixing matrix ($\mathbf{V}^\dagger\mathbf{V} = \mathbf{1}$), a neutrino mass eigenstate can be expressed as a superposition of flavor states,

$$|\nu_i\rangle = \sum_\alpha V_{\alpha i}|\nu_\alpha\rangle, \tag{2.32}$$

so that the evolution of a flavor state, equation (2.31), is

$$\begin{aligned} |\nu_\alpha(t)\rangle &= \sum_i \left[V^*_{\alpha i}\exp(-iE_i t)\left(\sum_\beta V_{\beta i}|\nu_\beta\rangle\right)\right] \\ &= \sum_{\beta=e,\mu,\tau}\left(\sum_i V^*_{\alpha i}\exp(-iE_i t)V_{\beta i}\right)|\nu_\beta\rangle. \end{aligned} \tag{2.33}$$

Equation (2.33), implies that the superposition of massive neutrino states $|\nu_\alpha(t)\rangle$ (see equation (2.28) $|\nu_\alpha\rangle = |\nu_\alpha(t=0)\rangle$)), becomes a superposition of different flavor states at $t > 0$[1].

Furthermore, equation (2.33) also gives the amplitude of $\nu_\alpha \to \nu_\beta$ transition, corresponding to the coefficient of $|\nu_\beta\rangle$, as a function of time:

$$\mathcal{A}_{\nu_\alpha\to\nu_\beta}(t) \equiv \langle\nu_\beta|\nu_\alpha(t)\rangle = \sum_i V^*_{\alpha i}V_{\beta i}\exp(-iE_i t), \tag{2.34}$$

and the transition probability results to be

$$P_{\nu_\alpha\to\nu_\beta}(t) = \left|\mathcal{A}_{\nu_\alpha\to\nu_\beta}(t)\right|^2 = \sum_{i,k} V^*_{\alpha i}V_{\beta i}V_{\alpha k}V^*_{\beta k}\exp[-i(E_i - E_k)t]. \tag{2.35}$$

Considering that neutrinos are ultrarelativistic, the energy difference in (2.35) is

$$\begin{aligned} E_i - E_k &= \sqrt{|\overrightarrow{p}|^2 + m_i^2} - \sqrt{|\overrightarrow{p}|^2 + m_k^2} \\ &\simeq |\overrightarrow{p}|\left(1 + \frac{m_i^2}{2|\overrightarrow{p}|^2}\right) - |\overrightarrow{p}|\left(1 + \frac{m_k^2}{2|\overrightarrow{p}|^2}\right) \\ &\simeq \frac{m_i^2 - m_k^2}{2E} \\ \Rightarrow E_i - E_k &= \frac{\Delta m^2_{ik}}{2E}, \end{aligned} \tag{2.36}$$

[1]This is true if the mixing matrix V is not diagonal, which means neutrinos are mixed [15].

where $E = |\overrightarrow{p}|$ is the neutrino energy neglecting the mass contribution, and

$$\Delta m^2_{ik} = m^2_i - m^2_k. \tag{2.37}$$

Then, the transition probability becomes

$$P_{\nu_\alpha \to \nu_\beta}(t) = \sum_{i,k} V^*_{\alpha i} V_{\beta i} V_{\alpha k} V^*_{\beta k} \exp\left[-i \frac{\Delta m^2_{ik}}{2E} t\right]. \tag{2.38}$$

Experiments studying neutrino oscillations do not measure the time of propagation, but what is known is the distance between the neutrino source and the detector, L. Given that neutrinos travel almost at the speed of light, and using natural units ($c = 1$), then $L = t$, so

$$P_{\nu_\alpha \to \nu_\beta}(L) = \sum_{i,k} V^*_{\alpha i} V_{\beta i} V_{\alpha k} V^*_{\beta k} \exp\left[-i \frac{\Delta m^2_{ik} L}{2E}\right]. \tag{2.39}$$

Equation (2.39) shows that the phases of the neutrino oscillations depend on the source-detector distance L, the neutrino energy E, and on the square-mass differences Δm^2_{ik}. On the other hand, the amplitude of the oscillations depends on the elements of the neutrino mixing matrix V.

Let us emphasize that, even though neutrino oscillations are a clear signature of the existence of neutrino masses, this is a phenomenon which is not able to give information about the absolute value of the neutrino masses, but only about the values of Δm^2_{ik}.

In the case of antineutrinos, the flavor state is written as

$$|\overline{\nu}_\alpha\rangle = \sum_i V_{\alpha i} |\overline{\nu}_i\rangle, \qquad \alpha = e, \mu, \tau, \tag{2.40}$$

which differs from the neutrino state in the coefficients, $V_{\alpha i}$, by the complex conjugate operation.

However, kinematical properties governing the transition probability of antineutrinos, $\overline{\nu}_\alpha \to \overline{\nu}_\beta$, are the same as the ones described before for the case of neutrinos. Then, the computation of the transition probability as a function of time follows the same steps, and the only consideration in order is the complex conjugation in the coefficients of the states. Therefore, from equation (2.39), taking the complex conjugate of the mixing matrix elements, the transition probability for antineutrinos is

$$P_{\overline{\nu}_\alpha \to \overline{\nu}_\beta}(L) = \sum_{i,k} V_{\alpha i} V^*_{\beta i} V^*_{\alpha k} V_{\beta k} \exp\left[-i \frac{\Delta m^2_{ik} L}{2E}\right]. \tag{2.41}$$

Note that if, in the last equation, α and β are interchanged, the transition probability becomes

$$P_{\overline{\nu}_\beta \to \overline{\nu}_\alpha}(L) = \sum_{i,k} V_{\beta i} V^*_{\alpha i} V^*_{\beta k} V_{\alpha k} \exp\left[-i \frac{\Delta m^2_{ik} L}{2E}\right], \tag{2.42}$$

which coincides with the expression for the oscillation probability for neutrinos, equation (2.39), showing that

$$P_{\nu_\alpha \to \nu_\beta} = P_{\overline{\nu}_\beta \to \overline{\nu}_\alpha}. \tag{2.43}$$

This is a result coming from the fact that the theory of neutrino oscillations is formulated in the framework of a local quantum field theory, which imples that the *CPT* transformation

$$\nu_\alpha \to \nu_\beta \quad \underset{\longleftrightarrow}{\text{CPT}} \quad \overline{\nu}_\beta \to \overline{\nu}_\alpha, \tag{2.44}$$

is a symmetry of the oscillation probabilities. Equality (2.43) also suggests that the survival probabilities[2] of neutrinos are equal to those of antineutrinos:

$$P_{\nu_\alpha \to \nu_\alpha} = P_{\overline{\nu}_\alpha \to \overline{\nu}_\alpha}, \tag{2.45}$$

a very important equality for the analysis presented in this Thesis.

2.3.1 Two neutrino mixing

An interesting approximation is the case of two neutrino mixing, for which it is easy to compute the corresponding transition probability, using the results presented in the previous section. Two neutrino mixing approximation is important and useful, because its description depends on less parameters than the three-(or more) neutrino mixing, and because in practice it allows an effective description of experimental data.

Considering two flavor neutrino states, ν_α and ν_β, which are linear superpositions of two massive neutrino states ν_1 and ν_2, the corresponding mixing matrix can be written as

$$V = \begin{pmatrix} \cos\theta & \sin\theta \\ -\sin\theta & \cos\theta \end{pmatrix}, \tag{2.46}$$

where θ is the mixing angle. Then, it is clear that

$$\begin{aligned} V_{\alpha 1} &= \cos\theta, & V_{\alpha 2} &= \sin\theta, \\ V_{\beta 1} &= -\sin\theta, & V_{\beta 2} &= \cos\theta. \end{aligned} \tag{2.47}$$

In addition, in the two neutrino mixing framework, there is only one square-mass difference:

$$\Delta m^2 \equiv \Delta m^2_{21} = m^2_2 - m^2_1. \tag{2.48}$$

In this way, replacing the corresponding elements of the mixing matrix in equation (2.39), the probability of $\nu_\alpha \to \nu_\beta$ transition is

$$\begin{aligned} P_{\nu_\alpha \to \nu_\beta}(L,E) &= \frac{1}{2}\sin^2 2\theta \left[1 - \cos\left(\frac{\Delta m^2 L}{2E}\right)\right] \\ &= \sin^2 2\theta \, \sin^2\left(\frac{\Delta m^2 L}{4E}\right). \end{aligned} \tag{2.49}$$

[2]The survival probability can be understood as the oscillation probability of the channel with $\alpha = \beta$ in, for instance, equation (2.39).

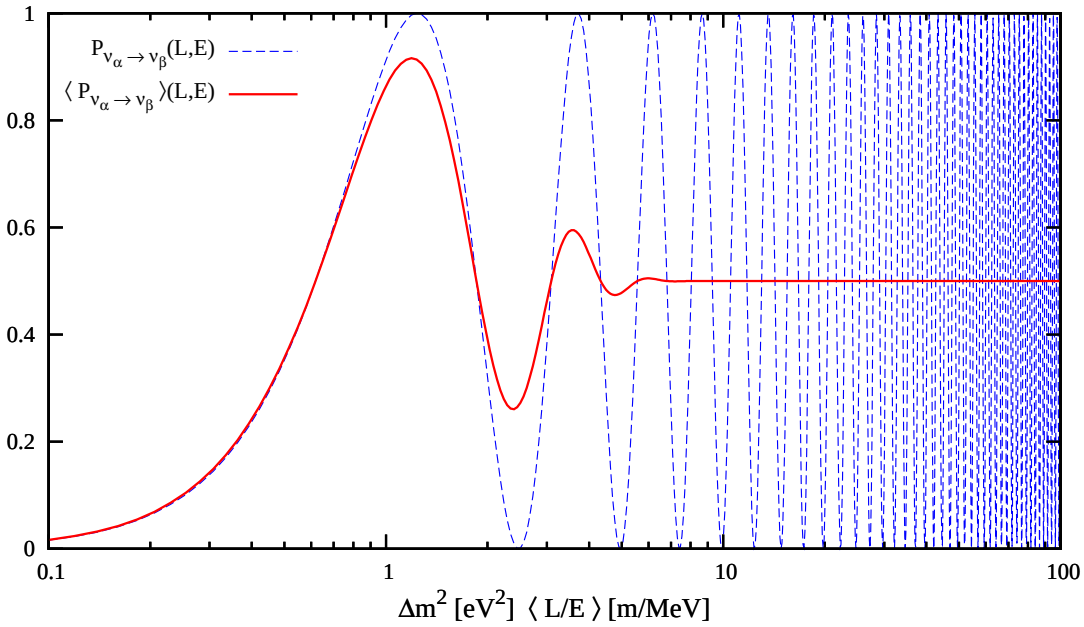

Figure 2.1: Probability of $\nu_\alpha \to \nu_\beta$ transition for $\sin^2 2\theta = 1$, as a function of $(L[\mathrm{m}]/E[\mathrm{MeV}])\Delta m^2[\mathrm{eV}^2]$.

For $\alpha = \beta$, the survival probability is obtained:

$$\begin{aligned} P_{\nu_\alpha \to \nu_\alpha}(L,E) &= 1 - P_{\nu_\alpha \to \nu_\beta}(L,E) \\ &= 1 - \sin^2 2\theta \, \sin^2\left(\frac{\Delta m^2 L}{4E}\right). \end{aligned} \tag{2.50}$$

Concerning the analyses of neutrino oscillation experimental data, it is better to write the transition probability in such a way to account for the convenient units and magnitudes of the involved quantities:

$$P_{\nu_\alpha \to \nu_\beta}(L,E) = \sin^2 2\theta \, \sin^2\left(1.27\frac{\Delta m^2[\mathrm{eV}^2] L[\mathrm{m}]}{E[\mathrm{MeV}]}\right). \tag{2.51}$$

Figure 2.1 shows the behavior of the transition probability (dashed-blue line) as a function of $L[\mathrm{m}]/E[\mathrm{MeV}]\Delta m^2[\mathrm{eV}^2]$, together to the transition probability averaged over a Gaussian L/E distribution with $\sigma_{L/E} = 0.2\langle L/E \rangle$ (red-solid line), for $\sin^2 2\theta = 1$.

The oscillation length

$$L_{\mathrm{osc}} = \pi \frac{E[\mathrm{MeV}]}{1.27\Delta m^2[\mathrm{eV}^2]} = 2.47\frac{E[\mathrm{MeV}]}{\Delta m^2[\mathrm{eV}^2]}, \tag{2.52}$$

corresponds to the position of the first dip of the transition probability, at $\frac{L[\mathrm{m}]\Delta m^2[\mathrm{eV}^2]}{E[\mathrm{MeV}]} = 2.47$, as show in the figure. For small distances $L \ll L_{\mathrm{osc}}$, the transition is very small, while it oscillates rapidly for $L \gg L_{\mathrm{osc}}$.

On the other hand, for distances $\langle L \rangle \lesssim L_{\mathrm{osc}}$, the average transition probability[3] has a very similar behavior to the unaveraged one, with a suppression depending on $\sigma_{L/E}$ (the larger the value of $\sigma_{L/E}$, the bigger the suppression); for $\langle L \rangle \gg L_{\mathrm{osc}}$, the oscillations are totally suppressed and it is only possible to measure the average transition probability [15],

$$\langle P_{\nu_\alpha \to \nu_\beta}(L, E) \rangle = \frac{1}{2} \sin^2 2\theta. \tag{2.53}$$

2.3.2 Experimental evidence

From the moment when neutrino physics was born, very intense effort have been done to understand the behavior, characteristics and participation of this particle inside many fields in physics, going from the smallest structures (in High Energy Particle and Nuclear Physics) to the very large scale of the Universe (Cosmology and Astrophysics). Hence, the great importance of neutrino detection and experiments.

The difficult task of detecting neutrinos was overcame in 1956, when Reines and Cowan [4] detected for the first time reactor antineutrinos by observing the inverse β-decay, in which an antineutrino produces a positron. From that moment, a large number of experiments have been proposed and realized in order to increase the knowledge and understanding of neutrino physics.

Oscillation experiments, can be divided into two classes:

- **Appearance experiments**, in which measurement of transitions between different neutrino flavors is done.

- **Disappearance experiments**, in which the survival probability of a neutrino flavor is measured. The interactions in the detector are counted and compared to the theoretical predictions or to a measurement of the initial neutrino flux, looking for an attenuation this.

Neutrino oscillations can be evidenced in terrestrial experiments, as well as in experiments which are sensitive to neutrinos coming from astrophysical sources. The Homestake experiment [46] was the first one to detect the large flux of neutrinos coming from the Sun, and observe the deficit of electron solar neutrinos with respect to the Standard Solar Model prediction. This *solar neutrino problem* was shown to be due to $\nu_e \to \nu_\mu, \nu_\tau$ transitions, by the SNO experiment [47]. The reactor long-baseline KamLAND experiment found that these transitions are the result of neutrino oscillations [48].

[3] It is necessary to average the transition probability over the experimental uncertainties of L and E.

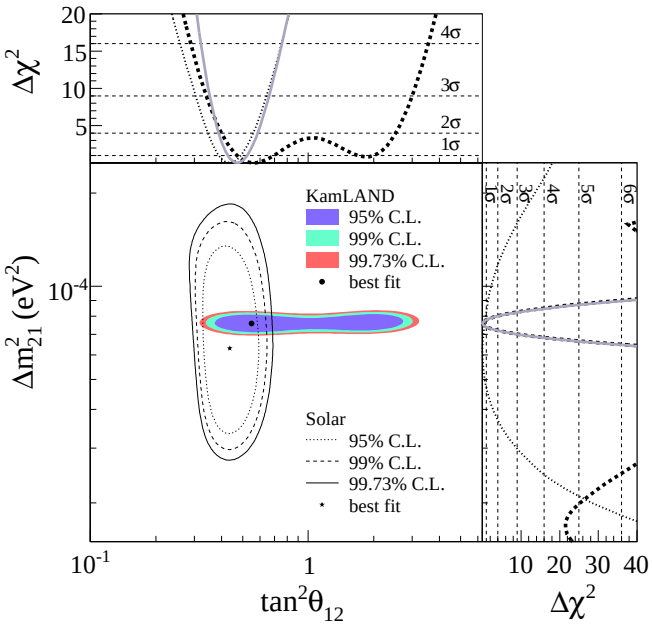

Figure 2.2: Allowed region for neutrino oscillation parameters from KamLAND and solar neutrino experiments [22].

KamLAND data and solar neutrino data are well fitted by effective two-neutrino oscillations, including MSW effects of neutrino propagation in matter [49, 50], with the solar square-mass difference and mixing angle [22]

$$\Delta m^2_{\rm sol} = (7.59 \pm 0.21) \times 10^{-5}{\rm eV}^2, \qquad \tan^2 2\theta_{\rm sol} = 0.47^{+0.06}_{-0.05}. \tag{2.54}$$

Figure 2.2 shows the allowed regions in the oscillation parameter space obtained from KamLAND data and the data of solar neutrino experiments (Homestake [46], GALLEX/GNO [51], SAGE [52], Super-Kamiokande [53], SNO [54], Borexino [55]).

In the 1980s, the Kamiokande [56] and IBM [57] experiments discovered the atmospheric anomaly, and in 1998 the Super-Kamiokande experiment found a model independent evidence of muon (anti)neutrino disappearance in atmospheric neutrino data [58]. Atmospheric neutrinos are produced by the interaction of primary cosmic rays (mainly protons) with the nuclei in the atmosphere. Super-Kamiokande observed that the muon neutrino deficit is zenith-angle[4] dependent. The zenith angle asymmetry is quantified by the ratio

$$A_\mu^{\text{up-down}} = \frac{U - D}{U + D}, \tag{2.55}$$

[4]The zenith angle θ is the angle between the direction of the reconstructed path of the charged lepton and the vertical of the detector; then, vertically down-going particles correspond to $\cos\theta = 1$.

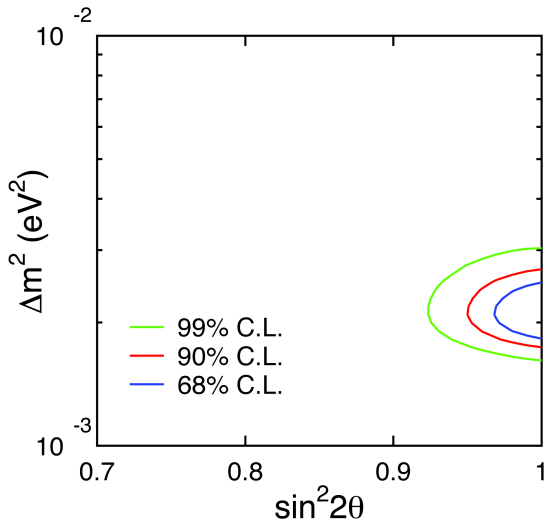

Figure 2.3: Allowed region in the oscillation parameter space for $\nu_\mu \to \nu_\tau$ oscillations obtained by the analysis of Super-Kamiokande experimental results. The best fit is located at $\sin^2 2\theta = 1.02$ and $\Delta m^2 = 2.1 \times 10^{-3}$ eV^2 [59].

where U and D are the contained muon- or electron-like events with zenith angle in the range $-1 < \cos\theta < 0.2$ and $0.2 < \cos\theta < -1$, respectively. The value presented by the Super-Kamiokande collaboration is

$$A_\mu^{\text{up-down}} = -0.296 \pm 0.048 \pm 0.01, \tag{2.56}$$

for muon-like events, while the corresponding electron up-down asymmetry was consistent with zero ($A_e^{\text{up-down}} = -0.036 \pm 0.067 \pm 0.02$) [58]. Considering that the source-detector distance covered by upward-going neutrinos is much larger than that covered by downward-going neutrinos, the asymmetry (2.56) is consistent with the hypothesis of neutrino oscillations. The analysis of the Super-Kamiokande most recent results [59] are presented in the figure 2.3. These results have been confirmed by the independent observations of muon (anti)neutrino disappearance in the accelerator long-baseline experiments K2K [60] and MINOS [61], with the same values of the mixing parameters. From MINOS data (see figure 2.4) [61],

$$\Delta m^2_{\text{atm}} = (2.43 \pm 0.13) \times 10^{-3}\text{eV}^2, \qquad \sin^2 2\theta_{\text{atm}} > 0.90(90\%\text{C.L.}). \tag{2.57}$$

2.4 Sterile Neutrinos

As already mentioned before, the SM is constructed in such a way that the particle spectrum is divided in three families. For each of these families, there is the corresponding neutrino, as a "partner" of the charged leptons, i.e., *electron*, *muon* and *tau*

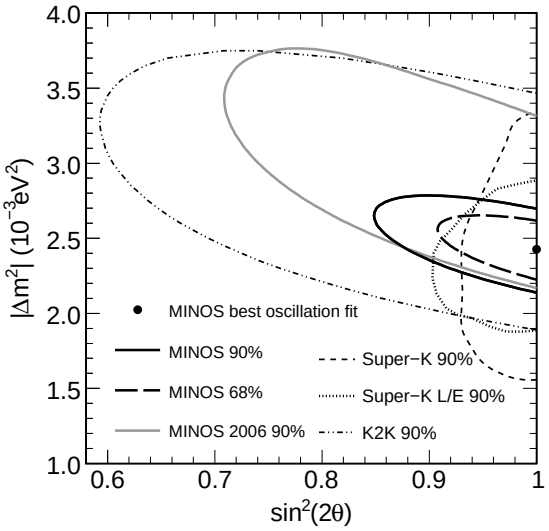

Figure 2.4: Allowed region of the oscillation parameters using the MINOS results, and compared to other experiment results [61].

neutrinos. These are so-called active neutrinos, meaning that they take part in weak interactions.

Furthermore, the experimental evidence coming from LEP precision electroweak measurements [62], points to the fact that the number of light neutrinos (those with $m < m_Z/2$) which couple with the Z boson through electroweak interaction is 2.984 ± 0.008 [62, 63], such that there is no open window for additional active neutrinos.

Let us remark that the possibility of existing *sterile neutrinos* is still open. For *sterile* is understood that those neutrinos do not participate in electroweak interactions and then, they do not contribute to the Z decay.

From a theoretical point of view, looking at the structure of the fundamental fermions (2.1), there is a clear difference between quarks and leptons: there is the right-handed neutrino missing (one per family). Right-handed neutrinos ν_R are sterile with respect to the SM gauge interactions [64]. As explained in section 2.2, the inclusion of right-handed neutrinos makes neutrinos naturally massive particles, allowing the presence of Dirac and Majorana mass terms.

Different experiments have set important and severe restrictions on the participation of sterile neutrinos in the oscillation phenomena observed in solar and atmospheric neutrino data, without ruling it out totally. The LSND (Liquid Scintillator Neutrino Detector) experiment [65] found an evidence of $\overline{\nu}_\mu \to \overline{\nu}_e$ oscillation with $\Delta m^2 = 0.2 - 10\text{eV}^2$ [66]. In order to fit this result together with the results from Solar and Atmospheric neutrino oscillation experiments (equations (2.54) and (2.57), respectively), it would be necessary to have an extra sterile neutrino. However, recent results from MiniBooNe [67], have not found evidence of oscillations in the same (L/E_ν) range, disfavoring the LSND results.

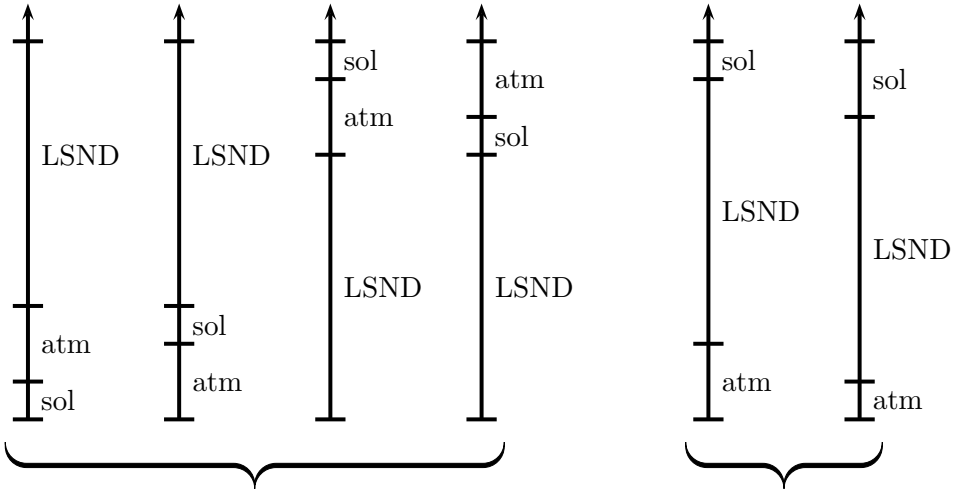

Figure 2.5: The different types of four-neutrino mass spectra [69].

If a Δm^2 value different from the two well known solar and atmospheric Δm^2 values is confirmed, the simplest extension of the SM is to include one sterile neutrino to the neutrino spectra. In this way, it is possible to accommodate the three square-mass differences ($\Delta m^2_{\rm sol}$, $\Delta m^2_{\rm atm}$, $\Delta m^2_{\rm LSND}$) in two different mass-spectra scenarios satisfying $\Delta m^2_{\rm sol} \ll \Delta m^2_{\rm atm} \ll \Delta m^2_{\rm LSND}$ [68]. As shown in figure 2.5, in the first scenario, denominated **(3+1)**, there is a group of three close masses separated from the fourth mass by the LSND gap; while in the second scenario, **(2+2)**, there are two pairs of close masses separated by the LSND gap.

Phenomenological analysis of four-neutrino mixing have already disfavored the (3+ 1) mass schemes [70, 69] by the incompatibility between LSND results and short-base line (SBL) disappearance experiments. The tension becomes stronger with the inclusion of the MiniBooNE (MB) results [71]. As can be seen in figure 2.6, there is only a marginal overlapping between the SBL bound and the LSND allowed region, taking both at 99%CL (left panel), which actually disappears with the inclusion of information from disappearance experiments and MB [71] (right panel).

On the other hand, $(2 + 2)$ schemes are found to be ruled out by constraints on a sterile neutrino component in solar and atmospheric neutrino oscillations [69].

Nevertheless, four-neutrino mixing is not the only possibility. The addition of one sterile neutrino is the *simplest* extension of the standard model in the field of neutrino oscillations, but it is possible to add more than one sterile neutrinos. For instance, the authors of reference [72], have found $(3 + 2)$ schemes can provide a good (better than $(3+1)$) description of the data coming from short-baseline experiments combined with LSND.

However, in this Thesis, the LSND and MiniBooNE results are not considered. Instead, we focused on Gallium radioactive source experiments and nuclear reactor

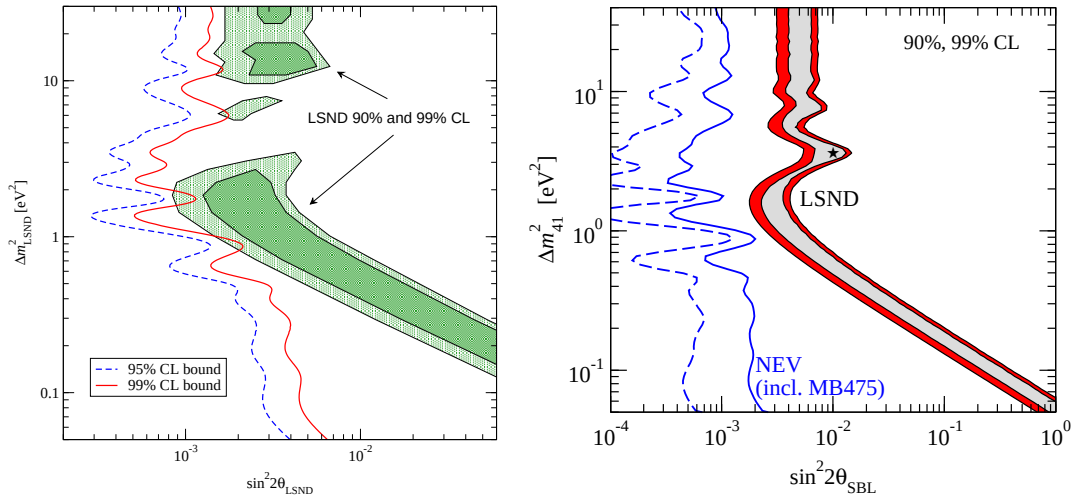

Figure 2.6: *Left.* LSND allowed region compared with bounds on $\sin^2(2\theta)$ from SBL experiments, for the (3+1) scheme [69]. *Right.* The same, with the inclusion of MB data and information from disappearance experiments [71].

experiments, which are explained in the next chapter.

CHAPTER 3

ANALYSIS OF THE GALLIUM RADIOACTIVE SOURCE EXPERIMENTS AND BUGEY AND CHOOZ REACTOR EXPERIMENTS

As presented in the previous chapter, the observation of solar and reactor neutrino oscillations due to the square-mass difference $\Delta m^2_{\rm sol} = (7.59 \pm 0.21) \times 10^{-5}\,{\rm eV}^2$ [22] and the observation of atmospheric and accelerator neutrino oscillations due to the square-mass difference $\Delta m^2_{\rm atm} = (2.43 \pm 0.13 \times 10^{-3}) \times 10^{-3}\,{\rm eV}^2$ [61] give very robust evidence of three-neutrino mixing.

In this chapter, we consider the Gallium radioactive source experiments anomaly [73] which could be interpreted as indications of exotic neutrino physics beyond three-neutrino mixing. A description of these experiments is presented, as well as the analysis of the observed anomaly, under the hypothesis of the disappearance of electron neutrinos due to neutrino oscillations [74, 75, 76] in the framework of two neutrino mixing. We also discuss the compatibility of this interpretation of the Gallium radioactive neutrino experiments anomaly, with the results of the Bugey and Chooz nuclear reactor neutrino experiments, including a short description of each experiment.

3.1 Gallium radioactive source experiments

Radiochemical detection is one of the methods used for detecting neutrinos. In this method, a detector chemical interacts with neutrinos converting the initial element into a radioactive isotope of another element,

$$\nu_e + N(A, Z-1) \rightarrow e^- + N(A, Z), \tag{3.1}$$

where Z is the atomic number and A the mass number. The atoms of the radioactive product are extracted and counted by using chemical techniques. This count gives a measure of the neutrino flux [77].

Radiochemical experiment using Gallium nuclei were proposed initially in [78] to detect *pp solar neutrinos* using the reaction

$$\nu_e + {}^{71}\mathrm{Ga} \longrightarrow e^- + {}^{71}\mathrm{Ge}, \tag{3.2}$$

with a threshold energy $E_\nu^{\mathrm{th}} = 0.233$ MeV.

The experiment was carried out by the GALLEX [79, 80, 81] and SAGE [82, 83, 84, 73] groups, measuring a lower flux of electron neutrinos that that expected from the Solar Standard Model (SSM), result which is explained with the phenomenon of neutrino oscillations.

This results have important consequences in particle physics and astrophysics, so it is very important to test carefully the experimental techniques, to cancel any possible doubt on them and on the results. The most straightforward check is to expose these experiments to neutrino sources with known activity levels and appropriate energy, under conditions nearly identical to those used in solar exposures [79].

These tests were done by the two groups in their respective detectors, and the corresponding experimental characteristics are described in the following sections, together with the analysis of the final results.

3.1.1 GALLEX

The GALLium EXperiment detector was located at the Gran Sasso underground laboratory, in Italy, reducing the muon induced background by shielding the facility by about 3300 meters of water equivalent. The *radiochemical source experiment* was used to test the detector using two radioactive sources with small differences, as explained later.

For the test, it was necessary to fabricate an intense and portable neutrino source with the following specifications [79]:

- the source activity level must be such that the measurements reach the precision of the measurements of the solar neutrino flux after 4 years of data collection;
- the energy of the emitted neutrinos must be close to the mean energy of solar neutrinos detected by GALLEX;
- the source lifetime must be long enough to allow transport of the source to the underground detector and the posterior development of the experiment.

After all this considerations, the ^{51}Cr nuclide was selected as the most suitable one. The radioactive nucleus ^{51}Cr is produced by neutron capture on ^{50}Cr, and has a lifetime of 27.7 days. It decays through electron capture to the ground state of ^{51}V (see figure 3.1),

$$e^- + {}^{51}_{24}\mathrm{Cr} \rightarrow {}^{51}_{23}\mathrm{V} + \nu_e, \tag{3.3}$$

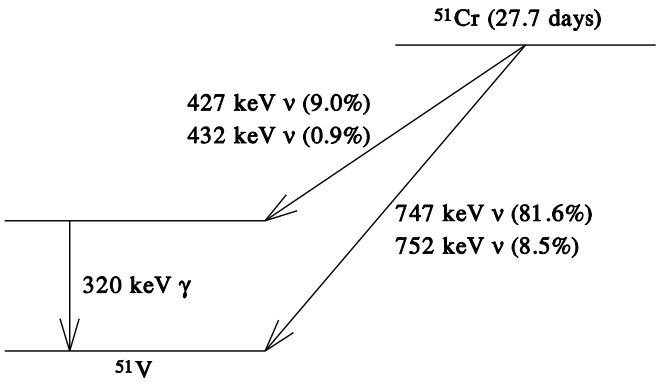

Figure 3.1: Decay scheme of the ^{51}Cr radioactive source [82].

GALLEX	**^{51}Cr**			
$\mathbf{E_\nu}$ **[keV]**	747	752	427	432
B.R. [%]	81.63	8.49	8.95	0.93
σ **[10^{-46} cm^2]**	60.8	61.5	26.7	27.1

Table 3.1: Energies (E_ν), branching ratios (B.R.) and Gallium cross sections (σ) of the ν_e lines emitted in ^{51}Cr decay through electron capture. The cross sections are interpolated from Table II of [85].

emitting ν_e lines with the energies and branching ratios listed in table 3.1, and a 320 keV γ.

The activity of the ^{51}Cr source must be larger than 50 PBq[1] in order to produce a signal about one order of magnitude grater than that of the Sun [79, 86]. To obtain the ^{51}Cr source, the ^{50}Cr isotope was transformed in ^{51}Cr by neutron capture in a nuclear reactor: $^{50}\mathrm{Cr}(n,\gamma)\,^{51}\mathrm{Cr}$ [87].

The activity of the final chromium source used as the neutrino sources in each of the two experiments, was measured using calorimetry, an ionization chamber, high-resolution gamma ray spectroscopy and neutron activation to measure the ^{51}V production (more details can be found in references [79, 80]). The resulting mean activity of each ^{51}Cr source at EOB[2] were [80]:

$$\begin{aligned} A_{\mathrm{Cr1}} &= 63.4 \pm 0.5 \text{ PBq}, \quad \text{for the first source;} \\ A_{\mathrm{Cr2}} &= 69.1 \pm 0.6 \text{ PBq}, \quad \text{for the second source.} \end{aligned} \tag{3.4}$$

These sources were placed inside tanks which contained the GALLEX detector (see

[1] 1 PBq = 10^{15} Bq, with Bq the unity to measure the number of nuclear transformations per second: 1 Bq = 1 nuclear transformations / s, which can be read as $1\mathrm{Bq} = 1\,\nu/s$.

[2] EOB is for end-of-bombardment.

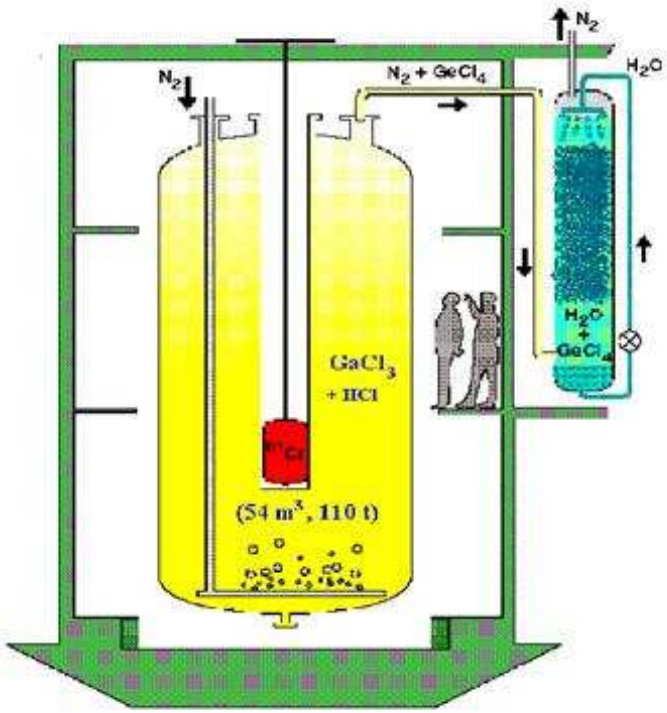

Figure 3.2: Scheme of the GALLEX tank containing the gallium chloride solution with the Cr source in the central tube.

GALLEX	**Cr1**	**Cr2**
Radius (m)	1.9	
Height (m)	5.0	
Source height (m)	2.7	2.38

Table 3.2: Radii and heights of the GALLEX cylindrical detectors and the heights from the base of the detectors at which the radioactive sources were placed along the axes of the detectors.

figure 3.2), composed of a $GaCl_3$-HCl solution, with $\sim$ 30tons of Gallium. All the experimental conditions were kept as close as possible to those for the solar experiments. The position of the radioactive sources and the size of the detectors are shown in table 3.2, where it should be noticed that for the second source experiment, the ^{51}Cr source was located at a position 32 cm lower than the position of the first source.

As mentioned above, the ^{51}Cr source decays through electron capture, equation (3.3), and the electron neutrinos generated in this process interact with the Gallium in

GALLEX	**Cr1**	**Cr2**
$\mathbf{Q_{Ge}^{exp}}$ **(^{71}Ge/d)**	11.9 ± 1.3	10.7 ± 1.4
R	1.00 ± 0.10	0.81 ± 0.10

Table 3.3: Measured production rates $Q_{\rm Ge}^{\rm exp}$ and Ratios R for the two GALLEX ^{51}Cr radioactive source experiments.

the detector through the same process used for detecting solar neutrinos, equation (3.2). The neutrino flux can be measured precisely, by counting the amount Germanium produced in the process. The ^{71}Ge atoms combine with the Cl forming the volatile molecule $GeCl_4$, which is extracted from the tank by air circulation. Then, the Ge is transformed into germane GeH_4 which is used as the gas of a proportional counter, used to observe the ^{71}Ge decay ($\tau_{1/2} = 11.43$ d) [87].

Then, the experimental production rate of ^{71}Ge, $Q_{\rm Ge}^{\rm exp}$, is compared with the expected one in absence of neutrino oscillations, $Q_{\rm Ge}$, using the ratio

$$R^{\rm exp} = \frac{Q_{\rm Ge}^{\rm exp}}{Q_{\rm Ge}}. \tag{3.5}$$

In table 3.3 the measured production rate of ^{71}Ge and the corresponding ratio for the two runs are presented. The numbers are collected from reference [73], which has different R values to the reported by the GALLEX collaboration [79, 80], as the result of a later revision on the results (see reference [3] of [73]).

In absence of neutrino oscillation, it is expected to have $R = 1$, but the GALLEX Cr2 result in table 3.3 shows an almost 2σ deviation from one. Assuming that the Germanium counting process and results as well as the theoretical value of the cross section of the process (3.2) are correct, this anomalous result could be interpreted as a hint of the presence of electron neutrino disappearance, produced by neutrino oscillations, motivating the present analysis.

Here we do the analysis of these two individual experimental results to determine the neutrino oscillation parameters, $(\sin^2(2\theta), \Delta m^2)$, adopting a Bayesian approach, as done in reference [88]. To do this calculation, the theoretical value of the ratio R of the predicted ^{71}Ge production rates in the presence and absence of neutrino oscillations is defined as

$$R = \frac{\int dV L^{-2} \sum_i (B.R.)_i \, \sigma_i P_{\nu_e \to \nu_e}(L, E_{\nu,i})}{\sum_i (B.R.)_i \, \sigma_i \int dV L^{-2}}, \tag{3.6}$$

where i is the index of the ν_e energy lines emitted in the ^{51}Cr decay, as listed in table 3.1, $(\text{B.R.})_i$ and σ_i are the branching ratio and the cross section at the corresponding energy (see table 3.1), and $P_{\nu_e \to \nu_e}(L, E_{\nu,i})$ is the survival probability of electron neutrinos (in the effective framework of two neutrino oscillations) with energy E_ν at a distance L from the source, given by (equation (2.49))

$$P_{\nu_e \to \nu_e}(L, E_\nu) = 1 - \sin^2(2\theta) \sin^2\left(\frac{\Delta m^2 L}{4E_\nu}\right), \tag{3.7}$$

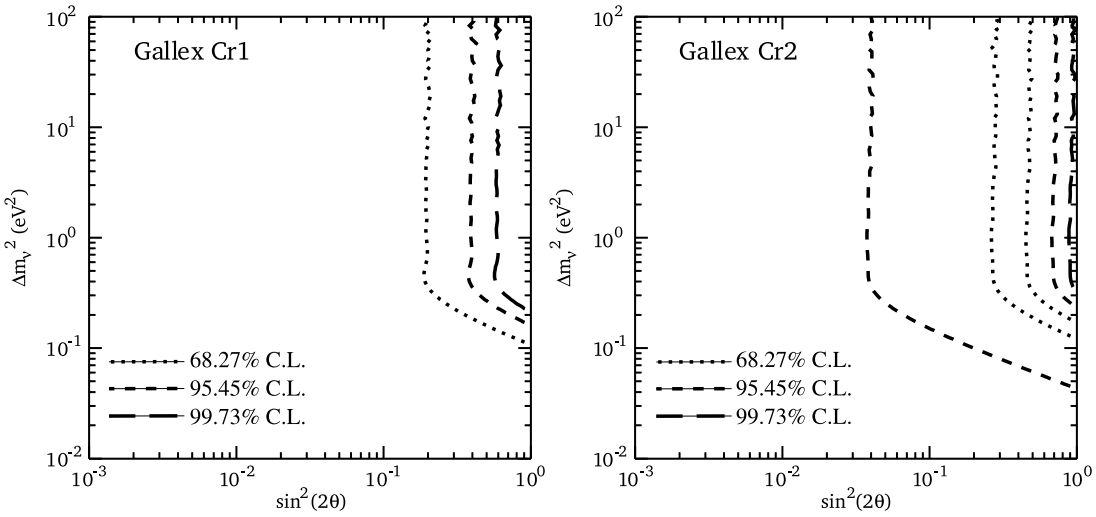

Figure 3.3: Allowed regions in the oscillation parameter space obtained from the fits of the results of the two GALLEX ^{51}Cr radioactive source experiments, Cr1 and Cr2. The curves in the GALLEX Cr1 plot exclude the regions on the right. In the GALLEX Cr2 plot, the pairs of 1σ and 2σ curves delimit allowed regions and the 3σ curve excludes the region on the right.

with θ the mixing angle and Δm^2 the square-mass difference.

In equation (3.6), the integration over L accounts for the distance travelled by the neutrino from the production point at the source, to the detection point (capture in the detector). The integration is, then, performed approximating the GALLEX detector and source as having a cylindrical shape with the dimensions shown in table 3.2. We averaged the neutrino path length L with a Monte Carlo integration over the volume V of each cylindrical detector, taking into account the different positioning of the source.

In the Bayesian approach, R in equation (3.6) is considered as a random variable with a uniform (flat) prior probability distribution between zero and one. If $R_{\rm obs}$ is the observed value of R, the normalized posterior probability distribution of R is given by

$$p(R|R_{\rm obs}) = \frac{p(R_{\rm obs}|R)}{\int_0^1 dR\, p(R_{\rm obs}|R)}. \tag{3.8}$$

Here, $p(R_{\rm obs}|R)$ is the sampling distribution of $R_{\rm obs}$ given R, which we assume to be a Gaussian with standard deviation equal to the experimental uncertainty,

$$p(R_{\rm obs}|R) = \frac{1}{\sqrt{2\pi}\,\sigma_{\rm exp}} \exp\left(-\frac{R - R_{\rm obs}}{\sqrt{2}\,\sigma_{\rm exp}}\right)^2. \tag{3.9}$$

The allowed interval of R with a given Bayesian Confidence Level is given bay the Highest Posterior Density interval with integrated probability equal to the Confidence

Level (C.L.),

$$1-\alpha=\int_{R_{\rm low}}^{R_{\rm up}} dR\, p(R|R_{\rm obs})=\frac{1}{N}\int_{R_{\rm low}}^{R_{\rm up}} dR\,\left[\exp\left(-\frac{R-R_{\rm obs}}{\sqrt{2}\,\sigma_{\rm exp}}\right)^2\right], \qquad (3.10)$$

where $R_{\rm low,\ up}$, are the limits such that $p(R|R_{\rm obs})$ is higher everywhere inside the interval $[R_{\rm low}, R_{\rm up}]$, than outside [63], and N is the value of the integral in the denominator of (3.8).

The resulting allowed regions are shown in Figure 3.3. One can note that the result for the first GALLEX source experiment (Cr1), for which the measured rate is within 1σ from unity, shows only upper limits for the mixing parameters. On the other hand, the second GALLEX experiment (Cr2), gives 2σ allowed bands, that shows a value of the square-mas difference of $\Delta m^2 > 1\text{eV}^2$, which is much larger than the known measurements from Solar and Atmospheric neutrino oscillation experiments.

3.1.2 SAGE

The other radioactive source experiment was developed to test the SAGE (Soviet-American Gallium Experiment) detector, which was used to measure the capture rate of solar neutrinos with a target of gallium metal in liquid state. The SAGE detector was located in the Baksan Neutrino Observatory, in Russia [82].

The test of the SAGE detector was performed using two different radioactive artificial neutrino sources: the first one using ^{51}Cr and the second one using ^{37}Ar.

In the case of the ^{51}Cr source experiment, similar considerations to the ones taken by the GALLEX collaboration were taken into account here. The chromium used in this experiment was enriched to 94.4% in ^{50}Cr, which has the advantage of yielding a great specific activity and a small physical size, thus giving a high neutrino capture rate [82].

The 55 tons of Ga that SAGE used for solar neutrino measurements were contained in eight chemical reactors with approximately 7 tons in each. Figure 3.4 shows the layout of the ten reactors in the experimental area. In normal solar neutrino operation, Ga is contained in reactors $2-5$ and $7-10$. All reactors except number 6 are equipped with the necessary mechanical equipment for the extraction process. Reactor 6 was modified for the Cr exposures by removing its stirring mechanism and replacing it with a reentrant Zr tube on its axis which extended to the reactor center. This modification increased the capacity of the reactor to 13 tons of Ga. To begin each irradiation, a remote handling system (figure 3.5) was used to place the ^{51}Cr source inside this reentrant tube at the reactor center. At the end of each irradiation, the source was moved to an adjacent calorimeter for activity measurement, and the gallium was pumped back to the two reactors where it was stored during solar neutrino runs [82]. For the Cr experiment, reactors $6-10$ in figure 3.4 were used.

As for the GALLEX experiment, the source activity was determined by measuring its heat (energy deposited in its surroundings) with a calorimeter, and by the measurement of the 320-keV gamma rays emitted by the ^{51}Cr. The average activity of the

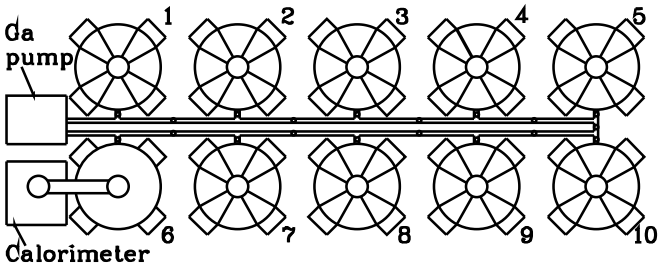

Figure 3.4: View of the SAGE laboratory showing the ten chemical reactors, irradiation reactor 6 with the adjacent calorimeter and the Ga pump for transferring the Ga between reactors [82].

SAGE	^{51}**Cr** ^{37}**Ar**
Radius (m)	0.7
Height (m)	1.47
Source height (m)	0.72

Table 3.4: Radii and heights of the SAGE cylindrical detectors and the heights from the base of the detectors at which the radioactive sources were placed along the axes of the detectors.

source was [82]

$$A_{^{51}\mathrm{Cr}} = 19.114 \text{ PBq}. \tag{3.11}$$

The ^{51}Cr source source was located in a central position inside the detector, as depicted in figure 3.5, which we approximated as cylindrical. Table 3.4 shows the dimensions of the detector and the height from the base of the detector at which the source was placed.

The source then, decays as depicted in equation (3.3), producing electron neutrinos with the energies and branching rations shown in table 3.1. The produced electron neutrinos interact with the Gallium in the detector via the process (3.2). The extracted Ge was synthesized into the counting gas GeH_4, mixed with Xe, and inserted into a very low-background proportional counter [82].

For the second experiment to test the SAGE detector, the SAGE collaboration used an ^{37}Ar source. Among the avantages of using ^{37}Ar instead of ^{51}Cr as the source, there are the following [73]:

- the desired active isotope must be chemically separated from the target following irradiation's, allowing the remotion of almost all the impurities that are present in the target, so that the ^{37}Ar source results to be practically free of radioactive impurities;
- ^{37}Ar has a longer half-life, giving longer time to prepare the source end to make measurements;

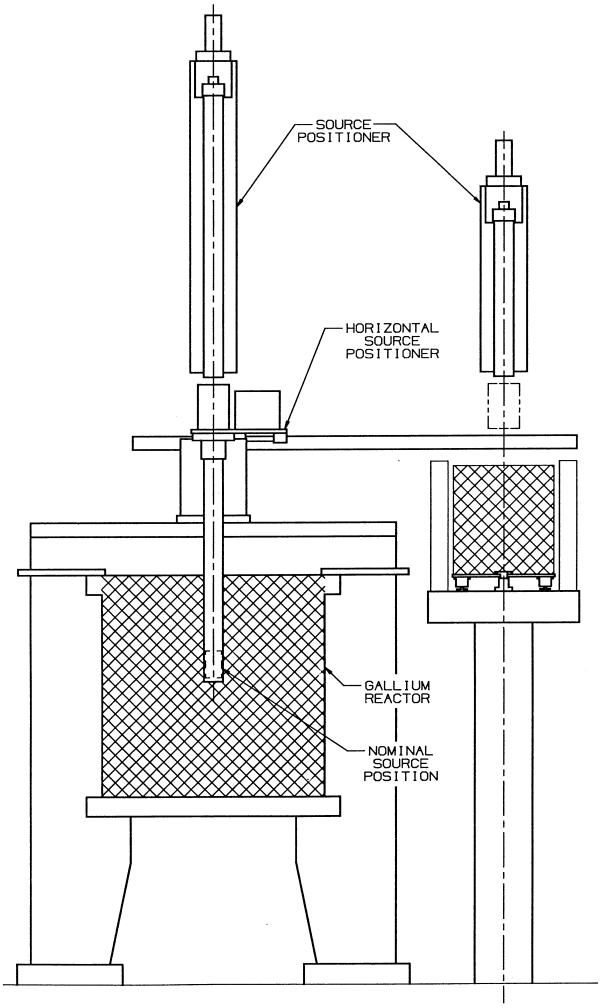

Figure 3.5: Scheme of the remote handling system which moved the ^{51}Cr source from the gallium-containing reactor to the adjacent calorimeter [82].

- the energy of the produced neutrinos is greater than in the case of ^{51}Cr, giving a higher cross section;
- there is no emission of γ rays, so the required shielding is less than for ^{51}Cr and the source can be very compact.

^{37}Ar decays ($\tau_{1/2} = 35.04 \pm 0.04$ d) to ^{37}Cl by the electron capture process

$$e^- + {}^{37}_{18}\mathrm{Ar} \longrightarrow {}^{37}_{17}\mathrm{Cl} + \nu_e. \tag{3.12}$$

In figure 3.6 and table 3.5, the decay process and the neutrino energy lines, with the corresponding branching ratios are shown.

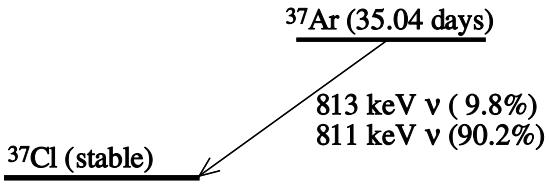

Figure 3.6: Scheme of the ^{37}Ar decay, showing the neutrino energies [73].

SAGE	^{37}**Ar**	
$\mathbf{E_\nu}$ **[keV]**	811	813
B.R. [%]	90.2	9.8
σ **[10^{-46} cm^2]**	70.1	70.3

Table 3.5: Energies (E_ν), branching ratios (B.R.) and Gallium cross sections (σ) of the ν_e lines emitted in ^{37}Ar decay through electron capture. The cross sections are interpolated from Table II of [85].

The method used to produce the ^{37}Ar source was irradiation of calcium oxide, following the neutron capture reaction $^{40}\mathrm{Ca}(n,\alpha)\,^{37}\mathrm{Ar}$, performed in the reactor BN-600 at Zarechny, Russia [73].

The experimental procedure and equipment were basically the same as those used by the SAGE Cr source experiment, described previously, using the same experimental area depicted in figure 3.4, and the same remote handling system shown in figure 3.5. In addition, the activity of the ^{37}Ar source was measured using similar techniques to those used for the chromium source, obtaining an average activity of

$$A_{^{37}\mathrm{Ar}} = 15.13 \text{ PBq}. \tag{3.13}$$

For the experiment, the source was located in the center of the cylindrical detector, considering the dimensions and position which are written in table 3.4. The electron neutrinos produced in the argon decay interact with the Gallium in the detector producing Ge as in equation (3.2), and the resulting Ge was synthesized into the counting gas GeH_4, mixed with inactive Xe and inserted into a proportional counter with a carbon-film cathode.

As in the GALLEX experiment, the measured and predicted (in absence of oscillation) production rates are compared using (3.5). The results for the two SAGE experiments are presented in table 3.6.

Also here there is an anomalous value of the ratio R coming from the SAGE ^{37}Ar experiment. In this case, the result has a deviation larger than 2σ, so the possible hint of electron neutrino disappearance is also motivated in this case.

The analysis of these experimental result is performed in the same way that for the GALLEX results, considering the geometrical configuration shown in figure 3.5, taking the detector with cylindrical shape with the dimensions shown in table 3.4.

SAGE	**^{51}Cr**	**^{37}Ar**
$\mathbf{Q_{Ge}^{exp}}$ **(^{71}Ge/d)**	14.0 ± 1.7	11.0 ± 1.5
R	0.95 ± 0.12	0.79 ± 0.10

Table 3.6: Measured production rates $Q_{\mathrm{Ge}}^{\mathrm{exp}}$ and ratios R for the SAGE ^{51}Cr and ^{37}Ar radioactive source experiments.

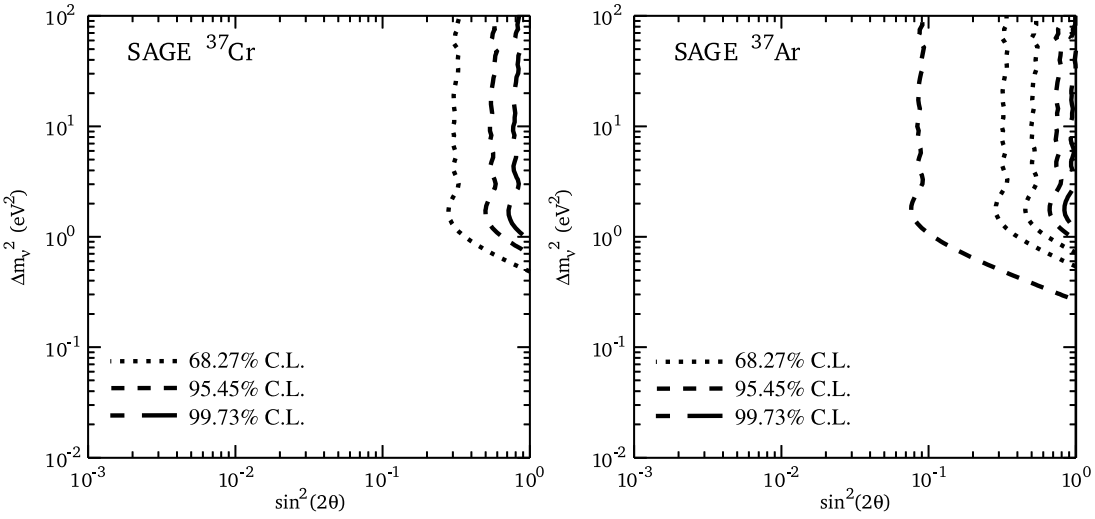

Figure 3.7: Allowed regions in the oscillation parameter space obtained from the fits of the results of the SAGE ^{51}Cr and ^{37}Ar radioactive source experiments. The curves in the SAGE ^{51}Cr plot exclude the region on the right. In the SAGE ^{37}Ar plot, the pairs of 1σ and 2σ curves delimit allowed regions and the 3σ curve excludes the region on the right.

Following the highest posterior density procedure as described previously, and using the theoretical ratio as equation (3.6) with the information of tables 3.1 and 3.5 (for ^{51}Cr and ^{37}Ar, respectively), the SAGE ^{51}Cr experimental datum results in the upper limits for the oscillation parameters shown in the left panel of figure 3.7, while in the right panel of the same figure an allowed band at 2σ is shown from the analysis of the SAGE ^{37}Ar datum.

The value of the ratio of measured and expected events (without oscillations) from SAGE ^{37}Ar, which presents a deviation from unity larger than 2σ, results in an allowed region for a Δm^2 larger or equal to 1 eV^2, and by comparison with the allowed region resulting from the GALLEX Cr2 (right panel of figure 3.3), one can see that there is a large overlap for the 2σ bands, for $\Delta m^2 \gtrsim 1$ eV.

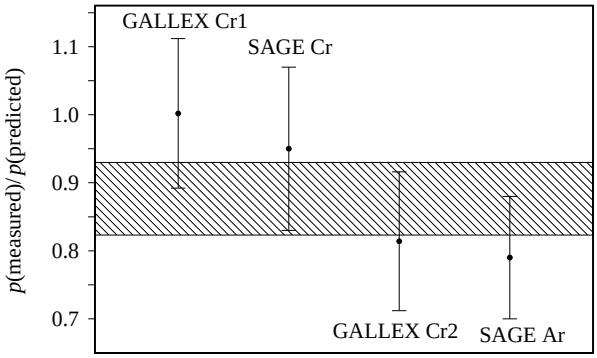

Figure 3.8: Experimental results of the four neutrino source experiments with Gallium. The hashed region corresponds to the weighted average, equation (3.14) [73].

3.1.3 Combined analysis

For the Combined analysis of the Gallium radioactive source experiments, we consider the results of each experiment, tables 3.3 and 3.6, presented graphically in figure 3.8. The weighted average value of the ratios, R, of the measured and predicted (in absence of oscillations) ^{71}Ge production rates of the four experiments Gallium radioactive source experiments (GALLEX Cr1 and Cr2, and SAGE Cr and Ar) is [73]

$$R_{\mathrm{Ga}} = 0.88 \pm 0.05, \tag{3.14}$$

with a deviation from unity of more than 2σ. Then, here there is also present the anomalous result which could be interpreted as an indication of the disappearance of electron neutrinos due to neutrino oscillations [74, 75, 76].

Since there are enough data points to determine the two mixing parameters $\sin^2 2\theta$ and Δm^2, we abandon the Bayesian approach in favor of a standard frequentist least-squares fit. This method is based on a global minimization of the χ^2 in the $\sin^2 2\theta$-Δm^2 plane and the calculation of the Confidence Level contours corresponding to a $\Delta\chi^2$ with two degrees of freedom: $\Delta\chi^2 = 2.30, 6.18, 11.83$ for 68.27% (1σ), 95.45% (2σ) and 99.73% (3σ) C.L., respectively (see [63]). We use a χ^2-function given by

$$\chi^2 = \sum_{i=1}^{4} \left(\frac{R_i^{\mathrm{the}} - R_i^{\mathrm{exp}}}{\sigma_i} \right)^2, \tag{3.15}$$

where R_i^{the} is computed using equation (3.6), and R_i^{exp} and σ_i are the four different experimental ratios and their errors, taken from tables 3.3 and 3.6.

Gallium experiments		
No Osc.	$\chi^2_{\rm min}$	8.21
	NDF	4
	GoF	0.084
Osc.	$\chi^2_{\rm min}$	2.94
	NDF	2
	GoF	0.23
	$\sin^2 2\theta_{\rm bf}$	0.23
	$\Delta m^2_{\rm bf}$ (eV^2)	2.09

Table 3.7: Results for fit of the different combinations of the Gallium radioactive source experiments. The first three lines correspond to the case of no oscillations (No Osc.). The following five lines correspond to the case of oscillations (Osc.).

Parameter	**C.L.**	**Gallium**
$\sin^2 2\theta$	68.27% (1σ)	$0.12 - 0.33$
	95.45% (2σ)	> 0.028
	99.73% (3σ)	–
Δm^2 [eV^2]	68.27% (1σ)	> 0.85
	95.45% (2σ)	> 0.079
	99.73% (3σ)	–

Table 3.8: Allowed ranges of $\sin^2 2\theta$ and Δm^2 from the combined fit of the results of Gallium radioactive source experiments. The dash indicates the absence of limits.

The result of the combined least-squares analysis of the four Gallium source experiments is shown in figure 3.9. One can see that there is an allowed region in the $\sin^2 2\theta$-Δm^2 plane at 1σ for $\Delta m^2 \gtrsim 0.6\,\text{eV}^2$ and $0.08 \lesssim \sin^2 2\theta \lesssim 0.4$. The values of $\chi^2_{\rm min}$, the number of degrees of freedom (NDF), the goodness-of-fit (GoF) and the best-fit values of the mixing parameters are given in table 3.7. The value of the the goodness-of-fit (23%) shows that the fit is acceptable.

Table 3.8 shows the allowed ranges of $\sin^2 2\theta$ and Δm^2 obtained from the corresponding marginal $\Delta\chi^2 \equiv \chi^2 - \chi^2_{\rm min}$ in figure 3.9. The presence of 2σ lower limits for $\sin^2 2\theta$ and Δm^2 in spite of the absence of a 2σ lower limit in the $\sin^2 2\theta$-Δm^2 plane in figure 3.9 is an effect due to the statistical analysis: for one parameter 2σ corresponds to $\Delta\chi^2 = 4$, whereas for two parameters it corresponds to $\Delta\chi^2 = 6.18$. Hence, it is fair to conclude that there is an indication of a possible neutrino disappearance due to neutrino oscillations with $\sin^2 2\theta \gtrsim 0.03$ and $\Delta m^2 \gtrsim 0.1\,\text{eV}^2$ at a confidence level between one and two sigmas ($\sim 70 - 90\%$ C.L.).

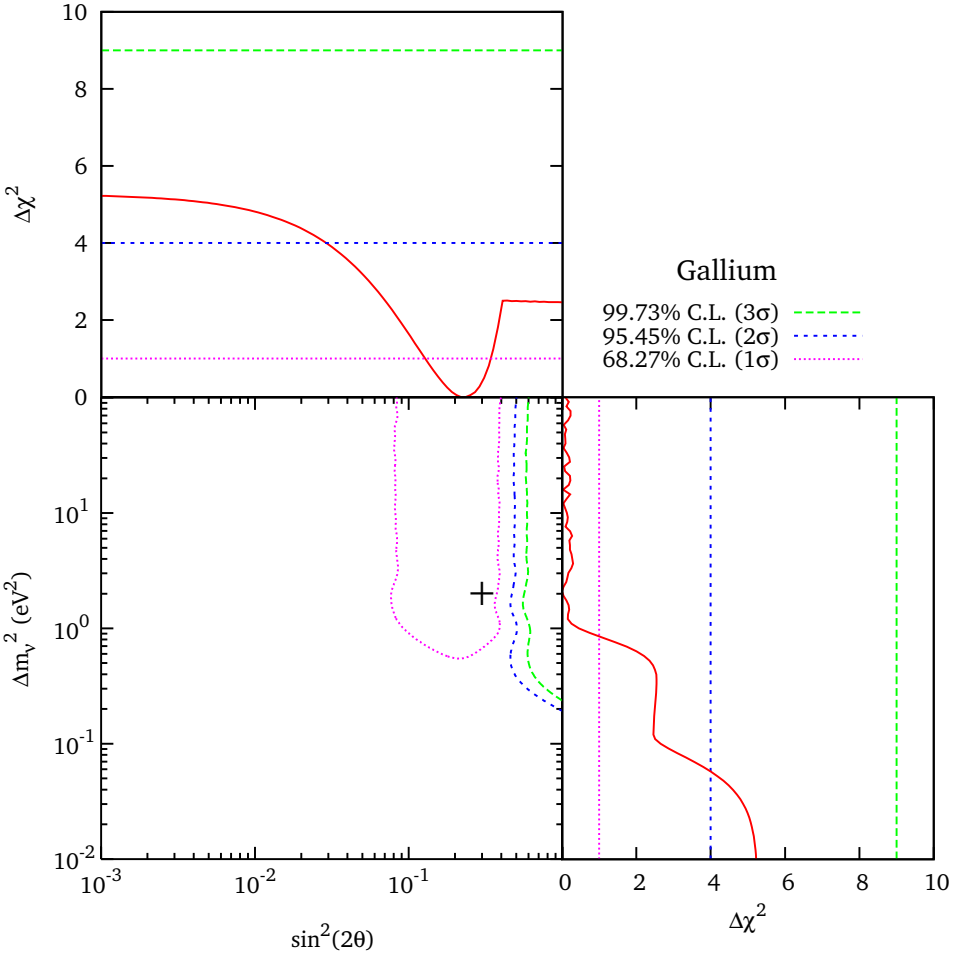

Figure 3.9: Allowed regions in the $\sin^2 2\theta$-Δm^2 plane and marginal $\Delta\chi^2$'s for $\sin^2 2\theta$ and Δm^2 obtained from the combined fit of the results of the two GALLEX ^{51}Cr radioactive source experiments and the SAGE ^{51}Cr and ^{37}Ar radioactive source experiments. The best-fit point corresponding to $\chi^2_{\rm min}$ is indicated by a cross.

3.2 Nuclear Reactor experiments

Nuclear reactors use neutrons to break heavy nuclei. Each fission produces more neutrons, raising up a chain reaction which generates nuclear fragments that decay producing a high flux of $\overline{\nu}_e$ and kinetic energy [18]. Most of the energy in nuclear reactors is generated from the fission of the isotopes ^{235}U, ^{239}Pu, ^{238}U and ^{241}Pu. In nuclear reactors used for neutrino experiments, the typical power is a few GW ($1\text{GW} = 6.24 \times 10^{21}$ MeV s^{-1}), and neutrinos have a typical energy $E_\nu \sim$ MeV. Although current nuclear power plants are made with several reactor cores, such that

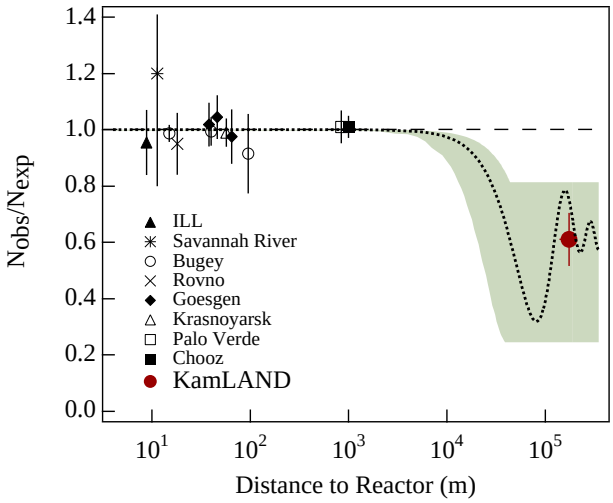

Figure 3.10: The ratio of the measured to the expected $\overline{\nu}_e$ flux from different reactor experiments as a function of their source-detector distance. The shaded region indicates the range of flux predictions corresponding to the 95% C.L. LMA region found on a global analysis of the solar neutrino data. The dotted curve corresponds to the best fit values $\Delta m^2_{\rm sol} = 5.5 \times 10^{-5}$ eV^2 and $\sin^2 2\theta_{\rm sol} = 0.83$ [48].

they produce a very high antineutrino flux, this flux decreases very fast with distance, because it is isotropic. This point has problematic effects for neutrino oscillations research because, to reveal neutrino oscillations, it is necessary to have an appropriate source-detector distance [15]. On the other hand, due to the low energy, electrons are the only charged leptons that can be produced in the neutrino CC interaction. If the $\overline{\nu}_e$ oscillate to another flavor, its CC interaction could not be observed [20]. In this way, neutrino oscillations can be studied with nuclear reactors by looking for variations in the observed neutrino flux and spectrum with distance. This is the so-called *disappearance method* (see section 2.3.2), which has the advantage that small values of Δm^2 can be studied.

In reactor neutrino experiments, the electron antineutrinos are detected through the inverse neutron decay process

$$\overline{\nu}_e + p \longrightarrow n + e^+, \tag{3.16}$$

which liberates a total visible energy $E_e + m_e$, where E_e is the energy of the positron, which annihilates immediately with surrounding electron. This energy can be observed using a scintillator by distinguishing the antineutrino events from the background, by the coincidence of the prompt positron signal and the delayed signal produced by the nuclear capture of the neutron. The antineutrino energy is related to the positron kinetic energy E_{e^+} by

$$E_\nu = E_{e^+} + m_e + T_n + m_n - m_p \simeq E_{e^+} + 1.8\text{MeV}, \tag{3.17}$$

where T_n is the negligibly small recoil energy of the neutron.

Reactor neutrino experiments can be classified according to their source-detector distance L as:

- Short-baseline (SBL) reactor experiments, with source-detector distance between 10 and 100 m. Given this short distance, it is not possible to reach enough sensitivity to small values of Δm^2 as to observe $\overline{\nu}_e$ disappearance due to the solar Δm^2.

- Long-baseline (LBL) reactor experiments, with a source-detector distance of the order of 1 km, allowing a sensitivity on Δm^2 of about 10^{-3} eV^2, such that the region of Δm^2 corresponding to atmospheric neutrino oscillations is covered.

Figure 3.10 shows the ratio of measured to expected electron antineutrino flux of different reactor neutrino experiments as a function of their source-detector distance L, some of which are described in the following sections, and the analysis of their results is presented.

3.2.1 Bugey

The Bugey nuclear power plant ran with four Pressurized Water Reactors (PWR) of 2800 thermal MW each. In a first experiment performed using two detectors at 14 and 18 m from one of the reactors [89], and using a position-1/position-2 ratio analysis, they found a deficiency in the expected neutrino flux, which was interpreted as an indication of neutrino disappearance (at 3σ level) [89]. Later, introducing a different neutron detection technique, the Bugey collaboration made another measurement, searching for electron antineutrino disappearance, using three identical module detectors placed at distances $L_j = 15, 40, 95$ m [90, 91]: one of the modules was located under the reactor building, at 15 m from the core, ant the other two were placed outside the reactor building, inside a concrete bunker, at 40 m away from the core (see more details bellow).

The Bugey experiment detected $\overline{\nu}_e$ by their charged current interaction, equation (3.16), on the free protons of the target which is a pseudocumene $C_6H_3(CH_3)_3$ based liquid scintillator with a H/C ratio of 1.4 doped with 0.15% in mass of ^{6}Li. The signature of such an event is [90]:

- a prompt light pulse from the positron which can be related through the response function of the detector to the positron energy E_e, and the the neutrino energy is given by equation (3.17);

- a delayed (by 30 μs on average) light pulse due to the produced neutron which is thermalized and captured with high probability by the ^{6}Li nuclei in the liquid, via the reaction

$$n + {}^6\mathrm{Li} \rightarrow {}^4\mathrm{He} + {}^3\mathrm{H} + 4.8 \text{ MeV}. \tag{3.18}$$

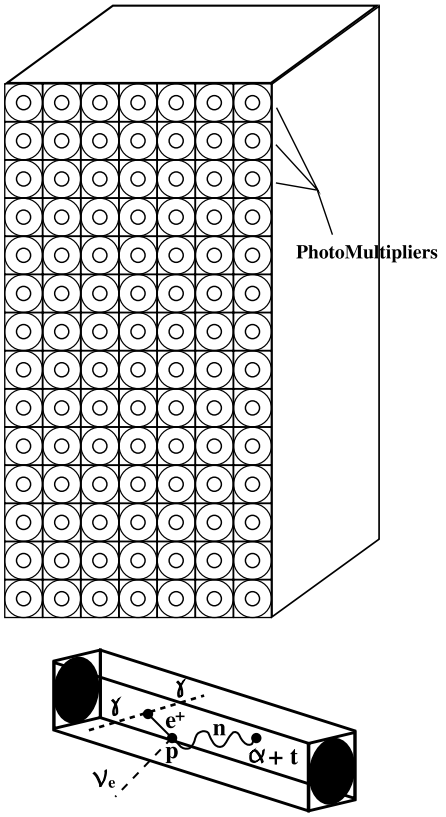

Figure 3.11: Schematic view of one detector module [90].

The neutron capture time and its mean free path allow efficient reduction of the accidental background by performing delayed time coincidence between the neutron and the positron signals, as well as by requiring spatial proximity between, them making use of the segmentation of the detector. The main components of the accidental background are Compton electron produced by low energy photons and α-particles from internal radioactivity of the scintillator [90].

A schematic view of one detector module is shown in figure 3.11. It is a $\sim$ 600 liter tank of $85 \times 122.5 \times 61.8$ cm^3 internal dimensions[3] and two acrylic windows on two opposite faces to collect the scintillation light. The tank is optically segmented in 98 cells, each with two 3−inch photomultiplayers. Three identical modules were constructed for the experiment, one installed at the 15 m station (Position 1), and the other two (one on top of the other) located in the 40 m station (Position 2).

Considering the origin of a reference frame in the center of the Reactor 5 of the Bugey nuclear plant, the location of the two stations and the two reactors used in the experiment is depicted in figure 3.12, and the precise coordinates are written in table

[3]The active part of the detector is $85 \times 120.4 \times 60.2$ cm^3 [91]

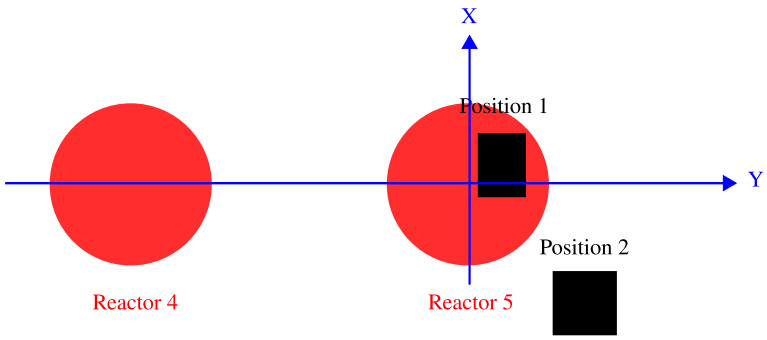

Figure 3.12: Localization of the Bugey nuclear reactors and detectors (top view) used for the neutrino oscillations experiment.

	Position 1			Position 2	
	Detector	**Reactor 5**	**Reactor 4**	**Detector**	**Reactor 5**
x(m)	3.53089	0.0	0.0	-36.818	0.0
y(m)	5.22890	0.0	-88.8	14.818	0.0
z(m)	-7.929	5.572	5.572	1.618	5.572

Table 3.9: Precise geometrical localization of the centers of detector and reactor cores at Position 1 and 2 of the Bugey Nuclear reactor plant [91].

3.9.

The module at the Position 1 was installed inside a shielding made of successive layers consisting of lead to stop photons, water and B_4C to slow down and capture fast neutrons, and liquid scintillator to tag cosmic ray particles passing through the shielding. The shielding of the modules at Position 2 used iron instead of lead in the first layer.

The experimental data were collected at three different source-detector distances, as follow (see figure 3.12) [90, 91]:

- $L_1 = 15$ m data set: electron antineutrinos from Reactor 5 were detected with the module located at Position 1, inside the reactor building;
- $L_2 = 40$ m data set: electron antineutrinos from Reactor 5 were detected with the two modules located at Position 2, outside the reactor building;
- $L_3 = 95$ m data set: taken during the shutdown of Reactor 5, electron antineutrinos from Reactor 4 were detected with the module located at Position 1, inside the building of Reactor 5.

Figure 3.13 (taken from [90]) shows the ratio of the measured positron spectra to the ones predicted in the absence of oscillations at the three source-detector distances.

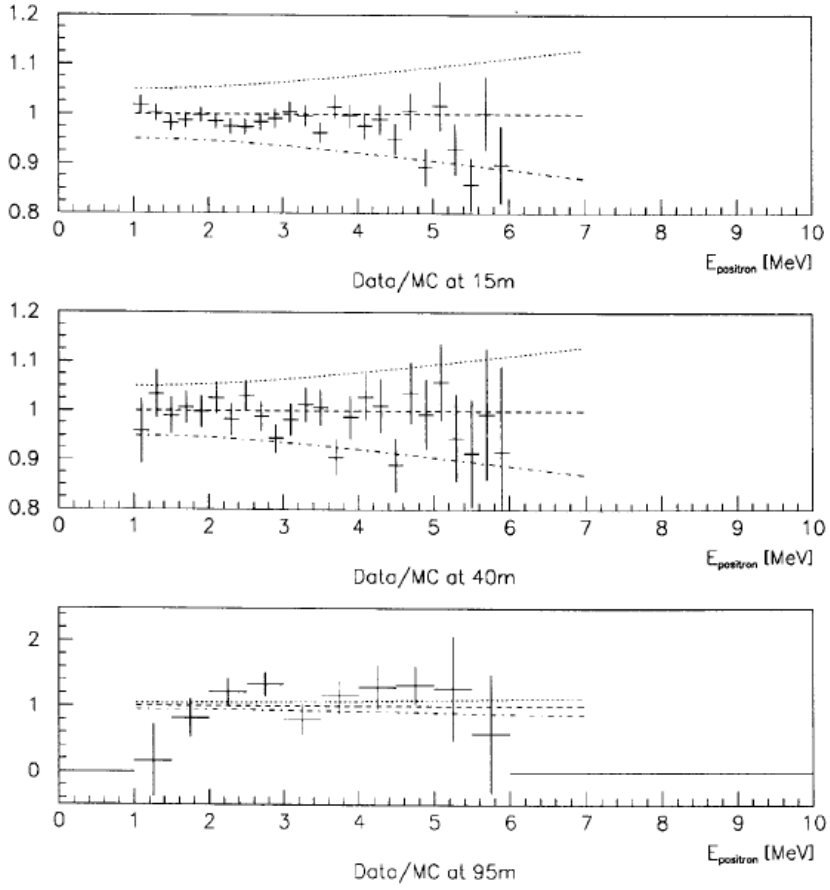

Figure 3.13: The ratio of the observed and the predicted positron spectra in absence of oscillations. Upper panel for $L_1 = 15$ m; middle panel for $L_1 = 40$ m; lower panel for $L_1 = 95$ m [90].

For the analysis we consider the data from the three source-detector distances, $L_j = 15, 40, 95$ m for $j = 1, 2, 3$, respectively, shown in figure 3.13. As can be seen in the figure, there are $N_j = 25, 25, 10$ energy bins. We analyze these data with the following χ^2 function, taken from reference [90]:

$$\chi^2 = \sum_{j=1}^{3} \left\{ \sum_{i=1}^{N_j} \frac{\left[(Aa_j + b(E_{ji} - E_0)) R_{ji}^{\text{the}} - R_{ji}^{\text{exp}} \right]^2}{\sigma_{ji}^2} + \frac{(A_j - 1)^2}{\sigma_{a_j}^2} \right\} + \frac{(A-1)^2}{\sigma_A^2} + \frac{b^2}{\sigma_b^2}, \tag{3.19}$$

where E_{ji} is the central energy of the ith bin in the positron kinetic energy spectrum measured at the L_j source-detector distance, R_{ji}^{exp} and R_{ji}^{the} are, respectively, the corresponding measured and calculated ratios. The uncertainties σ_{ji} include the

statistical uncertainty of each bin and a 1% systematic uncertainty added in quadrature, which takes into account the uncertainty of the spectrum calculation (with a total of about 5% uncorrelated systematic uncertainty over 25 bins). The coefficients $(Aa_j + b\,(E_{ji} - E_0))$, with $E_0 = 1\,\mathrm{MeV}$, were introduced in reference [90] in order to take into account the systematic uncertainty of the positron energy calibration. The value of χ^2 as a function of $\sin^2 2\theta$ and Δm^2 is calculated by minimizing equation (3.19) with respect to the five parameters A, a_j $(j = 1, 2, 3)$, b, which have, respectively, uncertainties $\sigma_A = 0.048$, $\sigma_{a_j} = 0.014$ $\sigma_b = 0.02\,\mathrm{MeV}^{-1}$ [90]. Following reference [92], we approximate the neutrino flux, the detection cross section and the detection efficiency as constants in each energy bin. The theoretical ratio R_{ji}^{the} is given by

$$R_{ji}^{\mathrm{the}} = \frac{\int \mathrm{d}L\, L^{-2} \int_{E_{ji}-\Delta E_j/2}^{E_{ji}+\Delta E_j/2} \mathrm{d}E \int_{-\infty}^{+\infty} \mathrm{d}T_e\, F(E, T_e)\, P_{\bar{\nu}_e \to \bar{\nu}_e}(L, E_\nu)}{\Delta E_j \int \mathrm{d}L\, L^{-2}}\,. \tag{3.20}$$

Here T_e and E_ν are, respectively, the positron kinetic energy and the neutrino energy, related by equation (3.17), whereas E is the measured positron kinetic energy, which is connected to T_e by the energy resolution function of the detector $F(E, T_e)$. We considered a Gaussian energy resolution function,

$$F(E, T_e) = \exp\left[-\left(\frac{T_e - E}{\sqrt{2}\,\sigma}\right)^2\right], \tag{3.21}$$

with standard deviation $0.252\sqrt{E\,/4.2\,\mathrm{MeV}}$ MeV [90]. The quantities ΔE_j are the widths of the energy bins in each detector. The integration over the neutrino path length L is performed by a Monte Carlo which takes into account the geometries of the reactor and of the detectors and their relative positions [91], information collected in table 3.9.

Figure 3.14 shows the allowed regions in the $\sin^2 2\theta - \Delta m^2$ plane and the marginal $\Delta\chi^2$ for $\sin^2 2\theta$ and Δm^2 obtained from the least-squares analysis of the Bugey data. The value and location in the $\sin^2 2\theta$–Δm^2 plane of the minimum of the χ^2, the number of degrees of freedom (NDF) and the goodness-of-fit (GoF) are given in table 3.10. The fit is satisfactory, since the goodness-of-fit is 69%. The best-fit value of the oscillation parameters and the small 1σ allowed regions in figure 3.14 are in favor of neutrino oscillations. However, the 2σ and 3σ contours in figure 3.14 provide only upper limits to neutrino oscillations. Also, the value of the χ^2 in the case of absence of oscillations and the corresponding goodness-of-fit (63%) do not allow us to exclude the absence of oscillations.

The reason of the hint in favor of neutrino oscillations given by the Bugey data is illustrated in figure 3.15, where the histogram relative to the best fit is shown against the Bugey R_{ji}^{exp}'s. With the help of the histogram, one can see that there is a weak hint of oscillations. The 1σ allowed regions in figure 3.14 have very narrow Δm^2 ranges around $0.9\,\mathrm{eV}^2$, $1.96\,\mathrm{eV}^2$, and $3\,\mathrm{eV}^2$, because slight shifts of Δm^2 from these optimal values spoil the agreement with the data of the histogram in figure 3.15. In each panel of figure 3.15, the dash-dotted and dashed histograms correspond, respectively, to the

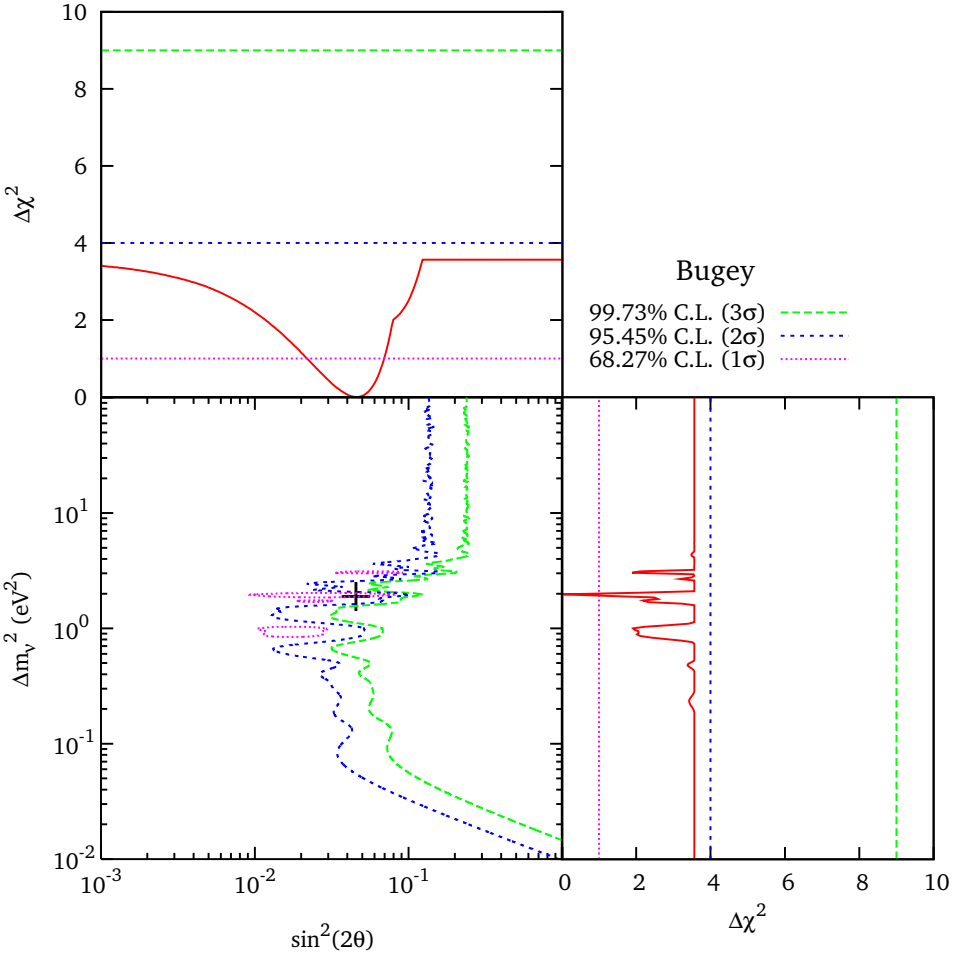

Figure 3.14: Allowed regions in the oscillation parameter space and marginal $\Delta\chi^2$s for $\sin^2 2\theta$ and Δm^2 obtained from the least-squares analysis of the Bugey data. The best fit point corresponding to χ^2_{min} is indicated by a cross.

best-fit values of $(Aa_j + b\,(E_{ji} - E_0))\,R^{\text{the}}_{ji}$ (with $A = 1.029$, $a_1 = 0.996$, $a_2 = 1.003$, $a_3 = 1.003$, $b = -0.009$) and R^{the}_{ji} (see equation (3.19))

Table 3.11 shows the marginal allowed ranges of $\sin^2 2\theta$ and Δm^2 obtained from the corresponding $\Delta\chi^2$'s in figure 3.14. One can see that there is a hint of neutrino oscillations with $0.02 \lesssim \sin^2 2\theta \lesssim 0.08$ and $\Delta m^2 \approx 1.9\,\text{eV}^2$.

From a comparison of figures 3.9 and 3.14 one can see that the allowed regions of the Gallium radioactive source experiments and the Bugey experiment are marginally compatible for $\sin^2 2\theta \sim 0.1$ and $\Delta m^2 \gtrsim 1\,\text{eV}^2$. Figure 3.16 shows the allowed regions obtained from the combined fit. Since the Bugey data are statistically dominant, the curves in Figure 3.16 are not very different from those in figure 3.14, which have been

Bugey		
No Osc.	$\chi^2_{\rm min}$	50.94
	NDF	55
	GoF	0.63
Osc.	$\chi^2_{\rm min}$	47.37
	NDF	53
	GoF	0.69
	$\sin^2 2\theta_{\rm bf}$	0.046
	$\Delta m^2_{\rm bf}$ (eV^2)	1.965

Table 3.10: Results for fit of the Bugey reactor experiment. The first three lines correspond to the case of no oscillations (No Osc.). The following five lines correspond to the case of oscillations (Osc.).

Parameter	C.L.	Bugey	Gallium + Bugey
$\sin^2 2\theta$	68.27% (1σ)	$0.022 - 0.070$	$0.033 - 0.079$
	95.45% (2σ)	–	$0.009 - 0.166$
	99.73% (3σ)	–	–
Δm^2 [eV^2]	68.27% (1σ)	$1.91 - 1.99$	$1.90 - 1.98$
	95.45% (2σ)	–	> 0.82
	99.73% (3σ)	–	–

Table 3.11: Allowed ranges of $\sin^2 2\theta$ and Δm^2 from the results of Bugey nuclear reactor experiment and from the combined fit of the Gallium radioactive source experiments and the Bugey reactor experiment. The dash indicates the absence of limits.

obtained from the fit of the Bugey data alone. The inclusion of the Gallium data has the effect of eliminating the 1σ allowed region at $\Delta m^2 \approx 0.9\,\text{eV}^2$ and of disfavoring at 1σ values of $\sin^2 2\theta$ smaller than about 2×10^{-2}. The value and location of $\chi^2_{\rm min}$, the number of degrees of freedom and the goodness-of-fit are listed in table 3.12. One can see that the Gallium data do not spoil the good fit of the Bugey data. Indeed, the value of the parameter goodness-of-fit[4] [93] reported in table 3.12 shows that the Bugey and Gallium data are compatible under the hypothesis of neutrino oscillations. The marginal allowed ranges of $\sin^2 2\theta$ and Δm^2 obtained from the corresponding $\Delta\chi^2$'s in figure 3.16 are given in table 3.11.

[4]The value of $(\Delta\chi^2_{\rm min})_{\rm A+B}$ corresponding to the parameter goodness-of-fit of two experiments A and B is given by $(\chi^2_{\rm min})_{\rm A+B} - [(\chi^2_{\rm min})_{\rm A} + (\chi^2_{\rm min})_{\rm B}]$. It has a χ^2 distribution with number of degrees of freedom NDF $= P_{\rm A} + P_{\rm B} - P_{\rm A+B}$, where $P_{\rm A}$, $P_{\rm B}$ and $P_{\rm A+B}$ are, respectively, the number of parameters in the fits of A, B and A+B data [93].

3.2.2 Chooz

The Chooz experiment [94, 95, 96] is a *Long-Baseline (LBL)* reactor experiments, with an average value of $L/E \sim 300$ km/MeV ($L \sim 1$ km, $E \sim 3$ Mev), designed to investigate $\overline{\nu}_e$ disappearance, by the detection of $\overline{\nu}_e$ via the inverse β-decay reaction, equation (3.16).

The Chooz nuclear power plant is located near the banks of the River Meuse in the north of France. It consists of two pressurized-water reactors with a total thermal power of $8.5\mathrm{GW_{th}}$ [96, 15]. The core of both reactors consists of an assembly of 205 fuel elements bound to the socket plate of the reactor vessel. The vessel is filled with pressurized water ($p = 155$ bars) at a temperature ranging from 280 °C at the entrance to about 320 °C at the exit. The water acts as a neutron moderator and cooling element.

The nuclear fuel consists of 110 T of uranium oxide tablets (diameter = 8.2mm) enriched with ^{235}U and stacked in 4 m long, 1 cm wide assemblies. Each fuel element contains 264 assemblies. About 1/3 of the 205 fuel elements are changed at the end of each cycle. The remainder is displaced towards the center and new fuel elements are arranged in the outer part of the core, so as to get the fuel burning as uniformly as possible. A schematic map of the reactor core is drawn in figure 3.18 [96]. The detector was located in an underground laboratory about 1 km from the neutrino source (figure 3.17), providing a overburden of 300 MWE, reducing the external cosmic ray muon flux to a value 0.4 $\mathrm{m^{-2}\ s^{-1}}$, decreasing the background caused by fast neutrons produced by muon-induced nuclear spallations in the materials surrounding the detectors. It was installed in a cylindrical vessel 5.5 m in diameter and 5.5 m deep, which was surrounded by 75 cm of low radioactivity sand and covered by 14 cm of cast iron, to protect it from the natural radioactivity of the rock.

The detector comprised three concentric regions (see figure 3.19) [96]:

- a central 5–ton target in a transparent container (total mass = 117 kg) filled with a 0.09% Gd–loaded scintillator ("Region I");
- an intermediate 17–ton region (70 cm thick) equipped with 192 eight–inch PMT's used to protect the target from PMT radioactivity and to contain the gamma rays from neutron capture ("Region II");
- an outer 90–ton optically separated active cosmic–ray muon veto shield (80 cm thick) equipped with two rings of 24 eight–inch PMT's ("Region III").

The target region contained a Gd-loaded liquid scintillator. The neutrino detection was based on the delayed coincidence between the prompt positron signal generated by reaction (3.16), boosted by the annihilation γ-rays, and the signal associated with the γ-ray emission following the neutron capture reaction

$$n + \mathrm{Gd} \rightarrow \mathrm{Gd}^{\star} \rightarrow \mathrm{Gd} + \sum_i \gamma_i \tag{3.22}$$

The choice of a Gd-doping was to maximize the neutron capture efficiency; Gadolinium has the highest thermal neutron cross section. Moreover, the large total γ-ray energy makes easy to discriminate the neutron capture from the natural radioactivity [96].

The inner detector volume was separated from Region II by a transparent vessel, a vertical cylindrical surface closed by two hemispherical end-caps. The outer radius of the cylinder and of the end-caps was 90 cm, the height of the cylinder was 100 cm, and the height of the complete neutrino target region was 280 cm.

The ratio of the number of measured events and that expected without neutrino oscillations is

$$R_{\text{Chooz}} = 1.01 \pm 0.04. \tag{3.23}$$

This value puts a constraint on the disappearance of electron (anti)neutrinos with energies in the MeV range at distances smaller than about 1 km. This corresponds to a constraint on $\sin^2 2\theta$ for $\Delta m^2 \gtrsim 10^{-3}\,\text{eV}^2$. In the range of sensitivity of the Gallium radioactive source experiments, $\Delta m^2 \gtrsim 10^{-1}\,\text{eV}^2$ (see figures 3.8), the oscillation length of reactor antineutrinos is much shorter than the Chooz source-detector distance. In this case, the Chooz experiment is only sensitive to the averaged survival probability

$$\langle P^{\;(-)\;\;(-)}_{\nu_e\to\nu_e}\rangle = 1 - \frac{1}{2}\,\sin^2 2\theta\,. \tag{3.24}$$

This can be understood looking at the figure 2.1. For the Chooz baseline and energies, one has $\langle L/E\rangle \approx 10^3$ m/MeV, so that for the range of sensitivity of the Gallium radioactive source experiments on Δm^2, we have $\Delta m^2\,\langle L/E\rangle \gtrsim 10^2$, leading to equation (3.24).

Therefore, the Chooz result in equation (3.23) can be combined[5] with the results of the Gallium radioactive source experiments simply by considering it as a measurement of $\sin^2 2\theta$: in the Bayesian approach of equation (3.8)

$$\sin^2 2\theta < 0.071,\ 0.15,\ 0.23\,, \tag{3.25}$$

at 68.27% (1σ), 95.45% (2σ), 99.73% (3σ) Bayesian Confidence Level, respectively.

First, we performed a combined frequentist least-squares analysis of the Bugey and Chooz data, which yielded the allowed regions in the $\sin^2 2\theta$–Δm^2 plane shown in figure 3.21, the best fit values of the mixing parameters reported in table 3.12, and the marginal allowed ranges listed in table 3.13. One can see that the addition of the Chooz result to the Bugey data analysis has the effect of improving slightly the upper limit on $\sin^2 2\theta$ for $\Delta m^2 \gtrsim 3\,\text{eV}^2$ and that of excluding values of $\sin^2 2\theta$ larger than about 0.1 for $\Delta m^2 \lesssim 3\times 10^{-2}\,\text{eV}^2$, where Bugey is not sensitive. In the intermediate range of Δm^2, where Bugey is sensitive to the oscillations, the addition of the Chooz result weakens the hint in favor of oscillations given by the Bugey data:

[5] In our figures we considered Δm^2 in the range $10^{-3} - 10^2\,\text{eV}^2$. For simplicity, we neglected the small Δm^2 dependence of the CHOOZ exclusion curve for $\Delta m^2 \lesssim 4\times 10^{-2}\,\text{eV}^2$ (see figure 55 of reference [96]).

		Ga+Bug	Bug+Cho	Gal+Cho	Gal+Bug+Cho
No Osc.	$\chi^2_{\rm min}$	59.15	51.01	8.27	59.22
	NDF	59	56	5	60
	GoF	0.470	0.664	0.142	0.504
Osc.	$\chi^2_{\rm min}$	53.48	47.99	6.70	54.30
	NDF	57	54	3	58
	GoF	0.608	0.704	0.082	0.614
	$\sin^2 2\theta_{\rm bf}$	0.055	0.041	0.078	0.050
	$\Delta m^2_{\rm bf}$ (eV^2)	1.965	1.965	1.905	1.965
PG.	$\chi^2_{\rm min}$	3.16	0.62	3.76	3.99
	NDF	2	1	1	3
	GoF	0.206	0.430	0.053	0.263

Table 3.12: Results for fit of the different combinations of the Gallium radioactive source experiments and the Bugey and Chooz reactor experiments. The first three lines correspond to the case of no oscillations (No Osc.). The following five lines correspond to the case of oscillations (Osc.). The last three lines describe the parameter goodness-of-fit (PG) [93].

Parameter	C.L.	Gal+Cho	Bug+Cho	Gal+Bug+Cho
$\sin^2 2\theta$	68.27%(1σ)	$0.016 - 0.14$	$0.017 - 0.085$	$0.028 - 0.073$
	95.45%(2σ)	–	–	$0.005 - 0.123$
	99.73%(3σ)	–	–	–
Δm^2 [eV^2]	68.27%(1σ)	> 0.59	$1.91 - 1.99$	$1.92 - 1.99$
	95.45%(2σ)	–	–	> 0.78
	99.73%(3σ)	–	–	–

Table 3.13: Allowed ranges of $\sin^2 2\theta$ and Δm^2 from the combined fit results of Bugey and Chooz reactor experiment, the Gallium radioactive source experiments and the Chooz reactor experiment and the Gallium radioactive source experiments and the Bugey and Chooz reactor experiments. The dash indicates the absence of limits.

the 1σ allowed regions in figure 3.14 are stretched towards small values of $\sin^2 2\theta$ in figure 3.21. However, the best-fit value of the mixing parameters remain unchanged, because of the dominance of the Bugey data. From table 3.12, one can see that the parameter goodness-of-fit implies that Bugey and Chooz results are compatible under the hypothesis of neutrino oscillations, but the goodness-of-fit obtained in the case of no oscillations do not allow us to exclude this possibility.

From the comparison of equation (3.24) and figure 3.8, one can see that the results of the Chooz and the Gallium radioactive source experiments are compatible only at the 2σ level. In fact the parameter goodness-of-fit reported in table 3.12 shows a tension

between Gallium and Chooz data under the hypothesis of neutrino oscillations. Figure 3.22 shows the allowed regions in the $\sin^2 2\theta$–Δm^2 plane obtained with the combined least-squares fit of Gallium and Chooz data. The values of $\chi^2_{\rm min}$ and Goodness of Fit and the best-fit values of the mixing parameters are given in table 3.12. It is clear that the combined fit is not good, since the results of Chooz and the Gallium radioactive source experiments are in contradiction regarding neutrino disappearance. The marginal allowed ranges of $\sin^2 2\theta$ and Δm^2 in table 3.13 are of little interest, since the minima of the corresponding $\Delta\chi^2$'s in figure 3.22 are very shallow, except for the upper bound on $\sin^2 2\theta$ driven by Chooz data. As one can see from the allowed regions in the $\sin^2 2\theta$–Δm^2 plane in figure 3.22, the Chooz bound on $\sin^2 2\theta$ in equation (3.24) is weakened by the results of the Gallium radioactive source experiments in a significant way only for $\Delta m^2 \gtrsim 10^{-1}\,\mathrm{eV}^2$ at the 1σ level.

A combined fit of the results of Bugey, Chooz, and Gallium data was also done. The resulting allowed regions in the $\sin^2 2\theta$–Δm^2 plane are shown in figure 3.23. The best fit values and the marginal allowed ranges of the mixing parameters are listed, respectively, in tables 3.12 and 3.13. One can see that the Gallium and Chooz data tend to compensate each other, leading to results which are similar to those obtained in the analysis of Bugey data alone. The value of the parameter goodness-of-fit reported in table 3.12 does not allow us to exclude the compatibility of the Bugey, Chooz and Gallium data under the hypothesis of neutrino oscillations. Also the goodness-of-fit obtained in the case of no oscillations is acceptable. Therefore, we can conclude that the combined analysis of all the experimental data that we have considered is compatible both with the case of no oscillations and with the hint in favor of neutrino oscillations with $0.02 \lesssim \sin^2 2\theta \lesssim 0.07$ and $\Delta m^2 \approx 1.95\,\mathrm{eV}^2$ found in the analysis of Bugey data.

3.3 Summary

In the present analysis, we interpreted the deficit observed in the Gallium radioactive source experiments as a possible indication of the disappearance of electron neutrinos. In the framework of two-neutrino mixing, we found that there is an indication of electron neutrino disappearance due to neutrino oscillations with $\sin^2 2\theta \gtrsim 0.03$ and $\Delta m^2 \gtrsim 0.1\,\mathrm{eV}^2$.

Studying the compatibility of the data of the Gallium radioactive source experiments with the data of the Bugey and Chooz reactor short-baseline antineutrino disappearance experiments, we found that the Bugey data present a hint of neutrino oscillations with $0.02 \lesssim \sin^2 2\theta \lesssim 0.08$ and $\Delta m^2 \approx 1.95\,\mathrm{eV}^2$, which is compatible with the region of the mixing parameters allowed by the analysis of the data of the Gallium radioactive source experiments.

The different combined analyses of the Gallium, Bugey and Chooz experimental data show compatibility between the two nuclear reactor experiments, between Gallium and Bugey experiments, and a marginal compatibility between Gallium and Chooz. The weak indication in favor of neutrino oscillations found in the analysis of the Bugey data persists in the combined analyses of the Bugey data with the Gallium and Chooz

data. Nevertheless, the no oscillations hypothesis cannot be excluded.

Note that this squared-mass difference is too large to be compatible with the three-neutrino mixing scheme inferred from the observation of neutrino oscillations in solar, very-long-baseline reactor, atmospheric and long-baseline accelerator experiments, in which there are only two independent squared-mass differences, $\Delta m^2_{\rm sol} \approx 8 \times 10^{-5}\,{\rm eV}^2$ and $\Delta m^2_{\rm atm} \approx 3 \times 10^{-3}\,{\rm eV}^2$. Therefore, the results of our analysis indicate the possible existence of at least one light sterile neutrino ν_s (see references [98, 99, 15]).

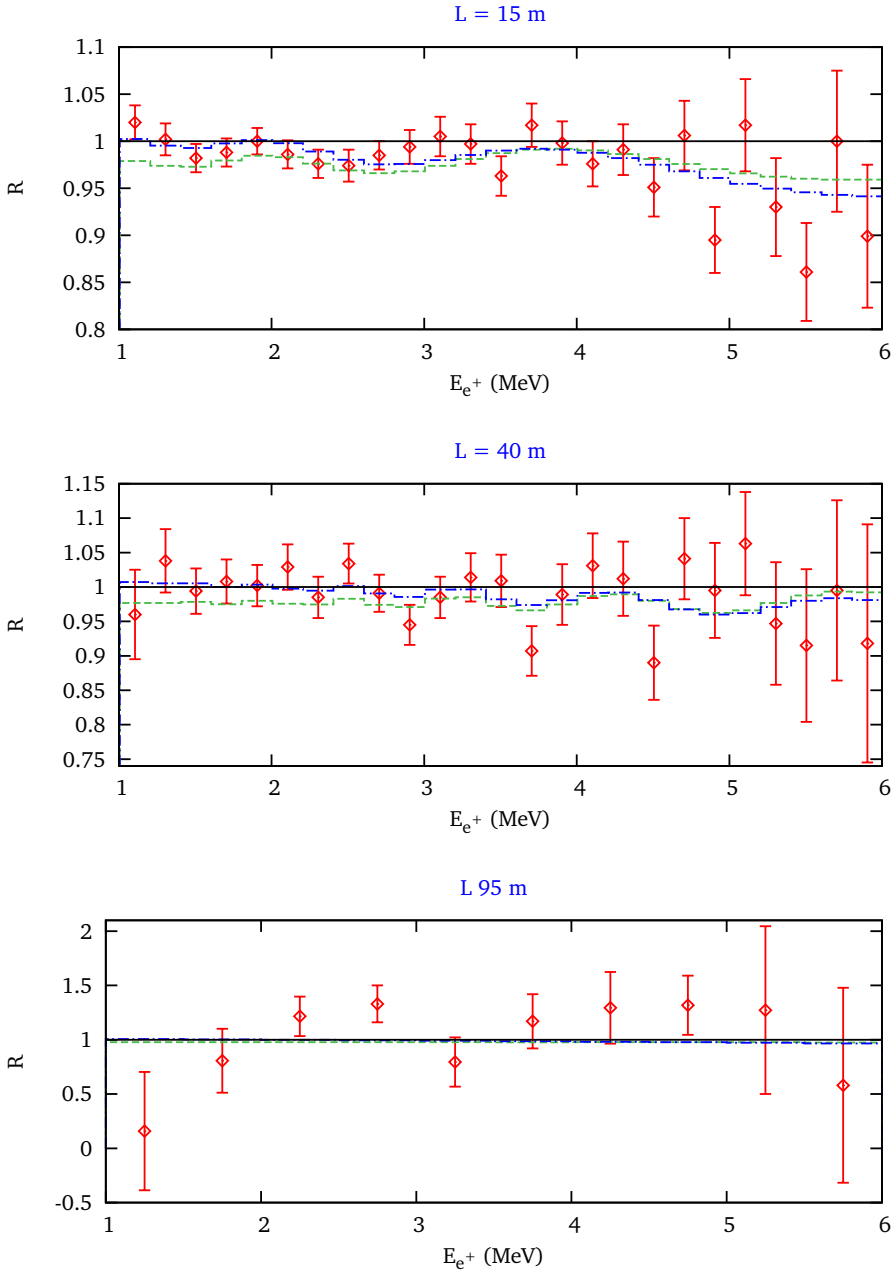

Figure 3.15: Best fit of Bugey data (points with error bars [90]). The three panels show the ratio R of observed and expected (in the case of no oscillation) event rates at the three source-detector distances in the Bugey experiment as functions of the measured positron kinetic energy E (see equation (3.20)). In each panel, the dash-dotted and dashed histograms correspond, respectively, to the best-fit values of $(Aa_j + b\,(E_{ji} - E_0))\,R_{ji}^{\rm the}$ and $R_{ji}^{\rm the}$ (see equation (3.19)).

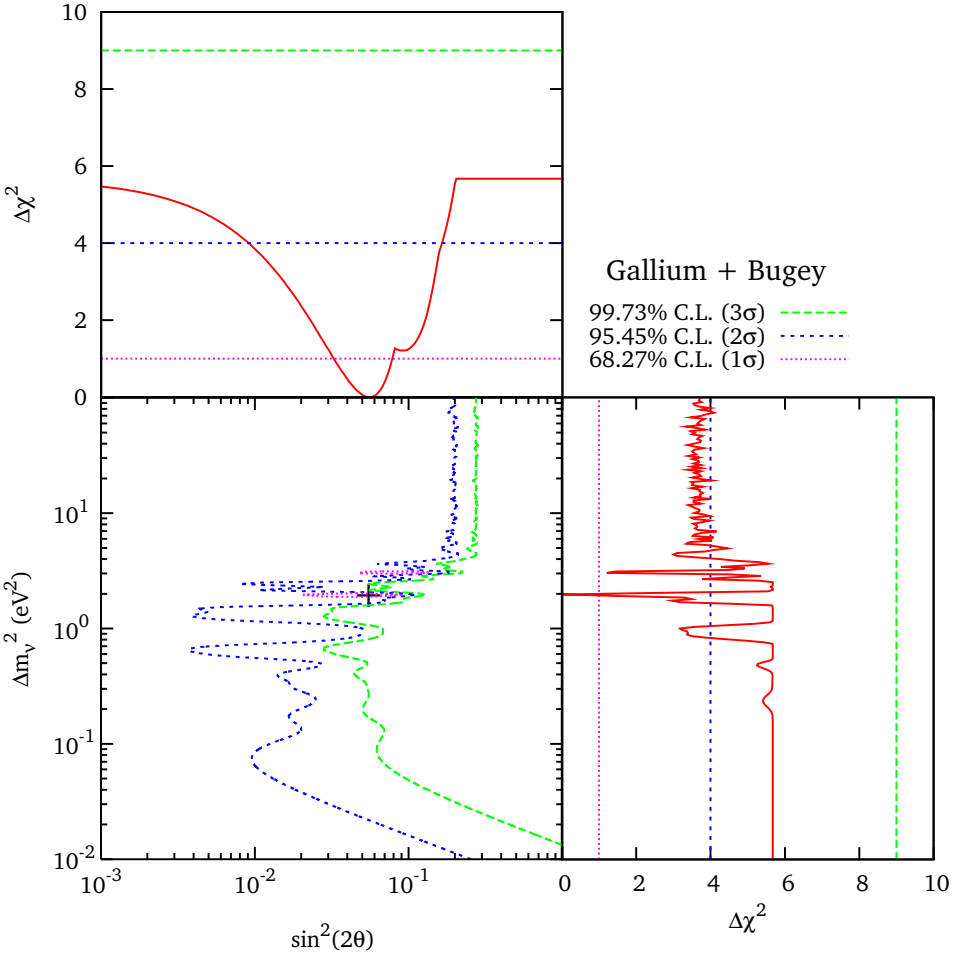

Figure 3.16: Allowed regions in the oscillation parameter space and marginal $\Delta\chi^2$s for $\sin^2 2\theta$ and Δm^2 obtained from the combined fit of the results from the two GALLEX ^{51}Cr radioactive source experiments, the SAGE ^{51}Cr and ^{37}Ar radioactive source experiments and the Bugey reactor experiment. The best fit point corresponding to $\chi^2_{\rm min}$ is indicated by a cross.

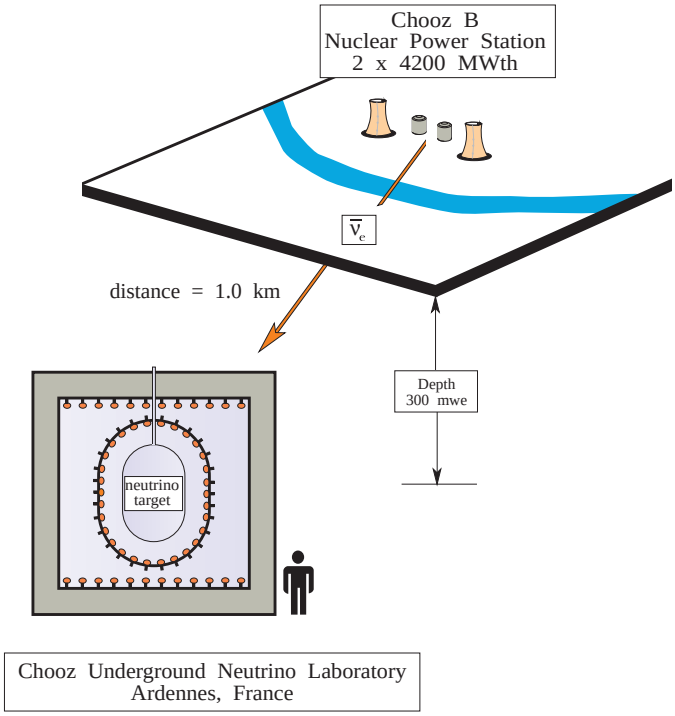

Figure 3.17: Chooz experimental site overview [94, 95].

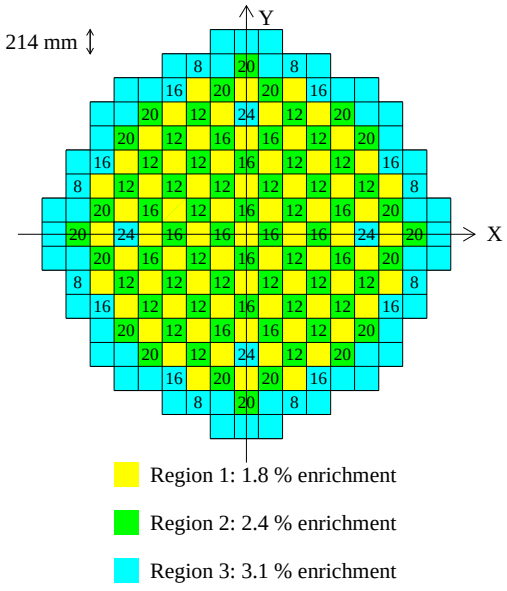

Figure 3.18: Schematic view of the fuel rods in the core of the Chooz reactor. The number of Boron poison rods assambled with each fuel element is also indicated [96].

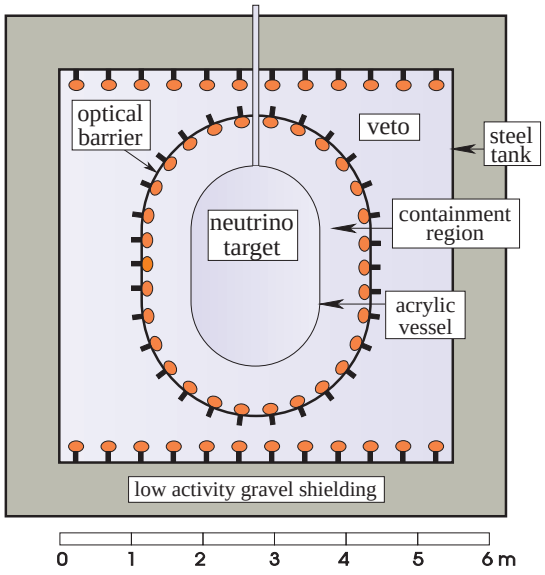

Figure 3.19: Schematic view of the Chooz detector [97].

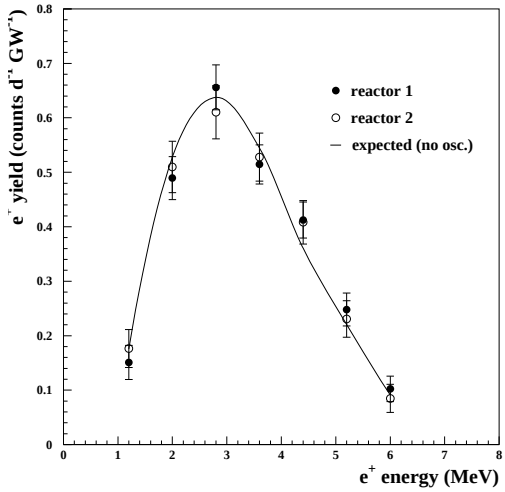

Figure 3.20: Positron yields for the two reactors, as compared with the expected yield for no oscillations [96].

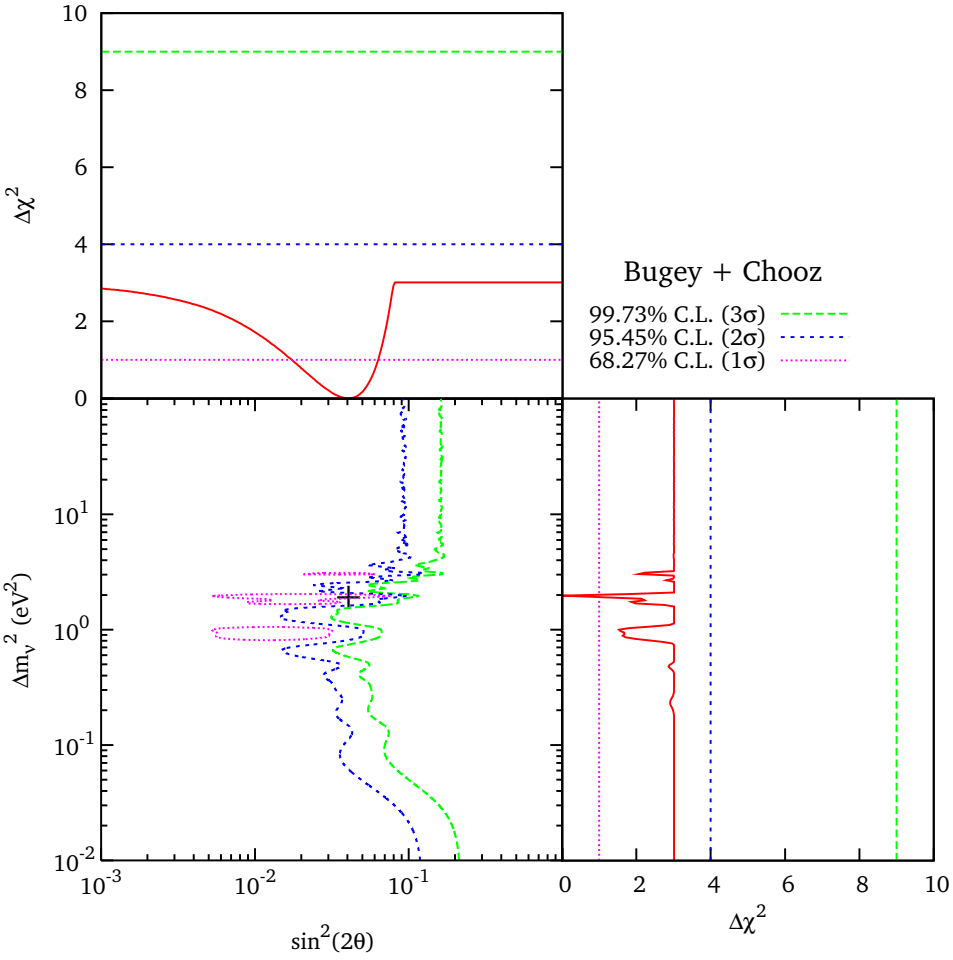

Figure 3.21: Allowed regions in the oscillation parameter space and marginal $\Delta\chi^2$s for $\sin^2 2\theta$ and Δm^2 obtained from the combined fit of the Bugey and Chooz nuclear reactor experiment. The best fit point corresponding to χ^2_{min} is indicated by a cross.

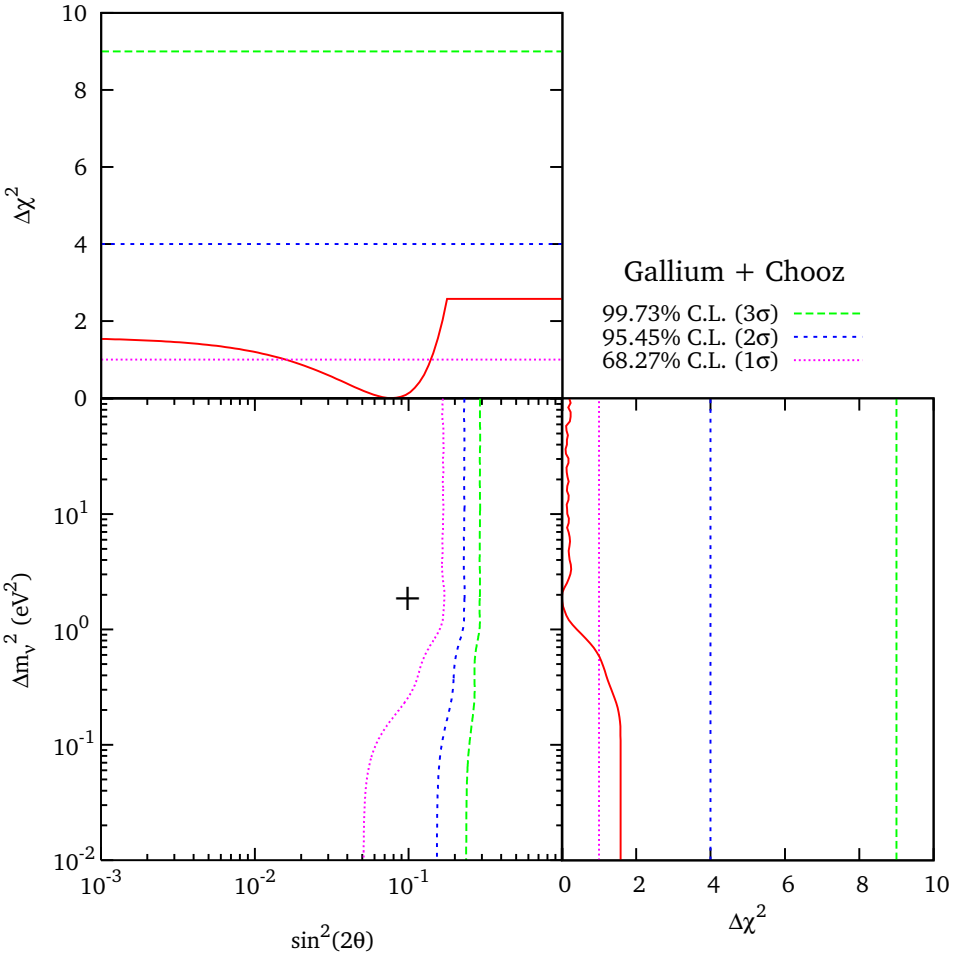

Figure 3.22: Allowed regions in the oscillation parameter space and marginal $\Delta\chi^2$s for $\sin^2 2\theta$ and Δm^2 obtained from the combined fit of the Gallium radioactive source experiments and the Chooz nuclear reactor experiment. The best fit point corresponding to $\chi^2_{\rm min}$ is indicated by a cross.

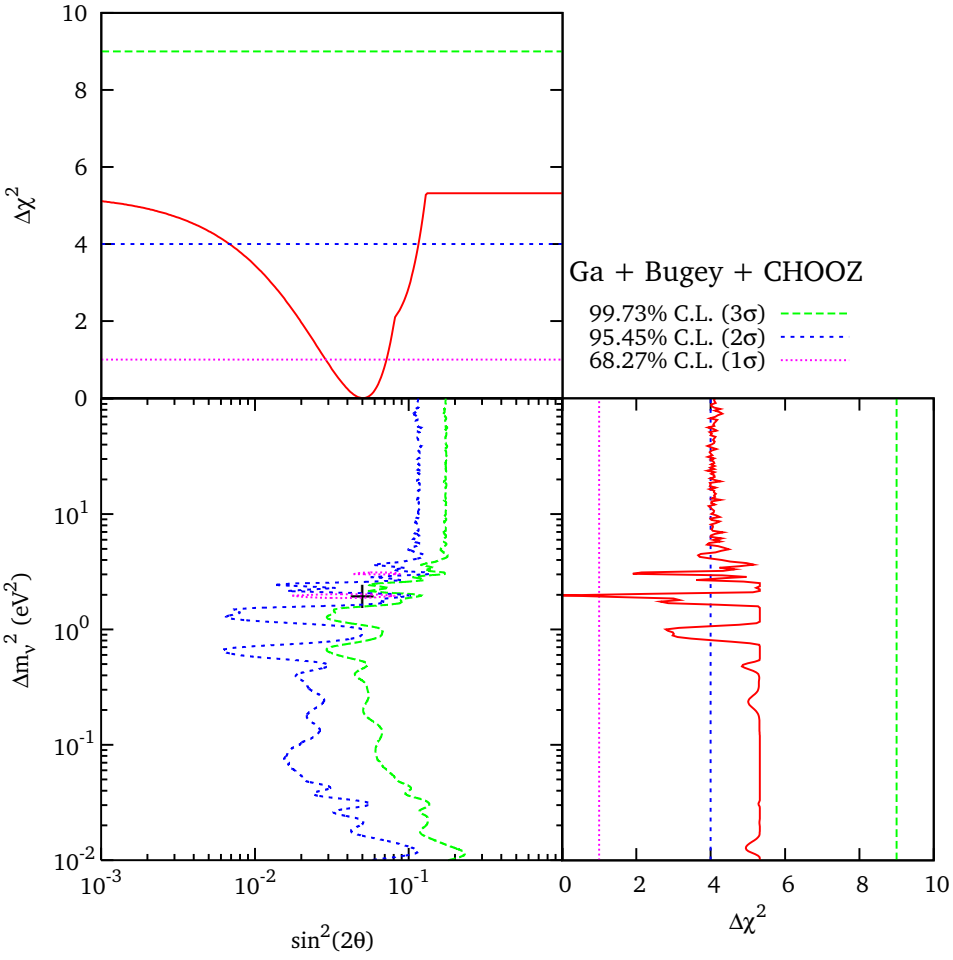

Figure 3.23: Allowed regions in the oscillation parameter space and marginal $\Delta\chi^2$s for $\sin^2 2\theta$ and Δm^2 obtained from the combined fit of the Gallium radioactive source experiments and the Bugey and Chooz nuclear reactor experiments. The best fit point corresponding to χ^2_{min} is indicated by a cross.

CHAPTER 4

OTHER NUCLEAR REACTOR EXPERIMENTS

So far, the results of the previous chapter show a hint of electron neutrino disappearance, which could be interpreted as an effect of neutrino oscillations. This indication appears in a region of the square-mass differences which is much larger than those found in the Solar and Atmospheric neutrino oscillation experiments, so that it could be considered as an indication of new physics beyond the standard model of neutrino oscillations.

The analysis presented in chapter 3 shows an acceptable compatibility of the experimental data from Gallium radioactive source experiments and Bugey and Chooz nuclear reactor experiments, in favor of the hint of neutrino oscillations. The inclusion of additional data could be useful to study the robustness of this result.

In this chapter, the analysis of the experimental results from the I.L.L., S.R.S. and Gösgen nuclear reactor experiments is presented, with a short description of each of them. Then, the compatibility of the results of the previous chapter is studied, by making different combined analyses of the data sets.

4.1 I.L.L.

The I.L.L. nuclear reactor experiment [100] was carried out at the Institut Laue-Langevin in Grenoble, France.

The inverse β-decay equation (3.16) was used as the detection reaction. The energy of the produced positrons is related to the neutrino energy through equation (3.17), so that the positron energy spectrum gives direct information about the neutrino spectrum. A deviation of the measured positron spectrum from that expected without oscillations would indicate the presence of neutrino oscillations.

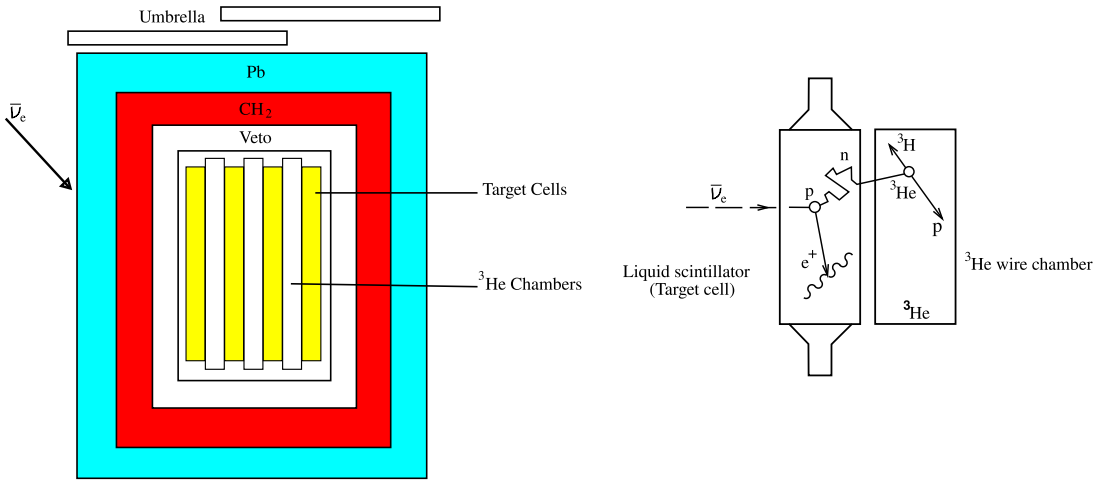

Figure 4.1: *(Left)* Experimental arrangement of the detector system and shielding [100]. *(Right)* Representation of the reaction used for the detection process.

For the experiment, a reactor of 57 MW thermal power was used[1], with fuel element consisting of 8.5 kg of 93% enriched ^{235}U in the form of UAl_3. This ILL reactor had a source strength of 9.5×10^{18} electron antineutrinos per second [100].

The reactor core was a cylinder, 40 cm in diameter and 80 cm in height, size that makes the reactor very good to study short oscillation lengths for which the effects would be averaged out in measurements in a power reactor.

Considering the importance of the energy resoution for the oscillation experiments, the ILL detector was designed with special care on the positron-energy resolution, as well as on low background and high detection efficiency, in order to get a sensitivity between 0.1 and 5 eV^2 for Δm^2. This detector system was located at an effective distance of 8.76m from the reactor core, in the basement of the reactor building. It was constructed as a multilayer 'sandwich' of five liquid-scintillator planes and four ^{3}He-wire-counter planes as shown in figure 4.1.

In the detection process, the antineutrino interacts with a proton of the liquid scintillator generating a positron and a neutron, as show in figure 4.1. The positron slows down by ionization in the liquid scintillator, producing a prompt light pulse proportional to the energy of the positron. The neutron is thermalized in the target cells within a few μs and diffuses into the ^{3}He counter. The neutron is captured in a ^{3}He counter via the reaction

$$n + {}^3\mathrm{He} \rightarrow p + {}^3\mathrm{H} + 765 \text{ keV}. \tag{4.1}$$

Both the p and the ^{3}H are detected in a ^{3}He wire counter. A delayed coincidence between target cells and ^{3}He counter pulses is the signature of a good event [100].

[1]According to reference [101], this values is not correct, because of the wrong operating power of the high-flux reactor reported in the beginning of its operation.

The detector system used a total of 30 target cells with outside dimensions of $9 \times 20 \times 88\times$ cm^3. The cells were thick enough for neutron thermalization, but as thin as necessary to prevent excessive neutron absorption [100]. Each target cell was viewed at both ends by two PMTs. The target-cell energy resolution is 18% full width at half maximum (FWHM)[2] at 0.91 MeV.

For the analysis presented in this Thesis, the experimental data were taken from the ratio of experimental spectrum to the theoretical spectrum (in the absence of oscillations), shown in reference [101], instead of those shown in table IV of [100]. This is because in reference [101] a reanalysis of the ILL data was done considering corrections in the full power of the reactor, which affected the computation and results of the theoretical spectrum.

We analyze these data with a least-square analysis, defining the χ^2-function

$$\chi^2 = \sum_{i=1}^{16} \frac{\left(\alpha R_i^{\text{the}} - R_i^{\text{exp}}\right)^2}{\sigma_i^2} + \frac{(\alpha - 1)^2}{\sigma_\alpha^2}, \tag{4.2}$$

where α is a global normalization factor to account uncertainties in the measured positron energy, with $\sigma_\alpha = 8.87\%$ [101]. We compute R_i^{the} using equation (3.6), considering the source-detector distance $L = 8.76$ m and the reactor core and source dimensions for the integration over the neutrino path, using a Monte Carlo, and considering the (Gaussian) energy resolution function $F(E, T_e)$ with standard deviation $\sigma = 0.069\sqrt{E/(0.91\,\text{MeV})}$ MeV.

The procedure consists in the minimization of the χ^2-function (4.2) with respect to α, to get the χ^2 values for each value of the oscillation parameters $(\sin^2 2\theta, \Delta m^2)$. In this case, taking into account the short-baseline of this experiment, we decided to limit the analysis to the range $(10^{-2} \leq \Delta m^2 \leq 5)$ eV^2.

The allowed regions in the oscillation parameter space resulting from the analysis of the ILL reactor experiment are shown in figure 4.2. The value of the χ^2_{min}, the number of degrees of freedom (NDF) and the goodness-of-fit (GoF) and the best fit of the oscillation parameters are given in table 4.1, together to the marginal allowed ranges of $\sin^2 2\theta$ and Δm^2 obtained from the corresponding $\Delta\chi^2$'s in figure 4.2.

One can see that there are allowed regions in the oscillation parameter space at 1σ for $0.1 \leq \sin^2 2\theta \leq 0.3$ and around $\Delta m^2 \approx 3.8\text{eV}^2$ and $\Delta m^2 \approx 2.4\text{eV}^2$, as well as at 2σ for $0.05 \leq \sin^2 2\theta \leq 0.4$ and around $\Delta m^2 \approx 3.8\text{eV}^2$, $\Delta m^2 \approx 2.4\text{eV}^2$ and $\Delta m^2 \approx 0.9\text{eV}^2$. The value of the goodness-of-fit (87%) indicates that the fit is good, and much better than the no oscillation hypothesis (goodness-of-fit of 32%). In addition, this result is very similar to the one presented in reference [101], whose best fit is indicated in figure 4.2 by an asterisk ($\sin^2 2\theta = 0.31$, $\Delta m^2 = 2.23$ eV^2 [101]). As a way to test the results, we also show the histogram relative to the best fit, compared to the ILL R_i^{exp}s, in figure 4.3. One can see that the fit is rather good, but the error bars so large enough that it is not possible to exclude the no oscillation hypothesis.

[2] A full width at half maximum (FWHM) is an expression of the extent of a function, given by the difference between the two extreme values of the independent variable at which the dependent

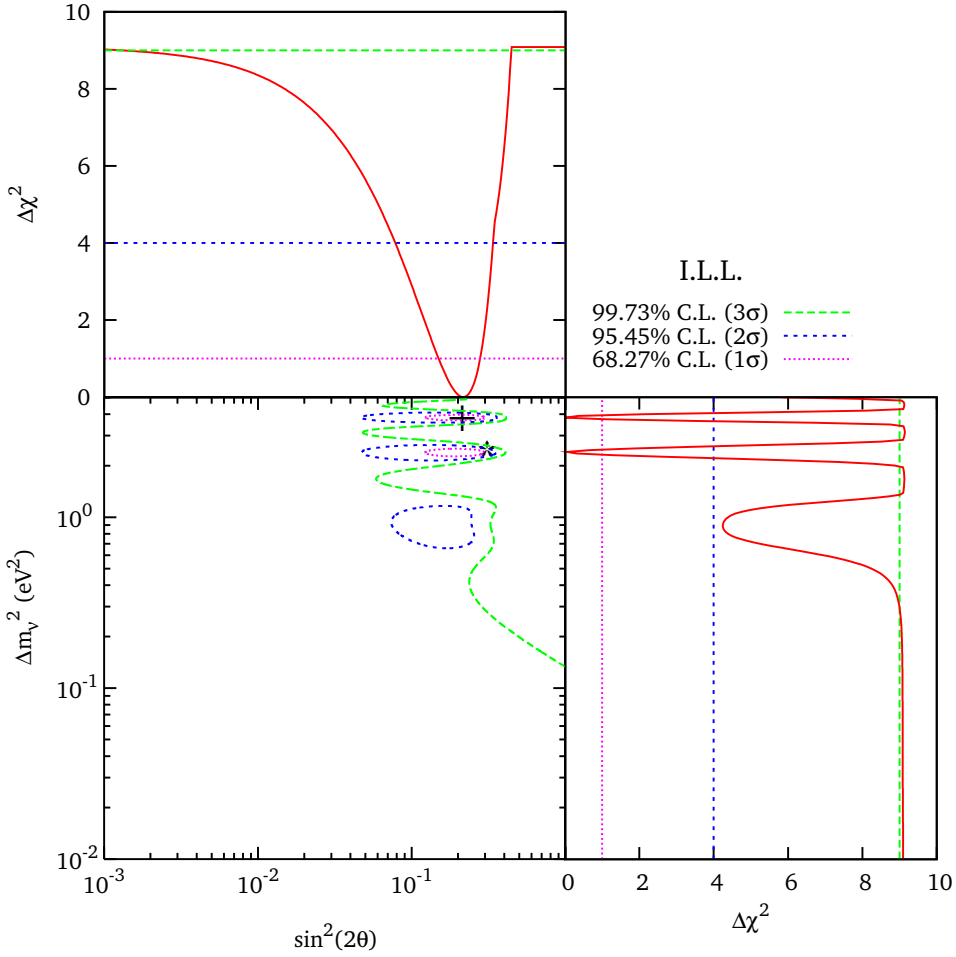

Figure 4.2: Allowed regions in the oscillation parameter space and marginal $\Delta\chi^2$s for $\sin^2 2\theta$ and Δm^2 obtained from the analysis of the ILL nuclear reactor experiment. The best fit point corresponding to χ^2_{min} is indicated by a cross.

As in the case of the Gallium radioactive source experiments, here there are allowed ranges coming from the marginal $\Delta\chi^2$ curves, giving an indication of a possible neutrino disappearance due to neutrino oscillations. Furthermore, comparing the results from the Gallium experiments in figure 3.9 and those from the ILL reactor experiments, there seems to be a compatibility between them.

However, before doing a combined fit of the Gallium and the ILL experiments, we decided to try the combined fit of the two reactor experiments, ILL and Bugey. By comparing the allowed regions obtained from ILL, in figure 4.2 with those from

variable is equal to half of its maximum value. When the considered function is the normal (Gaussian) distribution, the relationship between FWHM and the standard deviation σ is FWHM $= 2\sqrt{2\ln 2}\sigma$.

	I.L.L.		Parameter	C.L.	Range
No Osc.	$\chi^2_{\rm min}$	16.95	$\sin^2 2\theta$	$68.27\%(1\sigma)$	$0.15 - 0.28$
	NDF	15		$95.45\%(2\sigma)$	$0.08 - 0.33$
	GoF	0.322		$99.73\%(3\sigma)$	> 0.43
Osc.	$\chi^2_{\rm min}$	7.81	$\Delta m^2\,[{\rm eV}^2]$	$68.27\%(1\sigma)$	$2.2 - 3.9$
	NDF	13		$95.45\%(2\sigma)$	$2.0 - 3.9$
	GoF	0.856		$99.73\%(3\sigma)$	> 0.19
	$\sin^2 2\theta_{\rm bf}$	0.214			
	$\Delta m^2_{\rm bf}$ (eV^2)	3.820			

Table 4.1: Results for fit of ILL nuclear reactor experiment. The first three lines correspond to the case of no oscillations (No Osc.). The following five lines correspond to the case of oscillations (Osc.) Also shown the marginal allowed regions for the oscillation parameters.

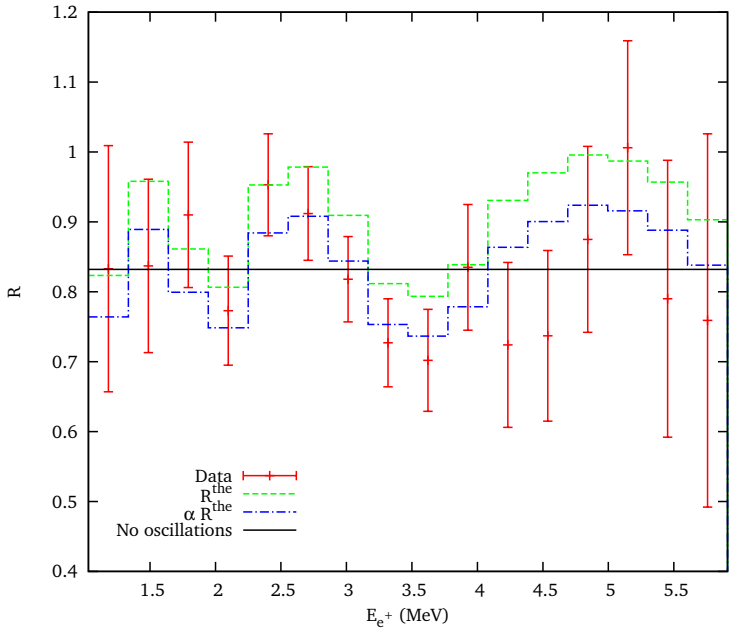

Figure 4.3: Best fit of ILL data (points with error bars [101]). The plot shows the ratio R of observed and expected (in the case of no oscillation) positron spectrum at the source-detector distance $L = 8.76$ m in the ILL experiment as a function of the measured positron kinetic energy E. The dashed and dot-dashed histograms correspond, respectively, to the best-fit values of $R^{\rm the}_{ji}$ and $\alpha\, R^{\rm the}_{ji}$ (with $\alpha = 0.928$) (see equation (4.2)).

		Bug+ILL
No Osc.	$\chi^2_{\rm min}$	67.89
	NDF	70
	GoF	0.549
Osc.	$\chi^2_{\rm min}$	64.41
	NDF	68
	GoF	0.601
	$\sin^2 2\theta_{\rm bf}$	0.044
	$\Delta m^2_{\rm bf}$ (eV^2)	1.965
PG.	$\chi^2_{\rm min}$	11.04
	NDF	2
	GoF	0.004

Table 4.2: Results for fit of the combination of the Bugey and I.L.L. reactor experiments. The first three lines correspond to the case of no oscillations (No Osc.). The following five lines correspond to the case of oscillations (Osc.). The last three lines describe the parameter goodness-of-fit (PG) [93].

Bugey in figure 3.14, we see that these two experiments appear to be only marginally compatible. Doing the combined analysis, we found that, even though the best fit is almost the same to that obtained from the Bugey data alone (see the third column of table 4.2), and the goodness-of-fit for the oscillation hypothesis is high (60%), it is clear that there is a significant incompatibility between the two data sets, as indicated by 0.4% the parameter goodness-of-fit in table 4.2.

Based on these results, we decided not to present any additional combined fit including the ILL data set.

4.2 S.R.S.

The SRS (Savannah River Site) nuclear reactor neutrino experiment was designed to search for neutrino oscillations of the form $\overline{\nu}_e \leftrightarrow \nu_x$ ($\overline{\nu}_e$ disappearance), in the range of $\Delta m^2 > 0.01$ eV^2, detecting neutrinos by observing the inverse β-decay reaction (3.16) in a liquid scintillator detector [102].

The method used in the experiment was to measure and compare the inverse β-decay reaction rated and corresponding positron energy spectra at two distances from the reactor. Two independent features of the data are considered in the analysis [102]:

- Spectral shape. If the shapes of the positron spectra of the two positions are different, this could be an indication of neutrino oscillations. However, for large Δm^2 (≥ 10 eV^2), the shape measurement is insensitive to oscillations.

- Absolute rate. The event rate at each detector location is compared with the theoretical predicted rate. The absolute measurement is sensitive to neutrino

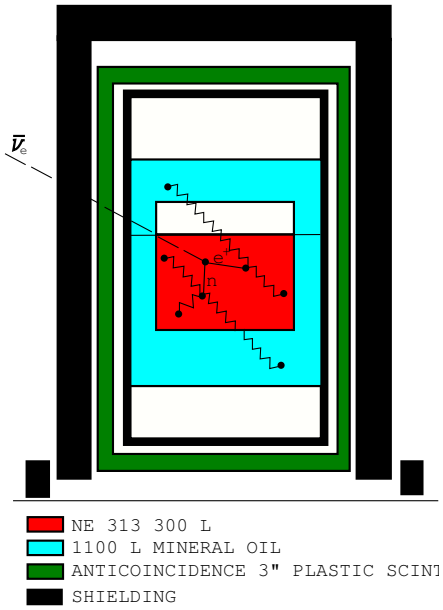

Figure 4.4: Configuration of the neutrino oscillation detector used by the SRS experiment [102, 104].

oscillations with large Δm^2.

The experiment was carried out at the Savannah River Site (SRS) in Aiken, South Carolina, with a detector located about 12m below the reactor center. A system which allowed to move the detector was used, in order to measure oscillations at two distances: $L_1 = 18.18 \pm 0.03$m and $L_2 = 23.82 \pm 0.03$m [102, 103].

At SRS, the power reactor was operating at 2000 MW_{th}, producing a flux of $\approx 10^{13}\,\overline{\nu}_e$ s^{-1} cm^{-2} at 20 m from the core. Since the SRS reactor was a production facility for Plutonium and Tritium, the neutrinos were generated from a relatively pure fuel made of ^{235}U.

The detector was designed to detect inverse β-decays by observing a signal from the positron followed by a signal from the capture of the neutron, taking care, also, of the discrimination of the possible backgrounds. Figure 4.4 shows the major components of the detector [102]:

- The target tank in which the inverse β reactions are observed, is a cylindrical stainless steel tank containing about 275 liters of a scintillator loaded with 0.5% gadolinium, which provides fast, highly efficient neutron detection. The target is viewed by 21 five-inches PMTs.

- The blanket detector contains 1100 liters of a mineral oil scintillator and is optically divided in two sectors, each viewed by 30 five-inches PMTs. It is used as

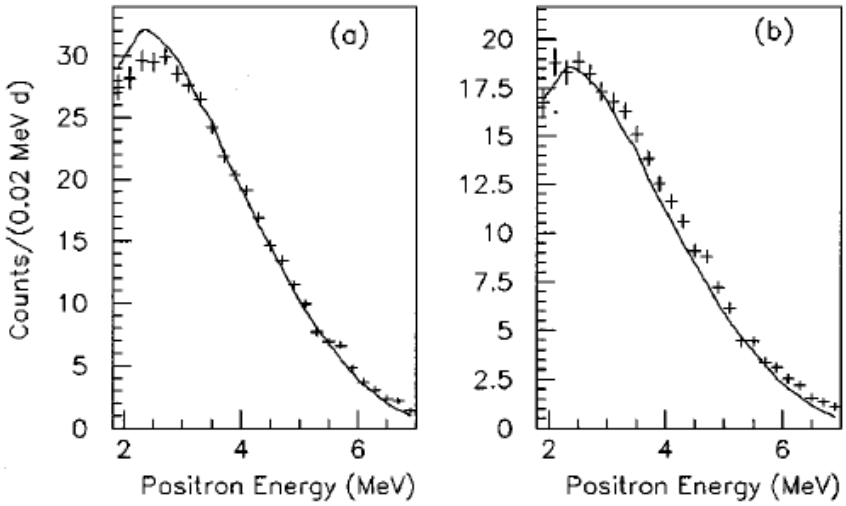

Figure 4.5: Positron spectra normalized for reactor power for the two source-detector distances used in the SRS experiment. The solid line corresponds to the Monte Carlo predictions assuming no oscillations [102].

an active anticoincidence and as an additional active volume which participates in the detector trigger.

- The inner lead shield against gammas and charged particles that may penetrate through or be created in the outer lead shield.

- The anticoincidence shield is a plastic scintillator which surrounds the inned shield used as a veto of cosmic rays.

- The outer lead shield which surrounds the anticoincidence shield, used to reduce the flux of gamma radiation associated with the β-decay of ^{16}N in the water of the heat exchangers above the experiment.

The detection technique consists in the distinction of the signature of an inverse β-decay process, fromed by a positron pulse, a scintillation flash in the target having the pulse shape characteristics of a positron; the energy in the target must exceed 1 MeV; and a light pulse following the positron pulse within 31.5μs; the total energy detected in the target plus blankets for this pulse must exceed $\sim$ 4 MeV.

The final data sample is shown in figure 4.5 (from [102]), in the form of the positron spectra normalized for reactor power for the two source-detector distances. These are the data used in the present Thesis, by making a least-squares analysis with the χ^2-

S.R.S.		
No Osc.	$\chi^2_{\rm min}$	130.24
	NDF	50
	GoF	4.5×10^{-9}
Osc.	$\chi^2_{\rm min}$	122.27
	NDF	48
	GoF	2.1×10^{-8}
	$\sin^2 2\theta_{\rm bf}$	1.0
	$\Delta m^2_{\rm bf}$ (eV^2)	0.023

Table 4.3: Results for the fit of the S.R.S. reactor experiment. The first three lines correspond to the case of no oscillations (No Osc.). The following five lines correspond to the case of oscillations (Osc.).

function defined as

$$\chi^2_{\rm SRS} = \sum_{j=2}^{2} \left[\sum_{i=1}^{26} \left(\frac{a_j R^{\rm the}_{ji} - R^{\rm exp}_{ji}}{\sigma_{ji}} \right)^2 + \left(\frac{a_j - 1}{\sigma_{\rm sys}} \right)^2 \right], \tag{4.3}$$

where a_j are normalization factors to account for systematic uncertainties in the measurements at each position of the detector; $R^{\rm exp}_{ji}$ is computed as

$$R^{\rm exp}_{ji} = \left(\frac{\text{Measured positron spectra}}{\text{MC predicted positron spectra}} \right)_{ji}, \qquad j = 1, 2; \quad i = 1, \cdots, 26. \tag{4.4}$$

Here (and in equation (4.3)), $j = 1$ corresponds to the data for the source-detector distance $L_1 = 18.18$ m and $j = 2$ corresponds to the data for the source-detector distance $L_2 = 23.82$ m. The measured and the MC predicted positron spectra are extracted from figure 4.5, and the errors σ_{ji} in (4.3) include the statistical uncertainty and a 1.8% systematic uncertainty per each energy bin added in quadrature. Finally, $\sigma_{\rm sys} = 3.7\%$ [102].

The theoretical ratios $R^{\rm the}_{ji}$ are computed using equation (3.20), considering the details of the geometrical configuration of the experimental site [103] and taking cylindrical shapes for the reactor core (3.0 m diameter and 3.5 m height) and the detector (0.9 m diameter and 0.45 m height). For the energy resolution function of the detector, equation (3.21), the standard deviation is $\sigma = 0.12\sqrt{E/(1\,\text{MeV})}$ MeV [104].

The results of the analysis are presented in table 4.3, where the value of the $\chi^2_{\rm min}$ is shown, together with the best fit values of the mixing parameters and the goodness-of-fit.

Note the extremely small value of the goodness-of-fit, which indicates that the fit is very bad for the oscillations hypothesis. Therefore, a combination of the data from SRS and Bugey reactors has not any meaning and would not give useful information about neutrino oscillations.

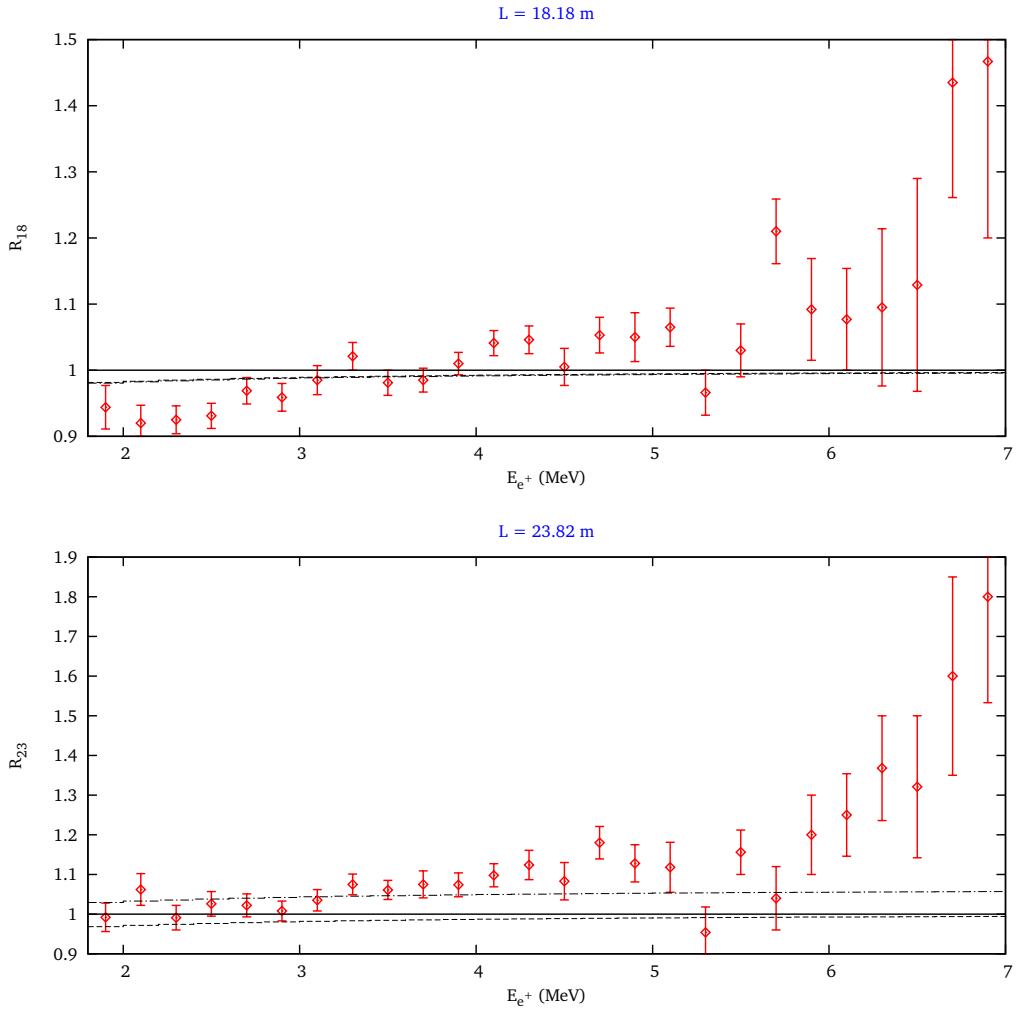

Figure 4.6: Best fit of SRS data. The plot shows the ratio R of observed and expected (in the case of no oscillation) positron spectrum at the two source-detector distances in the SRS experiment as a function of the measured positron kinetic energy E. The dashed and dot-dashed histograms correspond, respectively, to the best-fit values of R_{ji}^{the} and $\alpha_i\, R_{ji}^{\text{the}}$ (with $\alpha_1 = 0.999$, $\alpha_2 = 1.063$) (see equation (4.3)).

Besides, note that the goodness-of-fit for the no oscillation hypothesis is also extremely small. This indicates an incompatibility of the S.R.S. data with the no oscillation hypothesis, for which we do not have any explanation.

These results can also be seen by looking at the plots presented in Figure 4.6, where the histograms relative to the best fit is show compared with the SRS R_{ji}^{exp}. From the histograms one can see that the best fit value for the oscillation parameters does not fit the experimental data. Furthermore, the no oscillations case, represented by the

horizontal line in both histograms, does not show a good fit to the date, either.

4.3 Gösgen

The Gösgen neutrino experiment was performed at the nuclear power reactor in Gösgen, Switzerland. The energy spectra of the electron antineutrinos emerging from the reactor core were measures at distances of $L_1 = 37.9$ m, $L_2 = 45.9$ m and $L_3 = 64.7$ m [105].

The power reactor at Gösgen was a pressurized water reactor with an average thermal power of 2800 MW. The produced total flux was 5×10^{20} $\overline{\nu}_e$/s, with energies up to 8 MeV [105], with the antineutrinos produced from β-decay (essentially from the fission of ^{235}U, ^{239}Pu, ^{238}U and ^{241}Pu). The reactor had a cylindrical core of 3.2 m diameter and 3.4 m height [106].

The neutrino spectrum is obtained by measuring the positron spectrum resulting from the inverse β-decay reaction (3.16), with a neutrino energy given by equation (3.17), related to the kinetic energy of the positron.

The neutrino detector was very similar to the one used at the I.L.L. reactor experiment (section 4.1), figure 4.1, with the additional feature of position sensitivity. The central detector unit was approximately one cubic meter in size and consisted of two systems of counters, which recorded the positron and the neutron generated in the process, respectively [105] (figure 4.1). Thirty cells filled with a liquid scintillator and arranged in five planes were used as target for the antineutrinos and as detector for the produced positrons. The neutrons emerging with energy of several keV's are thermalized in the scintillator cell within a few μs and diffuse into one of the adjacent wire chambers filled with ^{3}He, where they are detected [105].

The target cell energy resolution was 1.8% FWHM at 0.91 MeV as measured with forwardly scattered Compton electrons produced in the scintillator with a ^{65}Zn single-γ-ray source.

The background suppression is basically the same to the one used in the I.L.L. experiment, with the additional advantage that the detector was located outside of the reactor containment building, giving additional 8 meters of concrete shielding.

For our analysis, the data were collected from table IV of [105], where the experimental positron spectra Y_{ji}^{exp} and the predicted positron spectra for no oscillations Y_{ji}^{0} are given ($j = 1, 2, 3$ counts for the source-detector distance, and $i = 1, \cdots, 16$ counts for the energy bin). These data are analyzed with a least-squares method, defining the χ^2-function as

$$\chi^2 = \sum_{j=1}^{3} \sum_{i=1}^{16} \left[\left(\frac{Y_{ji}^{\text{exp}} - N a_j Y_{ji}^{0} R_{ji}^{\text{the}}}{\sigma_{ji}} \right)^2 + \left(\frac{a_j - 1}{\sigma_{a_j}} \right)^2 \right] + \left(\frac{N - 1}{\sigma_N} \right)^2, \qquad (4.5)$$

where the experimental error σ_{ji} are also taken from table IV of [105], the parameters a_{ji} are respective normalizations with uncertainties $\sigma_1 = 0.015$, $\sigma_2 = 0.015$ and $\sigma_3 = 0.030$ [105], and N is a global normalization factor with error $\sigma_N = 6.0\%$, which takes

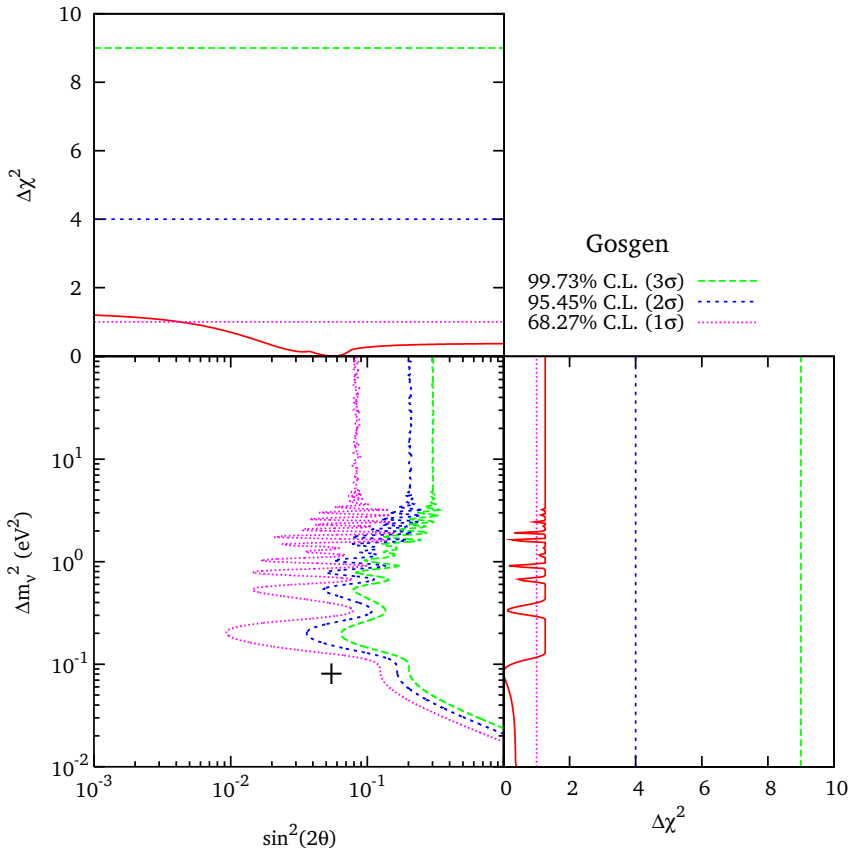

Figure 4.7: Exclusion regions in the oscillation parameter space and marginal $\Delta\chi^2$'s for $\sin^2 2\theta$ and Δm^2 obtained from the analysis of the Gösgen nuclear reactor experiment. The best fit point corresponding to χ^2_{min} is indicated by a cross.

into account uncertainties in normalization common to the three data set (taken at L_1, L_2, L_3) [105]. The R^{the}_{ji} are defined in equation (3.20), with the integrals with respect to the distance computed considering the geometrical configuration and the reactor core and detector sizes used in the experiment. The energy resolution function (3.21) is considered to have standard deviation $\sigma = 0.069\sqrt{E/(0.91\,\text{MeV})}$ MeV.

The χ^2 value at each point of the $(\sin^2 2\theta, \Delta m^2)$ plane is computed by minimizing (4.5) with respect to the four parameters N, a_1, a_2, a_3, and the resulting exclusion regions are shown in figure 4.7. The values of χ^2_{min}, the best fit of the oscillation parameter and the goodness-of-fit, together with the allowed ranges of the oscillation parameters $(\sin^2 2\theta, \Delta m^2)$ are presented in table 4.4.

In spite of the allowed regions present in the $\Delta\chi^2$ marginalized plots (which is an effect due to the statistical analysis, as explained in section 3.1.3), the result of the analysis of the Gösgen experimental data shows only upper limits on the $(\sin^2 2\theta, \Delta m^2)$

Gösgen			Parameter	C.L.	Range
No Osc.	$\chi^2_{\rm min}$	37.96	$\sin^2 2\theta$	$68.27\%(1\sigma)$	> 0.004
	NDF	44		$95.45\%(2\sigma)$	–
	GoF	0.72		$99.73\%(3\sigma)$	–
Osc.	$\chi^2_{\rm min}$	36.70	$\Delta m^2\,[{\rm eV}^2]$	$68.27\%(1\sigma)$	< 2.45
	NDF	42		$95.45\%(2\sigma)$	–
	GoF	0.70		$99.73\%(3\sigma)$	–
	$\sin^2 2\theta_{\rm bf}$	0.055			
	$\Delta m^2_{\rm bf}$ (eV^2)	0.083			

Table 4.4: Results for the fit of the Gösgen nuclear reactor experiment. The first three lines at left correspond to the case of no oscillations (No Osc.). The following five lines correspond to the case of oscillations (Osc.) At right, the marginal allowed regions for the oscillation parameters are given.

plane excluding $\sin^2 2\theta \gtrsim 0.3$ for $\Delta m^2 \gtrsim 0.05$ eV^2 at 3σ. One can also see from table 4.4 that the goodness-of-tit for the no oscillation hypothesis is high (72%), being impossible to exclude it.

To see the result of the analysis in a different way, figure 4.8 shows the histograms relative to the best fit against the Gösgen data at the three source-detector distances. One can see that the best fit lines are very similar to the one corresponding to the no oscillations hypothesis ($R = 1$), which could be considered as an indication of no deviation from this hypothesis.

On the other hand, by comparing figure 4.7 with the results of the Gallium radioactive source experiments, figure 3.9, one can see that there is a marginal compatibility between them. It also happens if one compares the Bugey results with the Gösgen ones, figures 3.14 and 4.7, respectively. The combined fit of the Gösgen nuclear reactor experiment with the Gallium radioactive source experiments and with the Bugey nuclear reactor experiments, as well as the combined fit of the three experiments are shown in figures 4.9, 4.10 and 4.11.

The 2σ and 3σ exclusion regions resulting from the combination of the Gallium and the Gösgen experiments are almost the same to those from the analysis of the Gösgen data alone, but the effect of the Gallium data is reflected in the 1σ contour, which shows some narrow allowed regions for $\sin^2 2\theta \sim 0.1$ and $\Delta m^2 \gtrsim 1$ eV^2, and as can be seen in table 4.5, the fit appears to be acceptable (goodness-of-fit of 64.5%). It is clear that the Gösgen data puts stronger constrains on the hint of neutrino oscillations coming from the Gallium experiments, but it is not completely eliminated, and the best fit of Δm^2 remains much larger than the Solar and Atmospheric neutrino oscillations results. The allowed ranges for the oscillation parameters, extracted from the marginal $\Delta\chi^2$ curves are show in table 4.6.

Concerning the combined fit of Bugey and Gösgen nuclear reactor experiments, the allowed regions are presented in figure 4.10. The curves are just slightly different of

		Ga+Gos	**Bug+Gos**	**Gal+Bug+Gos**
No Osc.	$\chi^2_{\rm min}$	46.27	88.99	97.20
	NDF	48	99	103
	GoF	0.544	0.755	0.643
Osc.	$\chi^2_{\rm min}$	41.90	85.49	91.69
	NDF	46	97	101
	GoF	0.645	0.792	0.735
	$\sin^2 2\theta_{\rm bf}$	0.112	0.044	0.052
	$\Delta m^2_{\rm bf}$ (eV^2)	1.906	1.965	1.965
PG.	$\chi^2_{\rm min}$	2.16	1.32	4.59
	NDF	2	2	4
	GoF	0.340	0.517	0.332

Table 4.5: Results for fit of the different combinations of the Gallium radioactive source experiments and the Bugey and Gösgen reactor experiments. The first three lines correspond to the case of no oscillations (No Osc.). The following five lines correspond to the case of oscillations (Osc.). The last three lines describe the parameter goodness-of-fit (PG) [93].

Parameter	**C.L.**	**Gal+Gos**	**Bug+Gos**	**Gal+Bug+Gos**
$\sin^2 2\theta$	$68.27\%(1\sigma)$	$0.060 - 0.168$	$0.020 - 0.066$	$0.031 - 0.074$
	$95.45\%(2\sigma)$	> 0.004	–	$0.007 - 0.123$
	$99.73\%(3\sigma)$	–	–	–
Δm^2 [eV^2]	$68.27\%(1\sigma)$	$1.56 - 2.49$	$1.89 - 1.98$	$1.89 - 1.98$
	$95.45\%(2\sigma)$	–	–	$0.82 - 4.49$
	$99.73\%(3\sigma)$	–	–	–

Table 4.6: Allowed ranges of $\sin^2 2\theta$ and Δm^2 from combined fit of the Gallium radioactive source experiments with the Gösgen nuclear reactor experiment, from the combined fit of the Bugey and Gösgen reactor experiments, and from the combined fit of the Gallium, Bugey and Gösgen experiments. The dash indicates the absence of limits.

those resulting from the Bugey analysis alone, and the net effect of the Gösgen data is that of weakening the hint of neutrino oscillations, by eliminating the 1σ allowed region present in the which appears from Bugey, figure 3.14, and stretching the other two towards small values of $\sin^2 2\theta$; however, the best fit values for the oscillation parameters remain unchanged. Note that, form table 4.5, the combined fit is good (GoF 79%), although the no oscillation hypothesis is not excluded. In addition, the parameter goodness-of-fit is also high, showing a good compatibility between the experiments.

By combining the three experimental data, the resulting allowed regions are those

		Reactors	**Gal+Reac**
No Osc.	$\chi^2_{\rm min}$	89.07	97.28
	NDF	100	104
	GoF	0.775	0.666
Osc.	$\chi^2_{\rm min}$	86.07	92.46
	NDF	98	102
	GoF	0.800	0.740
	$\sin^2 2\theta_{\rm bf}$	0.039	0.047
	$\Delta m^2_{\rm bf}$ (eV^2)	1.965	1.965
PG.	$\chi^2_{\rm min}$	1.28	4.73
	NDF	3	5
	GoF	0.733	0.450

Table 4.7: Results for fit of the combinations of the Gallium radioactive source experiments and the nuclear reactor experiments. The first three lines correspond to the case of no oscillations (No Osc.). The following five lines correspond to the case of oscillations (Osc.). The last three lines describe the parameter goodness-of-fit (PG) [93].

shown in figure 4.11. The values value of the $\chi^2_{\rm min}$ and the best fit of the oscillation parameters can be read from table 4.5, together with the goodness-of-fit and the parameter goodness-of-fit. The inclusion of the Gallium data to the combined fit of the two reactor data has the effect of cancelling the 1σ allowed region at $\Delta m^2 \sim 0.9$ eV^2 and disfavoring at 1σ values of $\sin^2 2\theta$ smaller than about 2×10^{-2}. This is a similar result to the one obtained from the combined fit of the Gallium radioactive experiments with the Bugey reactor experiment, shown in figure 3.16, so one can also say that the effect of the inclusion of the Gösgen data to the Gallium-Bugey combined fit is that of eliminating the 1σ allowed region at $\Delta m^2 \sim 3$ eV^2 and moving slightly the one at $\Delta m^2 \sim 1.9$ eV^2 towards smaller values of $\sin^2 2\theta$.

The best fit remains still unchanged, and the parameter goodness-of-fit (33%) does not allow to exclude the compatibility of the three data set. The goodness-of-fit for both, the oscillations and non oscillations cases, allow us to say that combinations are compatible with both cases, with a hint in favor of neutrino oscillations with $0.03 \lesssim \sin^2 2\theta \lesssim 0.07$ and $\Delta m^2 \approx 1.9$ eV^2.

Finally, we added the Chooz experimental data to the previous analyses. In the what follows, we call *Reactors* to the combined analysis of the data from the Bugey, Chooz and Gösgen nuclear reactor experiments, and *Gallium + Reactors* to the combined analysis in which the Gallium radioactive source experiment is added to the *Reactors*.

The results of these analyses are presented in the plots shown in figure 4.12 and 4.13, in which the allowed regions from the fit of the *Reactors* and form the combined analysis *Gallium + Reactors* are shown, respectively. The values of the $\chi^2_{\rm min}$, the goodness-

Parameter	C.L.	Reactors	Gal+Reac
$\sin^2 2\theta$	$68.27\%(1\sigma)$	$0.016 - 0.061$	$0.026 - 0.069$
	$95.45\%(2\sigma)$	–	$0.004 - 0.095$
	$99.73\%(3\sigma)$	–	–
Δm^2 [eV^2]	$68.27\%(1\sigma)$	$0.87 - 1.97$	$1.89 - 1.97$
	$95.45\%(2\sigma)$	–	$0.82 - 4.49$
	$99.73\%(3\sigma)$	–	–

Table 4.8: Allowed ranges of $\sin^2 2\theta$ and Δm^2 from combined fit of the Gallium radioactive source experiments with the nuclear reactor experiments, and from the combined fit of the nuclear reactor experiments. The dash indicates the absence of limits.

of-fit and the best fit values of the oscillation parameters are given in table 4.7, and the allowed ranges for the oscillation parameters, as extracted form the marginal $\Delta\chi^2$ plots are given in table 4.8.

One can note that the result of the combined fit of the Bugey, Chooz and Gösgen nuclear reactor experiments is just slightly different to that of the combination of Bugey and Chooz, figure 3.21. The inclusion of the Gösgen data makes the 1σ allowed regions to be smaller and the one for $\Delta m^2 \approx 3$ eV^2 disappears, but the best fit values of the oscillation parameters are practically unchanged (see table 4.7), and the hint in favor of neutrino oscillations persists.

Table 4.7 shows also the values of the goodness-of-fit for the oscillations and no oscillations hypothesis. Both of the cases present a good fit, so that the combined analysis is compatible with them. The important point here is that the parameter goodness-of-fit is also high (73%), suggesting that the data of the three reactor experiments are compatible.

Finally, the inclusion of the Gallium data gives as a result the allowed regions shown in figure 4.13. The values of the χ^2_{min}, the goodness-of-fit and of the best fit of the mixing parameters are given in table 4.7.

The first thing to see is that the inclusion of the Gallium data reduces considerably the 1σ allowed region for $\Delta m^2 \approx 0.9$ eV^2 and disfavors at 1σ values of $\sin^2 2\theta$ smaller than about 0.02 (very similar to the effect of the combination of the Bugey and Gallium experiments, section 3.2.1).

In conclusion, and taking into account the information written in tables 4.7 and 4.8, we can say that both of the combined analyses are compatible with the no oscillation hypothesis and with the hypothesis of neutrino oscillations. The hint of oscillations is weak, because of the narrowness of the 1σ allowed regions, but it remains and is consistent with the different analysis.

On the other hand, the parameter goodness-of-fit for the two analyses allows to say that the Bugey, Chooz, Gösgen, and Gallium experimental data are compatible and the hint of neutrino oscillations is present with

$$0.03 \lesssim \sin^2 2\theta \lesssim 0.07, \qquad \Delta m^2 \approx 1.93 \text{ eV}^2. \tag{4.6}$$

4.4 Summary

We analyzed the data of the ILL nuclear reactor experiment in terms of $\overline{\nu}_e$ disappearance due to effective two–neutrino oscillations. We found that the combination of these data with the Bugey data show a very low compatibility. In fact, the 1σ allowed regions obtained from the ILL data are almost completely inside the exclusion region given by the Bugey analysis, showing tension between them. Therefore, we do not consider these experimental data for additional analyses.

From the analysis of the SRS reactor experiment, we found that the data are incompatible with neutrino oscillations, as well as with no oscillations. We do not have any explanation for the behavior of the data.

The analysis of the Gösgen nuclear reactor experimental data gives only upper limits for the mixing parameters, excluding the region with $\sin^2 2\theta \geq 0.3$ and $\Delta m^2 \geq 0.05$ eV^2 at 3σ.

When combined with the Gallium data, we found a 1σ allowed region in the $(\sin^2 2\theta, \Delta m^2)$ plane, mainly coming from the Gallium data, around $\sin^2 2\theta \sim 0.1$ with $\Delta m^2 \gtrsim 1$ eV^2, with a parameter goodness-of-fit indicating a good compatibility of the data, and giving a hint in favor of neutrino oscillations compatible with the results presented in chapter 3.

The combination of the Gösgen data with the Bugey data gives similar results to those we got from Bugey data alone (chapter 3). The effect of the Gösgen data is that of weakening the hint in favor of neutrino oscillations, without changing the best fit values of the oscillation parameters. In this case, the parameter goodness-of-fit also indicates an acceptable compatibility of the data.

Then, the combined fit of Gallium, Bugey and Gösgen experiments has similar results to those of the Gallium+Bugey analysis. The best fit remains the same, with $\Delta m^2 \sim 1.9$ eV^2. We found a rather good compatibility of the data sets, and the results are consistent with the others presented here. Although the no oscillation hypothesis cannot be excluded, we found a hint in favor of neutrino oscillations with $0.03 \lesssim \sin^2 2\theta \lesssim 0.07$ and $\Delta m^2 \approx 1.9$ eV^2.

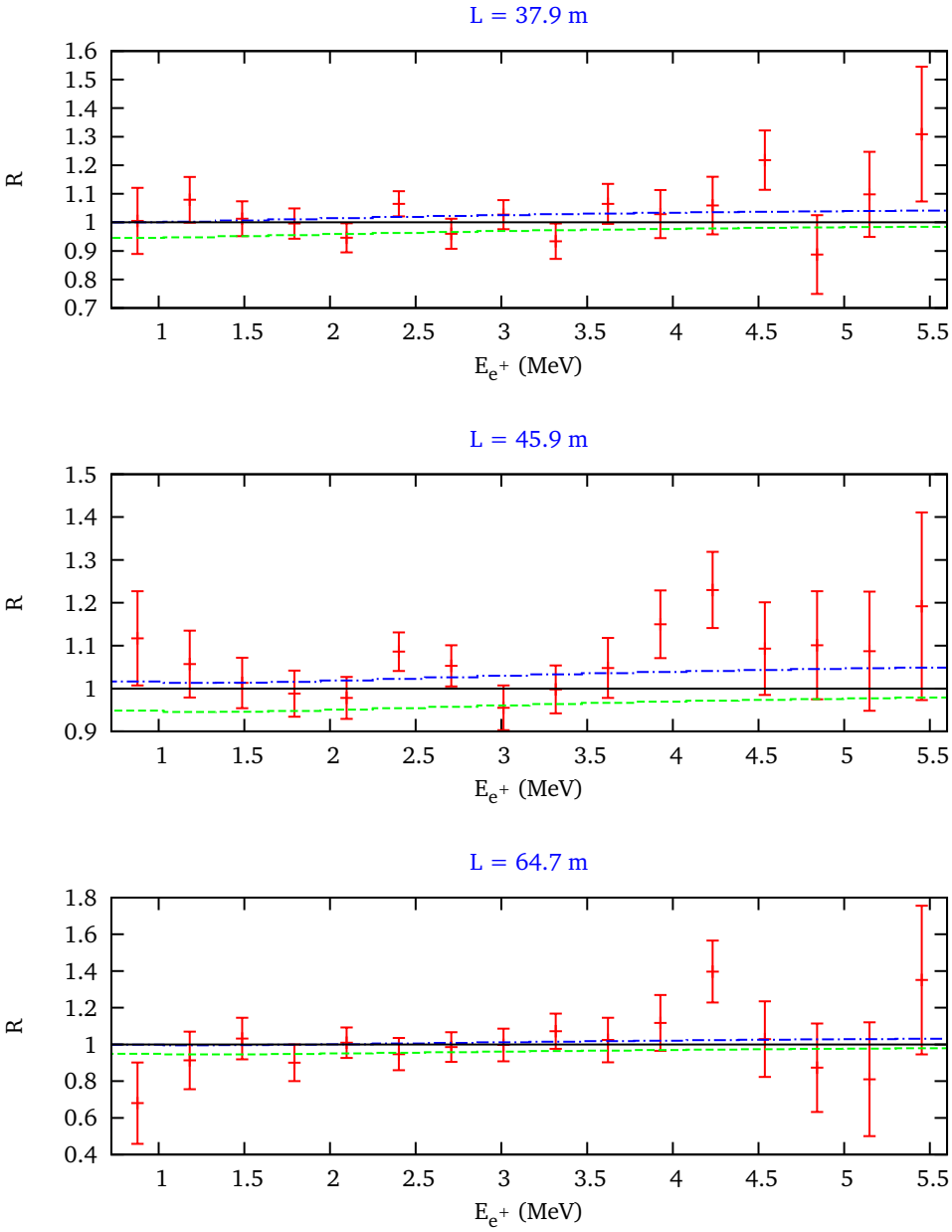

Figure 4.8: Best fit of Gösgen data. The three panels show the ratio R of observed (Y_{ji}^{exp}) and expected (in the case of no oscillation Y_{ji}^{0}) positron spectra at the three source-detector distances in the Gösgen experiment as functions of the measured positron kinetic energy E. In each panel, the dot-dashed and dashed histograms correspond, respectively, to the best-fit values of $(Na_j)\, R_{ji}^{\text{the}}$ and $Y_{ji}^{\text{exp}}/Y_{ji}^{0}$, with $a_1 = 0.996$, $a_2 = 1.010$, $a_3 = 0.992$, $N = 1.062$ (see equation (4.5)).

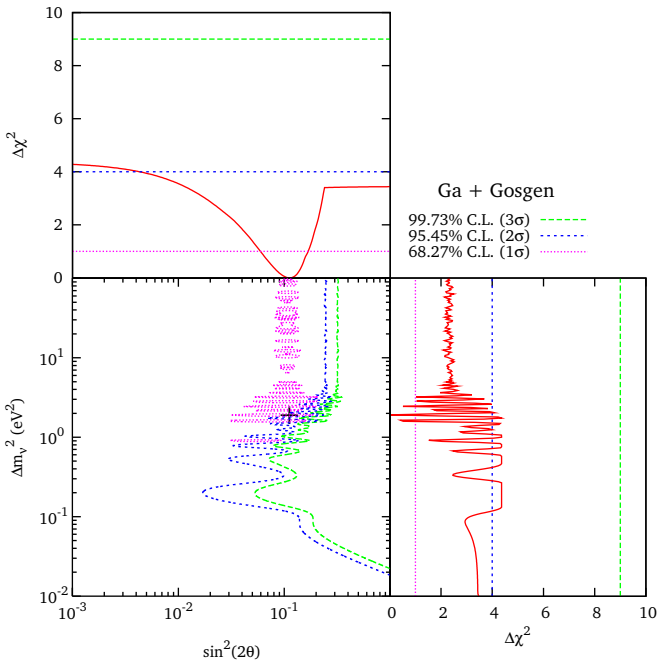

Figure 4.9: Allowed regions in the oscillation parameter space and marginal $\Delta\chi^2$s for $\sin^2 2\theta$ and Δm^2 obtained from the combined fit of the Gallium radioactive source experiments and the Gösgen nuclear reactor experiment. The best fit point corresponding to $\chi^2_{\rm min}$ is indicated by a cross.

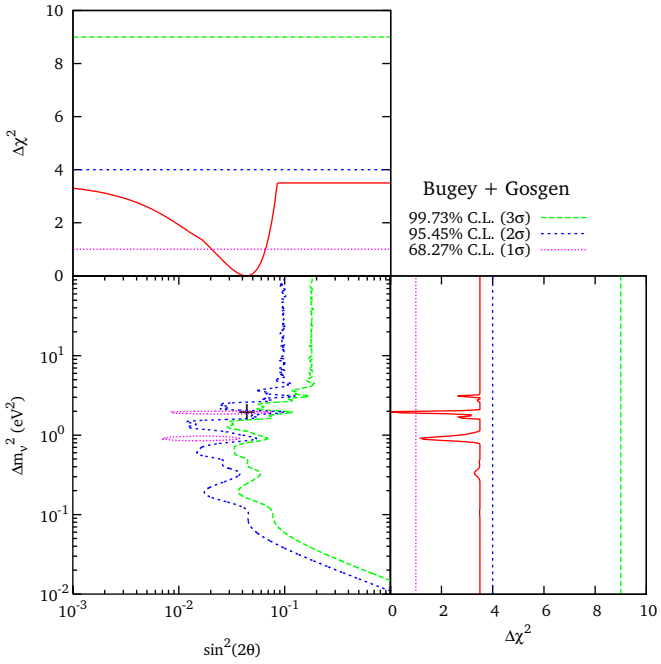

Figure 4.10: Allowed regions in the oscillation parameter space and marginal $\Delta\chi^2$s for $\sin^2 2\theta$ and Δm^2 obtained from the combined fit of the Bugey and Gösgen nuclear reactor experiments. The best fit point corresponding to χ^2_{min} is indicated by a cross.

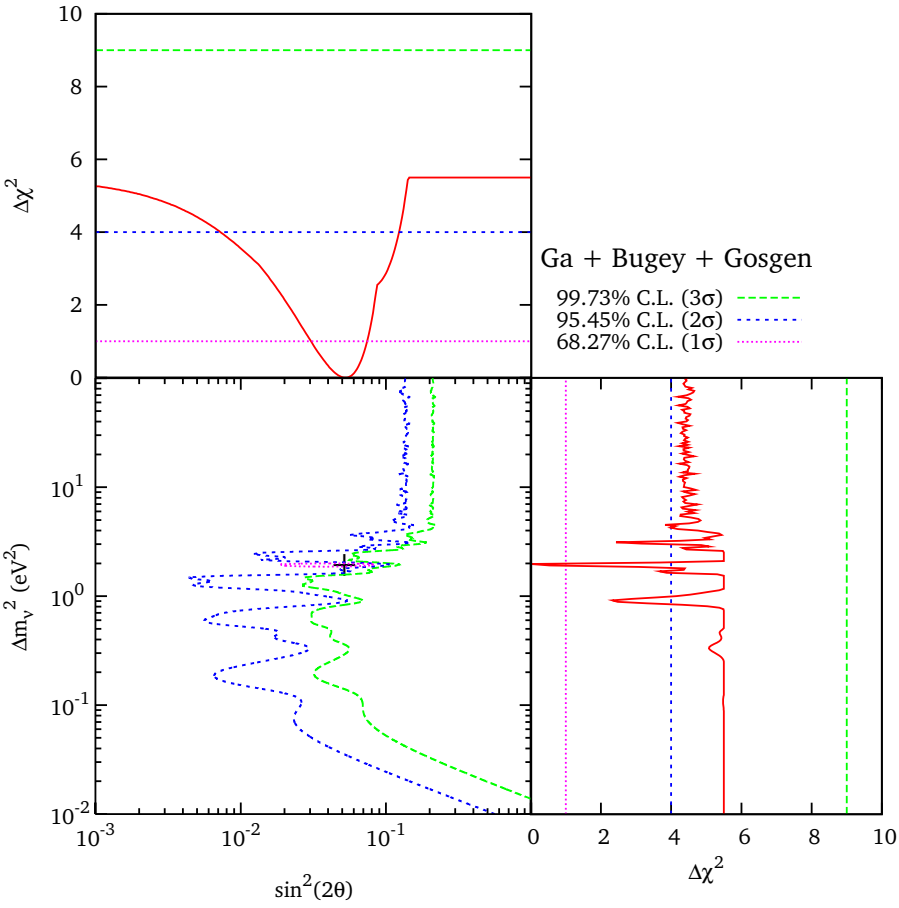

Figure 4.11: Allowed regions in the oscillation parameter space and marginal $\Delta\chi^2$'s for $\sin^2 2\theta$ and Δm^2 obtained from the combined fit of the Gallium radioactive source experiments and the Bugey and Gösgen nuclear reactor experiments. The best fit point corresponding to $\chi^2_{\rm min}$ is indicated by a cross.

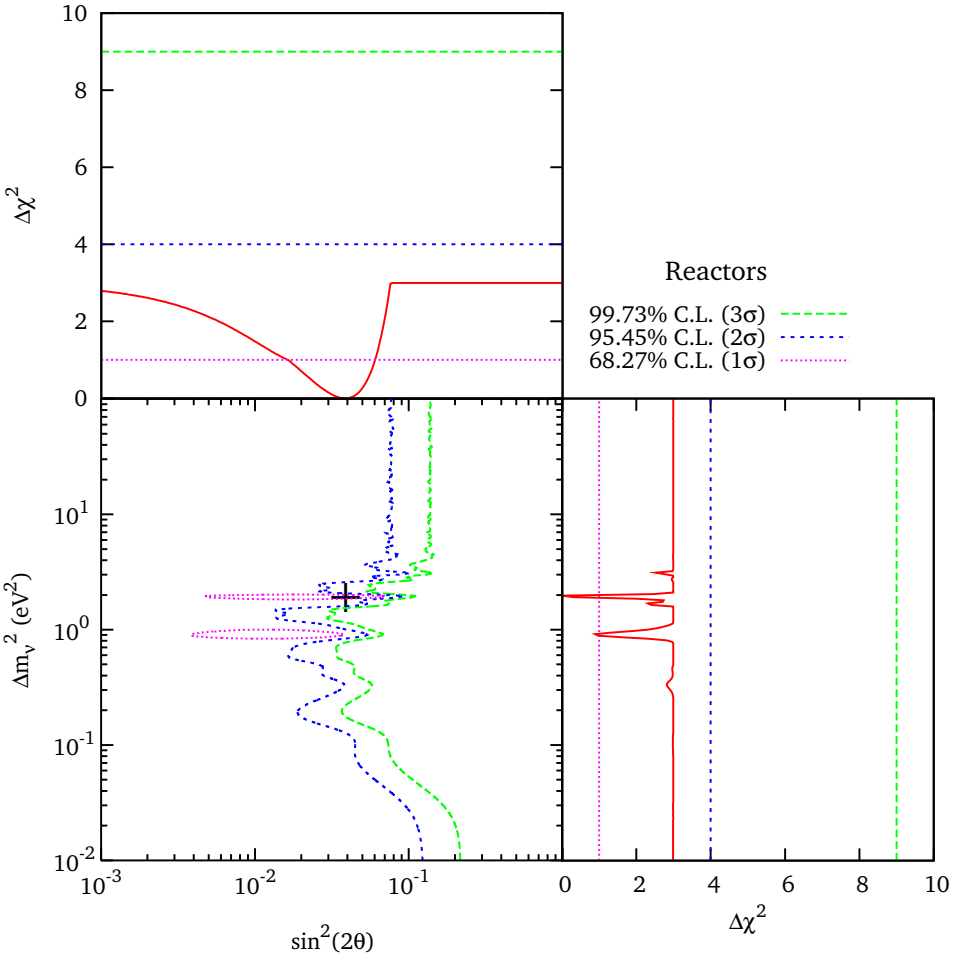

Figure 4.12: Allowed regions in the oscillation parameter space and marginal $\Delta\chi^2$s for $\sin^2 2\theta$ and Δm^2 obtained from the combined fit of all the nuclear reactor experiments. The best fit point corresponding to χ^2_{min} is indicated by a cross.

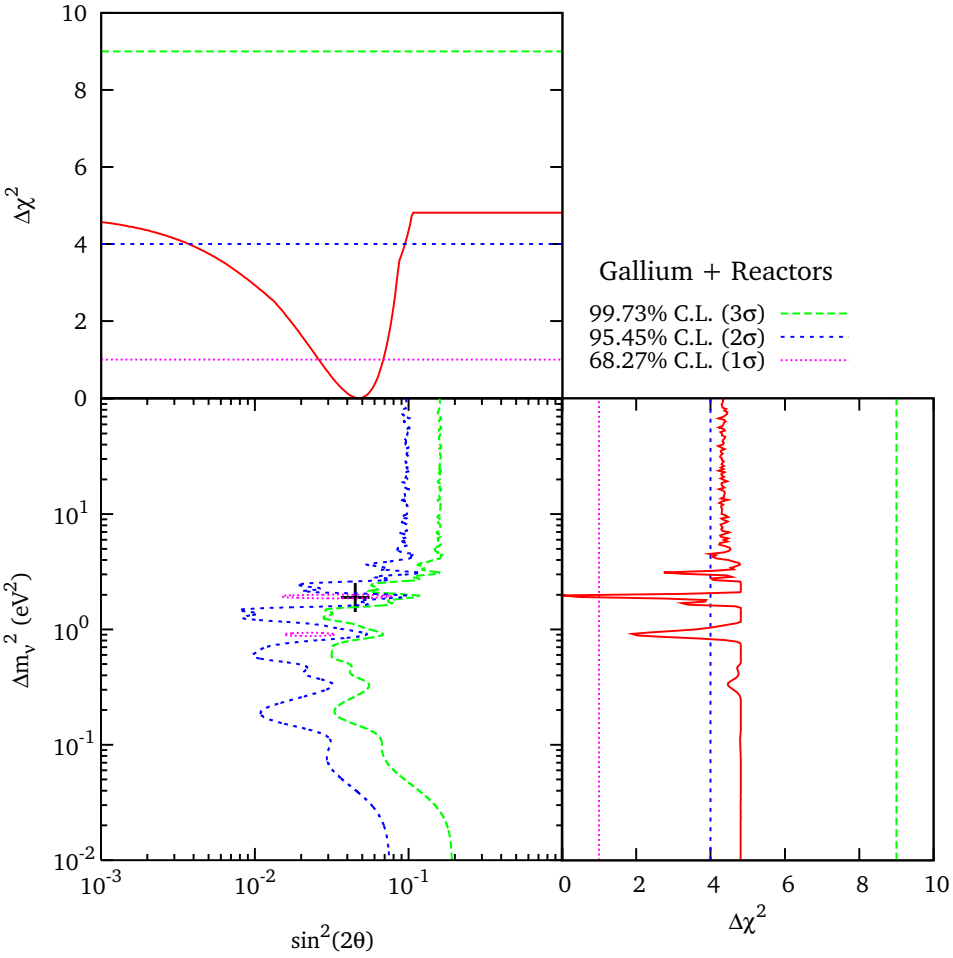

Figure 4.13: Allowed regions in the oscillation parameter space and marginal $\Delta\chi^2$s for $\sin^2 2\theta$ and Δm^2 obtained from the combined fit of the Gallium radioactive source experiments and all the nuclear reactor experiments. The best fit point corresponding to $\chi^2_{\rm min}$ is indicated by a cross.

CHAPTER 5

NEUTRINOS IN COSMOLOGY

Is clear that active interaction between different scientific areas is very important and produce fruitful results. A remarkable example of this, is the fascinating complementarity between Particle Physics and Astrophysics (and Cosmology), currently denominated *Astroparticle Physics*[1], inside which, neutrino physics plays a relevant role and is a very active topic of research.

In addition, neutrinos are the second most abundant particles in the Universe, so that they have profound impact on different aspects of cosmology, from the question of leptogenesis in the very early Universe, over big bang nucleosynthesis, to late time structure formation [108, 109].

This chapter is devoted to Neutrino Cosmology, presenting a brief introduction to the basics of Cosmology, followed by a brief thermal history of the Universe, enphazising on the neutrino decoupling time and temperature; also some constrains on neutrino properties which come from cosmological experimental data are presented. Finally, we present the study of the compatibility of cosmological experimental data with the hypothesis of light non-thermal sterile neutrinos (in the spirit of the result of the previous chapter) and with a small contribution to the effective number of neutrino species.

5.1 introduction

Although the way in which the Universe was originated is still unknown, we do know it is evolving in such a way that its temperature is decreasing and that it is experimenting an expansion process. During this evolution, the Universe has passed by different epochs characterized by a decreasing temperature as the time grows.

[1] As defined in reference [107], Astroparticle physics is an interdisciplinary field lying between particle physics and cosmology that attempts to reveal the nature and structure of matter in the universe.

At around $t \approx 10^{-37}$ s ($T \sim 10^{28}$ K) after the Big Bang, an epoch known as *inflation* dominated the evolution of the Universe; here the expansion was rapidly accelerated and, presumably, all the existing particles were mixed in a dense and hot (primordial) plasma in thermal equilibrium.

Following the inflation epoch, the temperature decreases until a value in which particles (quarks, gluons) started to decouple from the primordial plasma and to combine to form mesons and baryons (neutrons and protons).

Latter on, at a temperature of a few MeV's ($\sim 10^{10}$ K), electromagnetic interactions became much more effective than weak interactions, so that neutrinos and antineutrinos decoupled from the main plasma and the so-called *Cosmic Neutrino Background (CNB)* started it journey, contributing to the evolution of the Universe in the form of radiation. Just after this ($t \sim 1$ s), *Primordial Nucleosynthesis* started to take place, creating the light elements (D, He, Li).

One of the most important events for observational cosmology took place in the next stage, at $T \sim 3000$ K, when photons decoupled form the plasma (mainly composed by photons, electrons and positrons, at this stage) and the *Cosmic Microwave Background Radiation, CMBR* was created. At this point, the CNB started to contribute also to the matter component of the Universe, and its presence played an important role in the subsequent processes of the evolution of the Universe, as in the fromation of Large Scale Structures (LSS).

5.2 Basics on Cosmology

To understand the evolution of the Universe, it is necessary to study the fundamentals of the Standard Model of Cosmology (SMC).

In the SMC, the Universe is assumed to be *homogeneous* and *isotropic* (cosmological Principle), and its dynamical evolution is described by the Einstein equations

$$R^{\mu\nu} - \frac{1}{2} g^{\mu\nu} \mathcal{R} = 8\pi G_N T^{\mu\nu} + \Lambda g^{\mu\nu}, \tag{5.1}$$

where $g^{\mu\nu}$ is the metric tensor which describes the geometry of the space-time[2], and $T^{\mu\nu}$ is the energy-momentum tensor describing the contents of the Universe. In equation (5.1), Λ is the cosmological constant and G_N is the Newton constant of gravitation.

Under the considerations of the cosmological principle, the Standard Cosmological Model describes the Universe by a perfect fluid with an energy momentum tensor given by

$$T^{\mu\nu} = (\rho + p) u^\mu u^\nu - p g^{\mu\nu}, \tag{5.2}$$

where ρ and p are the energy and pressure densities, respectively, and $u^\mu = \mathrm{d}x^\mu / \mathrm{d}\tau$ is

[2]In an empty and flat space-time, the metric tensor reduces to the Minkowski limit, $\eta^{\mu\nu} = \mathrm{diag}(1, -1, -1, -1)$, which is the metric tensor of special relativity.

the four-velocity[3] of the fluid. In the rest frame of the fluid, $u^\mu = (1, 0, 0, 0)$, so

$$\begin{aligned} T^{00} &= \rho, \\ T^{ij} &= p\,\delta^j_i \quad (i, j = 1, 2, 3). \end{aligned} \tag{5.3}$$

The cosmological constant Λ in equation (5.1), can be interpreted as the energy density of the vacuum (*dark energy*), defined as the state with the lowest attainable energy. Then, the contribution of the cosmological constant to the Einstein equation can be written as a contribution to the energy-momentum tensor in the right-hand side, as

$$T^{\mu\nu}_\Lambda = \frac{\Lambda}{8\pi G_N} g^{\mu\nu}, \tag{5.4}$$

which can be considered as a perfect fluid with constant energy density

$$\rho_\Lambda = \frac{\Lambda}{8\pi G_N}, \tag{5.5}$$

and constant negative pressure

$$p_\Lambda = -\rho_\Lambda. \tag{5.6}$$

In this way, the total energy-momentum tensor can be expressed as the sum of the different components of the Universe,

$$T^{\mu\nu} = T^{\mu\nu}_{\text{matter}} + T^{\mu\nu}_{\text{radiation}} + T^{\mu\nu}_\Lambda, \tag{5.7}$$

so that Einstein equations (5.1) can be written as

$$R^{\mu\nu} - \frac{1}{2} g^{\mu\nu}\mathcal{R} = 8\pi G_N T^{\mu\nu}, \tag{5.8}$$

Each of the components which contributes to the energy-momentum tensor, is characterized by an *equation of state* of the form

$$p_i = w_i \rho_i, \qquad (i = \text{mat,rad,}\Lambda), \tag{5.9}$$

with

$$w_{\text{mat}} = 0, \tag{5.10}$$

$$w_{\text{rad}} = 1/3, \tag{5.11}$$

$$w_\Lambda = -1, \tag{5.12}$$

which have direct effect on the corresponding energy densities evolution.

The other important part in the Einstein equation (5.1), necessary to describe the evolution of the Universe, is the metric tensor $g^{\mu\nu}$. In the SMC, the geometry of the space-time is described by the Robertson-Walker metric

$$\mathrm{d}s^2 = \mathrm{d}t^2 - a^2(t)\left(\frac{\mathrm{d}r^2}{1-kr} + r^2\mathrm{d}\theta^2 + r^2\sin^2\theta\mathrm{d}\phi^2\right), \tag{5.13}$$

[3] $\mathrm{d}\tau$ is the infinitesimal proper-time interval given by $\mathrm{d}\tau^2 = g_{\alpha\beta}\mathrm{d}x^\alpha\mathrm{d}x^\beta$, with $g^{\alpha\rho}g_{\rho\beta} = \delta^\alpha_\beta$.

where $a(t)$ is the scale factor describing the dynamics of the expanding Universe, and the parameter k describes the spacial curvature, with

$$k = \begin{cases} -1 & \text{open Universe,} \\ 0 & \text{flat Universe,} \\ +1 & \text{closed Universe.} \end{cases} \tag{5.14}$$

The physical length is given by $x = a(t)r$, with r the comoving coordinate, in which the distance between two particles remains constant unless a force acts on them. When the scale factor grows, $\dot{x} = \left(\frac{\dot{a}}{a}\right) x$, and one can define the expansion rate of the Universe (*Hubble parameter*) as

$$H(t) = \frac{\dot{a}(t)}{a(t)}, \tag{5.15}$$

which appears in the Friedmann equation (00 component of the Einstein equations (5.1)), with the energy-momentum tensor (5.3) and the Robertson-Walker metric (5.13),

$$(H(t))^2 = \left(\frac{\dot{a}}{a}\right)^2 = \frac{8\pi G_N}{3}\rho - \frac{k}{a^2}. \tag{5.16}$$

From the (ii) component of the Einstein equations (5.1) one also finds the acceleration equation

$$\frac{\ddot{a}}{a} = -\frac{4\pi G_N}{3}(\rho + 3p). \tag{5.17}$$

Note that from the Friedmann equation (5.16), one has the time derivative of the energy density given by

$$\dot{\rho} = \frac{3}{4\pi G_N}\left(\frac{\dot{a}}{a}\right)\left\{\frac{\ddot{a}}{a} - \left[\left(\frac{\dot{a}}{a}\right)^2 + \frac{k}{a^2}\right]\right\}, \tag{5.18}$$

which, using equations (5.16) and (5.17), allows to get the law of energy conservation

$$\dot{\rho} = -3H(\rho + p), \tag{5.19}$$

where the the definition of the expansion (Hubble) parameter (5.15) was used.

From the Friedmann equation (5.16) it is also possible to define the *critical density* ρ_c, as that for which $k = 0$ (meaning a spatially flat Universe):

$$\rho_c \equiv \frac{3H^2}{8\pi G_N}, \tag{5.20}$$

used to define the dimensionless density

$$\Omega \equiv \frac{\rho}{\rho_c}. \tag{5.21}$$

Parameter	Mean value
$\Omega^0_{\rm mat}\, h^2$	$0.1358^{+0.0037}_{-0.0036}$
$\Omega^0_{\rm bar}\, h^2$	$0.02267^{+0.00058}_{-0.00059}$
$\Omega^0_{\rm cdm}\, h^2$	0.1131 ± 0.0034
$\Omega^0_{\rm rad}$	4.6×10^{-5} [32]
Ω^0_Λ	0.726 ± 0.015

Table 5.1: Mean values of the energy densities of the different components of the Universe: *mat* is for matter, *bar* for the baryonic content, *cdm* for the cold dark matter, *rad* for radiation and Λ for the vacuum energy. The values are taken from Table I of [32], except for $\Omega^0_{\rm rad}$.

The value of the present critical density is [63]

$$\begin{aligned} \rho_c^0 &= (1.87835 \pm 0.00019) \times 10^{-29}\, h^2 \ \text{g cm}^{-3} \\ &= (1.05368 \pm 0.00011) \times 10^{-5}\, h^2\, (\text{GeV}/c^2), \end{aligned} \tag{5.22}$$

where $h = 0.73 \pm 0.03$ [63] is the normalized Hubble parameter.

Dividing each term of equation (5.16) by ρ_c and considering the dimensionless density (5.21), the Friedmann equation can be rewritten as

$$\Omega - 1 = \frac{k}{H^2 a^2} = \frac{k}{\dot{a}^2}, \tag{5.23}$$

from which one can see that Ω is constant only if it is equal to unity ($\rho = \rho_c$) and the Universe is flat, $k = 0$; if $\Omega > 1$, $k = 1$ and Ω increases when the expansion velocity $\dot{a}$ decreases; if $\Omega < 1$, $k = -1$ and Ω decreases with the expansion velocity $\dot{a}$.

In the cosmological model, it is useful to make the distinction among the different constituents of the Universe which contribute to the density Ω,

$$\Omega_i = \frac{\rho_i}{\rho_c}, \qquad i = \text{mat, rad, } \Lambda, \tag{5.24}$$

such that the total dimensionless energy density of the Universe is

$$\Omega_{\rm T} = \sum_i \Omega_i. \tag{5.25}$$

The present values of the corresponding (matter, radiation and vacuum) contributions, is denoted by Ω_i^0 (see table 5.2). Each component has a different equation of state relating ρ and p, and its evolution in time is also different, and can be derived from equation (5.19) together with the general equation of state (5.9):

$$\dot{\rho}_i = -3H(1 + w_i)\rho_i, \tag{5.26}$$

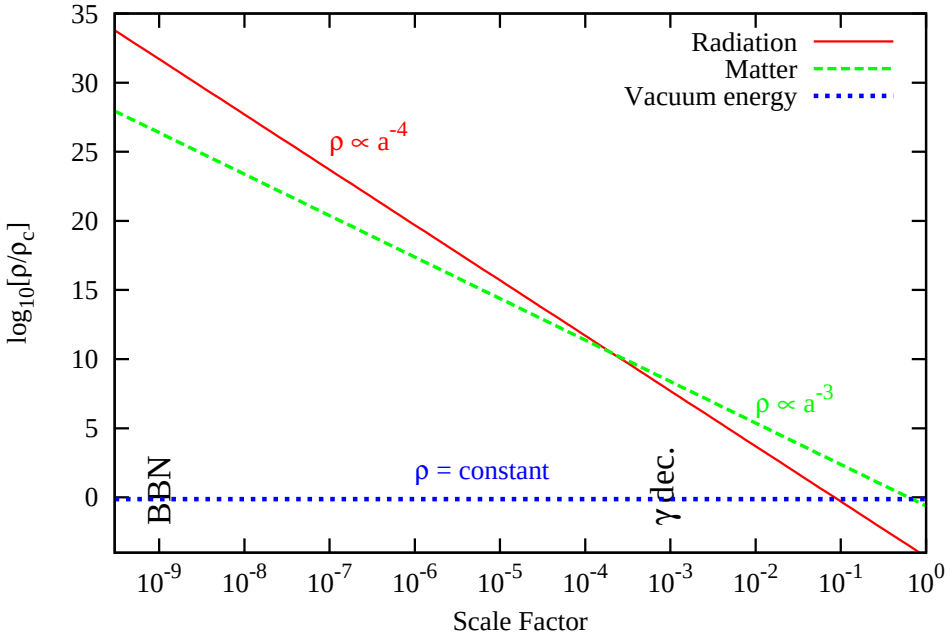

Figure 5.1: Energy density vs. scale factor for different constituents of a flat Universe. The plots are in units of the critical density today.

which can be written as

$$\frac{\dot{\rho}_i}{\rho_i} = -3(1+w_i)\frac{\dot{a}}{a}$$
$$\frac{\mathrm{d}(\ln \rho_i)}{\mathrm{d}t} = -3(1+w_i)\frac{\mathrm{d}(\ln a)}{\mathrm{d}t}, \tag{5.27}$$

giving the evolution in time for each of the density components of the Universe, in terms of the scale factor:

$$\rho_i \propto a^{-3(1+w_i)}, \qquad i = \text{mat, rad, } \Lambda. \tag{5.28}$$

Therefore, on has

$$\begin{array}{lll} w_{\text{mat}} = 0 & \text{so} & \rho_{\text{mat}} \propto a^{-3} \\ w_{\text{rad}} = 1/3 & \text{so} & \rho_{\text{rad}} \propto a^{-4} \\ w_\Lambda = -1 & \text{so} & \rho_\Lambda = \text{constant}. \end{array} \tag{5.29}$$

Figure 5.1 shows the evolution of the energy density for each component, in terms of the scale factor a, considering the results in equation (5.29). From the figure, one can notice that today ($a = 1$) the Universe is dominated by vacuum energy (cosmological constant) and matter, but at early times, radiation was the dominant component. The intersection point of the matter and radiation evolution lines marks the epoch at which matter and radiation are equal (a_{eq}).

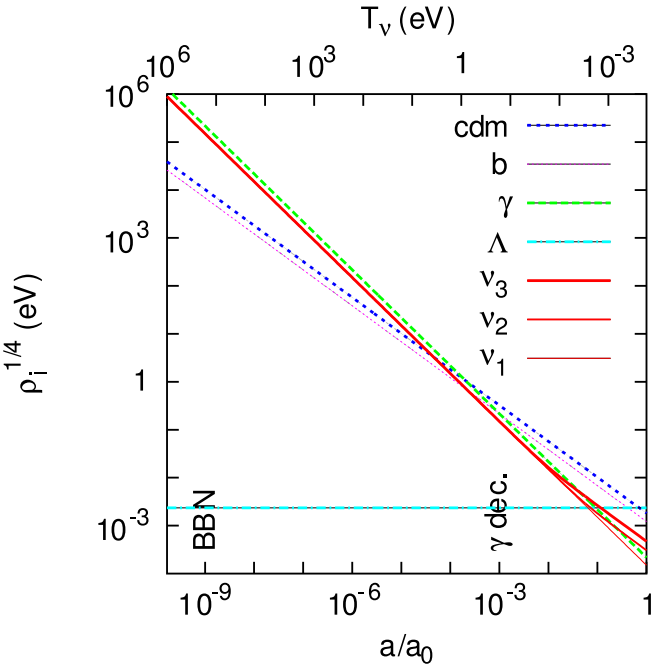

Figure 5.2: Evolution of the background densities from the time when $t_\nu = 1$ MeV until now, for each component of a flat Universe (cold dark matter -cdm-, baryons -b-, radiation -γ-, vacuum energy -Λ- and neutrinos -ν_i-). The three neutrino masses are distributed according to the normal hierarchy scheme, with $m_1 = 0$, $m_2 = 0.009$ eV and $m_3 = 0.05$ eV. The neutrino energy is shown on the top axis [19].

A detailed analysis of the evolution of the densities, including small neutrino masses, shows a slight modification of the result in figure 5.1. Depending on their masses, neutrinos evolve in such a way that they contribute to the radiation energy density till the moment when $T \ll m_{\nu_i}$, and from this point, massive neutrinos contribute to the matter density. This is shown in figure 5.2, from [19]. One can see that the non relativistic transition of each neutrino species amounts in converting a fraction of radiation into matter [19], occurring first to the most massive one.

5.3 Brief history of the Universe

As mentined before, while the Universe expands, the temperature decrease, and one can also describe the evolution of the components of the Universe in terms of its temperature in an analogous way as it is show in figure 5.1, such that the corresponding temperature today, for $a = 1$ is $T_0 \approx 2.4 \times 10^{-4}$ eV.

At large temperature (small scale factor), the matter and radiation energy densities were very large, and the Universe was in thermal equilibrium due to rapid interactions

of the particles through processes of the form

$$\chi + A \rightarrow \chi + A \tag{5.30}$$

$$\chi + \overline{\chi} \leftrightarrow A + \overline{A}. \tag{5.31}$$

These processes are effective, keeping the thermal equilibrium, until the temperature decreases at values at which the interaction rate $\Gamma_{\rm int}$ (for each particle species) becomes smaller than the expansion rate; in other words, an individual species remain in equilibrium as long as $\Gamma_{\rm int} \gtrsim H = \dot{a}/a$, and it *freezes out* (becomes a relic species) when $\Gamma_{\rm int} < H$. From this moment, the particles travel is not any more coupled to the *primordial plasma* formed by all the species in the early Universe.

Each particle species χ forms a weakly-interacting gas with number density n, energy density ρ and pressure density given by

$$n = \frac{g}{(2\pi)^3} \int f(\overrightarrow{p}) \mathrm{d}^3 p, \tag{5.32}$$

$$\rho = \frac{g}{(2\pi)^3} \int E(\overrightarrow{p}) f(\overrightarrow{p}) \mathrm{d}^3 p, \tag{5.33}$$

$$p = \frac{g}{(2\pi)^3} \int \frac{|\overrightarrow{p}|^2}{3E(\overrightarrow{p})} f(\overrightarrow{p}) \mathrm{d}^3 p, \tag{5.34}$$

where g is the number of degrees of freedom and $E(\overrightarrow{p}) = \sqrt{|\overrightarrow{p}|^2 + m^2}$ is the energy. For particles in kinetic equilibrium, the phase space distribution function f is given by the Fermi-Dirac (+) or Bose-Einstein (-) distributions

$$f(\overrightarrow{p}) = \left[\exp\left(\frac{E - \mu}{T} \right) \pm 1 \right]^{-1}, \tag{5.35}$$

where μ is the chemical potential.

The computation of the quantities in equations (5.32) can be done in two different cases:

- Non-relativistic regime, $m \gg T$ (and $m \gg \mu$).
  In this case, for bosons and fermions,

$$f(\overrightarrow{p}) \simeq \exp\left(\frac{\mu - m}{T} \right) \exp\left(-\frac{|\overrightarrow{p}|^2}{2mT} \right), \tag{5.36}$$

  so that

$$n = g \left(\frac{mT}{2\pi} \right)^{3/2} \exp\left(\frac{\mu - m}{T} \right), \tag{5.37}$$

$$\rho = mn \left(1 + \frac{3}{2} \frac{T}{m} \right), \tag{5.38}$$

$$p = nT \ll \rho. \tag{5.39}$$

- Relativistic regime, $T \gg m$ (and $T \gg \mu$).
  In this case, the distribution function (5.35) can be approximated to

$$f(\overrightarrow{p}) \simeq \frac{1}{\exp(|\overrightarrow{p}|/T) \pm 1}, \tag{5.40}$$

such that

$$n = \begin{cases} \frac{\varsigma(3)}{\pi^2} g T^3 & \text{bosons,} \\ \\ \frac{3}{4}\frac{\varsigma(3)}{\pi^2} g T^3 & \text{fermions,} \end{cases} \tag{5.41}$$

$$\rho = \begin{cases} \frac{\pi^2}{30} g T^4 & \text{bosons,} \\ \\ \frac{7}{8}\frac{\pi^2}{30} g T^4 & \text{fermions,} \end{cases} \tag{5.42}$$

$$p = \frac{\rho}{3}, \tag{5.43}$$

with $\varsigma(3) \approx 1.20206$, the Riemann zeta function of 3.

5.3.1 Neutrino Decoupling

In the particular case of neutrinos, when 1 MeV $\lesssim T \lesssim m_\mu$, they are coupled to the primordial plasma via the weak interactions, so that neutrinos are in thermal equilibrium, holding a Fermi-Dirac distribution, equation (5.35) with the + sign. Thermal equilibrium ensures that $T_\nu = T_e = T_\gamma$. While temperature falls down, weak interactions become ineffective to keep neutrinos in thermal contact with the electromagnetic plasma. This is the moment of *neutrino decoupling*, and the temperature can be computed equating the rate of weak processes to the Hubble expansion rate $\Gamma_{\text{weak}} \approx H$, taking into account that at that time the Universe is dominated by radiation:

$$\Gamma_{\text{weak}} = \langle \sigma_{\text{weak}} v \rangle n \sim G_F^2 T^5, \tag{5.44}$$

$$H^2 = \frac{8\pi G_N}{3} \rho_{\text{rad}} = \frac{8\pi \rho_{\text{rad}}}{3 M_{\text{Plank}}^2}. \tag{5.45}$$

Considering (5.42), $\rho_{\text{rad}} \sim T^4$, so

$$\begin{aligned} G_F^2 T^5 &\approx \sqrt{\frac{8\pi T^4}{3 M_{\text{Plank}}^2}} \\ T_{\text{dec}}^3 &\approx 10^{-9}\ \text{GeV}^3 \\ T_{\text{dec}} &\approx 1\ \text{MeV}, \end{aligned} \tag{5.46}$$

so, neutrinos decoupled at a temperature of 1 Mev, approximately.

Actually, if one takes into account that ν_e have both, charged and neutral current interactions with the electrons and positrons present in the plasma at the time, those remain in contact with the electromagnetic plasma longer time, so that a precise computation of the neutrino decoupling temperature gives [110]

$$T_{\rm dec}(\nu_e) = 1.34 \text{ MeV}, \tag{5.47}$$
$$T_{\rm dec}(\nu_{\mu,\tau}) = 1.5 \text{ MeV}. \tag{5.48}$$

From this moment neutrinos are free-streaming, but they keep the same Fermi-Dirac spectrum,

$$f(\overrightarrow{p}) = \left[\exp\left(\frac{p-\mu_\nu}{T}\right)+1\right]^{-1}. \tag{5.49}$$

This is so because both neutrino momenta and temperature redshift identically with the universe expansion. On the other hand, neutrinos are ultrarelativistic at decoupling time ($m_\nu \ll T_{\rm dec}$), so the momentum distribution (5.49) does not depend on the neutrino masses, even after decoupling [19].

After neutrino decoupling, when $T \sim m_e$, electrons and positrons annihilate by the process

$$e^+ + e^- \to \gamma + \gamma, \tag{5.50}$$

heating the potons in the plasma, but not the decoupled neutrinos.

It is possible to find the relation between neutrino and photon temperatures using the conservation of the entropy before and after the process of photon decoupling. Before, the electromagnetic plasma is formed by $e^\pm$'s and γ's, while after, the photons are travelling freely with temperature T_γ. Since neutrinos decoupled earlier, their temperature T_ν remains the same during the rest of the evolution of the Universe, and one has that this temperature is precisely the temperature of the electromagnetic plasma just after neutrino decoupling.

The entropy of the plasma after neutrino decoupling can be expressed as

$$S_i = \frac{p+\rho}{T_\nu}\,V = \frac{(1+w)\rho}{T_\nu}\,V, \tag{5.51}$$

where V is the volume of the expanding Universe, and p and ρ are the pressure and energy densities of the electromagnetic plasma (the equation of state has been used here). It is necessary to compute the total energy density of the plasma, resulting from the sum of the different constituents: electrons, positrons and photons, all of them being relativistic (meaning $w = 1/3$ in (5.51)); so, considering (5.40):

$$\begin{aligned}\rho &= \rho_{e^\pm} + \rho_\gamma \\ &= \frac{7\pi^2}{240} g_{e^\pm} T_\nu^4 + \frac{\pi^2}{30} g_\gamma T_\nu^4 \\ &= \left(\frac{7}{8} g_{e^\pm} + g_\gamma\right)\frac{\pi^2}{30} T_\nu^4.\end{aligned} \tag{5.52}$$

g_i indicates the corresponding number of degrees of freedom, being $g_{e^\pm} = 2 \times 2$ and $g_\gamma = 2$.

On the other hand, after photon decoupling,

$$S_f = \frac{p_\gamma + \rho_\gamma}{T_\gamma} V = \frac{(1+w)\rho_\gamma}{T_\gamma} V, \tag{5.53}$$

with $w = 1/3$ and

$$\rho_\gamma = \frac{\pi^2}{30} g_\gamma T_\gamma^4, \qquad g_\gamma = 2. \tag{5.54}$$

Then, the entropy before and after photon decoupling are, respectively,

$$S_i = \frac{11}{2} \left(\frac{\pi^2}{90} \right) T_\nu^3 \tag{5.55}$$

$$S_f = 2 \left(\frac{\pi^2}{90} \right) T_\gamma^3, \tag{5.56}$$

so that the relation between the neutrino and photon temperatures is

$$\frac{T_\nu}{T_\gamma} = \left(\frac{4}{11} \right)^{1/3}. \tag{5.57}$$

Measurements of the CMBR have established that [63]

$$T_\gamma^0 = 2.725 \text{ K} = 2.348 \times 10^{-4} \text{ eV}, \tag{5.58}$$

hence

$$T_\nu^0 = 1.945 \text{ K} = 1.676 \times 10^{-4} \text{ eV}, \tag{5.59}$$

which is a very low temperature, difficulting the Cosmic Neutrino Background detection.

5.4 Energy density of neutrinos

Being relativistic, the present neutrino number density (per flavor) is given by (5.41), with the temperature given in (5.59):

$$\begin{aligned} n_{\nu_i} &= \frac{3}{4} \frac{\varsigma(3)}{\pi^2} g_{\nu_i} T_\nu^3 \\ &= \frac{6}{4} \frac{\varsigma(3)}{\pi^2} \left(1.676 \times 10^{-4} \text{ eV} \right)^3 \\ &= 112.1 \text{ cm}^{-3}. \end{aligned} \tag{5.60}$$

The corresponding contribution to the present energy density of relativistic neutrinos ($m_\nu \ll T$) is computed using (5.42)

$$\begin{aligned}\Omega_\nu &= \frac{1}{\rho_c}\left(\frac{7}{8}\frac{\pi^2}{30}g_\nu T_\nu^4\right)\\ &= \frac{7}{8}g_\nu\left(\frac{T_\nu}{T_\gamma}\right)^4\frac{\Omega_\gamma}{g_\gamma}\\ &= \frac{7}{8}g_\nu\left(\frac{4}{11}\right)^{4/3}2.3\\ &= 1.1\times10^{-5},\end{aligned} \tag{5.61}$$

with $g_\nu = 2$, and where (5.57) was used, as well as the value of Ω_γ of table 5.2.

On the other hand, nonrelativistic massive neutrinos ($m_\nu \gg T$) may give a significant contribution to the energy density of the Universe. From equation (5.38), one has that for each neutrino species

$$\rho_{\nu_i} = m_i n_i, \tag{5.62}$$

which, dividing by the critical energy density of the Universe ρ_c equation (5.20), and using the result of the number density of neutrinos (5.60), can be written as

$$\Omega_{\nu_i}h^2 = \frac{m_i}{94.05\text{ eV}}, \tag{5.63}$$

therefore the total contribution of neutrinos to the energy density of the Universe is

$$\Omega_\nu h^2 = \frac{\sum_i m_i}{94.05\text{ eV}}. \tag{5.64}$$

Equation (5.64) can be used to get a bound on the sum of neutrino masses from the measurements of the matter content of the Universe $\Omega_m h^2 = 0.1358^{+0.0037}_{-0.0036}$ [32]:

$$\sum_i m_i \lesssim 12.8\text{ eV}. \tag{5.65}$$

This limit is commonly known as the *Gershtein-Zeldovich limit*.

Nevertheless, this is only one possibility to get a limit on the sum of neutrino masses. Constraining this parameter depends on the assumed cosmological model and on the combination of cosmological data used. Table 5.4 shows some of the resulting constrains on $\sum m_\nu$ coming from different analyses.

In addition, the bound on $\sum m_\nu$ depends also on the number of neutrinos, so for example, the author of reference [36] found

$$\begin{aligned}\sum m_\nu &\leq 1.01\text{ eV} \quad \text{for} \quad N_\nu = 3,\\ \sum m_\nu &\leq 1.38\text{ eV} \quad \text{for} \quad N_\nu = 4,\\ \sum m_\nu &\leq 2.12\text{ eV} \quad \text{for} \quad N_\nu = 5,\end{aligned} \tag{5.66}$$

at 95% confidence.

Used data set	$\sum m_\nu$	**Reference**
Cluster Number Density	< 2.4 eV	[111]
WMAP5	< 1.3 eV	[32]
SDSS + WMAP3	< 0.9 eV	[112]
WMAP5 + BAO + SNe	< 0.61 eV	[32]
WMAP3 + SDSS + SNLS + BAO + CMF	< 0.56 eV	[41]
CMB + LSS	< 0.48 eV	[113]
WMAP1 + SDSS + Lyα	< 0.42 eV	[114]
CMB + HST + SNe + BAO + Lyα	< 0.19 eV	[115]
CMB + SDSS + 2dF + SNe + Lyα	< 0.17 eV	[116]

Table 5.2: Constrains at 95 C.L. on the sum of the neutrino masses from various data set in the literature (taken from [117]). CMB means the collection of CMB data sets; LSS means combination of SDSS and 2dF data sets; SNLS is the Supernova Legacy Survey; CMF is the cluster mass function ; Lyα are the clustering measurements of the Lyman-α forest; BAO stands for Baryon Acoustic Oscillation data.

5.5 Relativistic particles in the Universe

The total energy density of the Universe in form of radiation is computed as the sum of all the relativistic particles. At $T < m_e$, the radiation content of the Universe is given by

$$\begin{aligned}\rho_{\rm rad} &= \rho_\gamma + \rho_\nu \\ &= \frac{\pi^2}{15}T_\gamma^4 + \frac{7}{8}\frac{\pi^2}{15} \times 3 \times T_\nu^4 \\ &= \left[1 + \frac{7}{8}\left(\frac{4}{11}\right)^{4/3} \times 3\right]\frac{\pi^2}{15}T_\gamma^4 \\ &= \left[1 + \frac{7}{8}\left(\frac{4}{11}\right)^{4/3} \times 3\right]\rho_\gamma, \end{aligned} \tag{5.67}$$

where has been made evident that there are $N_\nu = 3$ active neutrinos which contribute to the radiation content of the Universe.

However, it is useful to rewrite (5.67) defining an *effective number of neutrino species* N_{eff} (or effective number of relativistic degrees of freedom), as

$$\rho_{\rm rad} = \left[1 + \frac{7}{8}\left(\frac{4}{11}\right)^{4/3} N_{\rm eff}\right]\rho_\gamma. \tag{5.68}$$

It is important to remark that the possible contributors for the extra radiation can be different kind of particles (scalar, pseudoscalars, sterile neutrinos, etc.). Regarding the neutrino species, it is necessary to remind that $N_{\rm eff}$ is not exactly 3 for standard

neutrinos. As explained before, when considering the process of neutrino decoupling in the Early Universe, it must be taken into account that the decoupling temperature $T_\nu^{\rm dec}$, is close to the electron mass m_e, so that neutrinos share some of the entropy released in the photon heating process $e^+ e^- \to \gamma\gamma$, making the neutrino spectra to be modified from its normal form (Fermi-Dirac distribution). The net effect of the complete process gives the effective number of relativistic neutrino species to be $N_{\rm eff} \simeq 3.046$ [118, 19, 108, 119].

Experimental data as well as models which describe cosmological observations, also give constrains on the number of neutrinos. For instance, the WMAP experiment [32], in the recently realeased data analysis [34], has found a limit on the number of light neutrino families,

$$N_{\rm eff} > 2.3 \quad (95\%\text{C.L.}), \tag{5.69}$$

and with the addition of Baryon Acoustic Oscillation and Super Novae data,

$$N_{\rm eff} = 4.4 \pm 1.5, \tag{5.70}$$

but constrains on $N_{\rm eff}$ are very dependent of the model and the used experimental set of data.

5.6 Constraints on a light non-thermal sterile neutrino

Throughout this text, we have emphasized that neutrino oscillation is a well studied phenomenon, confirmed by strong experimental evidences. Most experimental results are well explained with a three-neutrino oscillation model, involving two independent and well-measured square-mass differences, equations (2.54) and (2.57). However, we have seen also that there are experiment showing anomalies which do not fit in this hypothesis.

The physics behind the different anomalous results have been studied, finding diverse results. In reference [76], the MiniBooNE anomaly was explained through a renormalization of the absolute neutrino flux and a simultaneous disappearance of electron neutrinos oscillating into sterile neutrinos (with $P_{\nu_e\to\nu_e} = 0.64^{+0.08}_{-0.07}$). The LSND [66] and Gallium radioactive source experiment [80, 82, 120] anomalies were studied in reference [75], concluding that these anomalies could be interpreted as an indication of the presence of, at least, one sterile neutrino with rather large mass (few eV's). In chapter 3 of this thesis and in reference [121] the compatibility of the Gallium results with the Bugey [90] and Chooz [96] reactor experimental data were studied, concluding that such a sterile neutrino should have a mass between one and two eV's. Finally, the MiniBooNE collaboration performed global fits of MiniBooNE, LSND, KARMEN2, and Bugey experiments in presence of a fourth sterile neutrino [122] (assuming no renormalization issue for MiniBooNe unlike reference [76]). When all four experiments are combined, the compatibility between them is found to be very low (4%); however, when only three of them are included, the compatibility level is usually reasonable (the largest tension being found between LSND and Bugey). In

this analysis, the preferred value of the sterile neutrino is usually smaller than 1eV, but still of possible cosmological relevance (for instance, for all four experiments, the best fit corresponds to $\Delta m^2 \sim 0.2 - 0.3$ eV^2).

These various developments suggest that it is important to scrutinize cosmological bounds on scenarios with one light sterile neutrino, which could help ruling them out, given that current bounds on the total neutrino mass assuming just three active neutrinos are as low as $\sum m_\nu < 0.61$eV (using WMAP5, BAO and SN data [32]). This result cannot be readily applied to the models which we consider here. Indeed, scenarios with extra neutrinos require a specific cosmological analysis, for the simple reason that besides affecting the total neutrino mass, additional neutrinos also increase the abundance of relativistic particles in the early universe.

From the point of view of Cosmology, there have been many works constraining simultaneously the sum of neutrino masses and the contribution to the relativistic energy density component of the Universe, parametrized as the effective number of neutrinos (section 5.5) $N_{\rm eff}$ (see for example [110, 37, 123, 19, 38, 124]). Most of these works assume either that the heaviest neutrino (and hence the most relevant one from the point of view of free-streaming) has a thermal distribution, sharing the same value of temperature as active neutrinos, or that all neutrinos are degenerate in mass. However, the results of references [125, 126] can also be applied to the case of very light active neutrinos plus one heavier, non-necessarily thermal sterile neutrino, which is the most interesting case for explaining oscillation anomalies.

In terms of physical motivations, it is very likely that the light sterile neutrino required by the LSND anomaly acquires a thermal distribution in the early universe, through oscillations with active neutrinos in presence of a large mixing angle [127]. On the other hand, there are some proposals to avoid these contrains (for a list of some scenarios, see [128]). One of such possibilities is based on a low reheating temperature (T_R) Universe [129, 130, 131, 132, 133], in which, for a sufficiently low T_R, the sterile neutrinos could be non-thermal [134] and its production would be suppressed [131], such that usual cosmological bounds are evaded.

In absence of thermalization, cosmological bounds on the sterile neutrino mass become potentially weaker. Hence, it is interesting to study the compatibility of recently proposed scenarios with a light sterile neutrino with the most recent cosmological data, keeping in mind the possibility of a non-thermal distribution.

In this section hence we study the compatibility of cosmological experimental data (WMAP5 plus small-scale CMB data, SDSS LRG data, SNIa data from SNLS and Lya data from VHS) with the hypothesis of a sterile neutrino with the characteristics sketched above, i.e., with a mass of the order of the electron-Volt, and a contribution to $N_{\rm eff}$ smaller than one.

5.6.1 Physical effects and parametrization

If a population of free-streaming particles becomes non-relativistic after photon decoupling, its physical effects on the cosmological background and perturbation evolution are mainly described by three quantities:

1. its contribution to the relativistic density before photon decoupling, which affects the redshift of radiation/matter equality, usually parametrized by an effective neutrino number (standing for the relativistic density of the species divided by that of one massless neutrino family in the instantaneous decoupling (id) limit):

$$\Delta N_{\rm eff} \equiv \frac{\rho_s^{\rm rel}}{\rho_\nu} = \left[\frac{1}{\pi^2}\int dp\ p^3 f(p)\right] / \left[\frac{7}{8}\frac{\pi^2}{15}T_\nu^{\rm id\,4}\right] \tag{5.71}$$

   with $T_\nu^{\rm id} \equiv (4/11)^{1/3} T_\gamma$ (see equation 5.57),

2. its current energy density, which affects (i) the current energy budget of the Universe (with various consequences for the CMB and LSS spectra, depending on which other parameters are kept fixed), and (ii) the amplitude reduction in the small-scale matter power spectrum due to these extra massive free-streaming particles, parametrized by the dimensionless number ω_s:

$$\omega_s \equiv \Omega_s h^2 = \left[\frac{m}{\pi^2}\int dp\ p^2 f(p)\right] \times \left[\frac{h^2}{\rho_c^0}\right] \tag{5.72}$$

   where ρ_c^0 is the critical density today 5.20 and h the reduced Hubble parameter,

3. the comoving free-streaming length of these particles when they become non-relativistic, which controls the scale at which the suppression of small-scale matter fluctuations occurs. This length can easily be related to the average velocity of the particles today, $\langle v_s \rangle$[4].

However, for whatever assumption concerning the phase-space distribution function $f(p)$, the three numbers ($\Delta N_{\rm eff}$, ω_s, $\langle v_s \rangle$) satisfy a constraint equation. Indeed, the average velocity of the particles today (assumed to be in the non-relativistic regime) is given *exactly* by

$$\begin{aligned}\langle v_s \rangle &\equiv \frac{\int p^2 dp\, \frac{p}{m} f(p)}{\int p^2 dp\, f(p)} \\ &= \frac{7}{8}\frac{\pi^2}{15}\left(\frac{4}{11}\right)^{4/3}\frac{T_\gamma^4 h^2}{\rho_c}\frac{\Delta N_{\rm eff}}{\omega_s} \\ &= 5.618\times 10^{-6}\frac{\Delta N_{\rm eff}}{\omega_s},\end{aligned} \tag{5.73}$$

in units where $c = k_B = \hbar = 1$, and taking $T_\gamma = 2.726$ K. Hence, the three physical effects described above depend on only *two independent parameters*.

Reducing the physical impact of any population of massive free-streaming particles to these three effects (and two independent parameters) is a simplification: two models based on different non-thermal phase-space distributions $f(p)$ can in principle share

[4]The minimum comoving free-streaming wavenumber $k_{\rm fs}$ is controlled by Ω_m and by the ratio $a(t_{\rm nr})/\langle v_s(t_{\rm nr})\rangle$ evaluated when $T = m$, i.e. when $a(t_{\rm nr}) \sim \langle v_s(t_0)\rangle a(t_0)$. Given that $\langle v_s(t_{\rm nr})\rangle \sim \langle v_s(t_0)\rangle a(t_0)/a(t_{\rm nr})$, the minimum comoving free-streaming length just depends on $\langle v_s(t_0)\rangle$ and Ω_m.

the same numbers ($\Delta N_{\rm eff}$, ω_s, $\langle v_s \rangle$) and impact the matter power spectrum differently. Indeed, the free-streaming effect depends on the details of $f(p)$ (including high statistical momenta like $\int dp\, p^4 f(p)$, etc.) However, the conclusions of Ref. [123] indicate that for many models with non-thermal distorsions, observable effects can indeed be parametrized by two combinations of ($\Delta N_{\rm eff}$, ω_s, $\langle v_s \rangle$) with good accuracy: other independent parameters would be very difficult to observe[5].

Let us compute the three parameters ($\Delta N_{\rm eff}$, ω_s, $\langle v_s \rangle$) for simple cases. For one species of thermalized free-streaming particles with mass m_s, sharing the same temperature as active neutrinos in the instantaneous decoupling limit, one gets:

$$\Delta N_{\rm eff} = 1, \tag{5.74a}$$

$$\omega_s = \frac{m_s}{94.05 \text{ eV}}, \tag{5.74b}$$

$$\langle v_s \rangle = \frac{7\pi^4}{180\zeta(3)} \frac{T_\nu^{\rm id}}{m_s} = \frac{0.5283 \text{ meV}}{m_s}. \tag{5.74c}$$

For a light thermal relic with a Fermi-Dirac distribution and a different temperature T_s, these quantities become

$$\Delta N_{\rm eff} = \left(\frac{T_s}{T_\nu^{\rm id}} \right)^4, \tag{5.75a}$$

$$\omega_s = \frac{m_s}{94.05\text{eV}} \left(\frac{T_s}{T_\nu^{\rm id}} \right)^3, \tag{5.75b}$$

$$\langle v_s \rangle = \frac{0.5283 \text{ meV}}{m_s} \left(\frac{T_s}{T_\nu^{\rm id}} \right) . \tag{5.75c}$$

For a non-thermal relic with a free function $f(p)$, there is an infinity of possible models. A popular one is the Dodelson-Widrow scenario [136], motivated by early active-sterile neutrino oscillations in the limit of small mixing angle and zero leptonic asymmetry, which corresponds to the phase-space distribution

$$f(p) = \frac{\chi}{e^{p/T_\nu} + 1} \tag{5.76}$$

where χ is an arbitrary normalization factor. In this case, in the approximation $T_\nu = T_\nu^{\rm id}$, the three "observable" parameters read

$$\Delta N_{\rm eff} = \chi, \tag{5.77a}$$

$$\omega_s = \frac{m_s}{94.05\text{eV}} \chi, \tag{5.77b}$$

$$\langle v_s \rangle = \frac{0.5283 \text{ meV}}{m_s} . \tag{5.77c}$$

[5] This conclusion does not apply when the non-thermal distribution $f(p)$ has a sharp peak close to $p = 0$. In this case, particles with very small momentum should be counted within the CDM component, not within the extra massive free-streaming component. Otherwise, one would obtain values of ω_s and $\langle v_s \rangle$ based on an averages between cold and hot/warm particles; then, these parameters would not capture the correct physical effects (see [135])

Hence, a Dodelson-Widrow (DW) model shares that same "observable" parameters ($\Delta N_{\rm eff}$, ω_s, $\langle v_s \rangle$) as a thermal model with $m_s^{\rm thermal} = m_s^{\rm DW} \chi^{1/4}$ and $T_s = \chi^{1/4} T_\nu$. Actually, for these two models, the degeneracy is exact: it can be shown by a change of variable in the background and linear perturbation equations that the two models are strictly equivalent from the point of view of cosmological observables [137, 123]. As mentioned before, in the general case, two models sharing the same ($\Delta N_{\rm eff}$, ω_s, $\langle v_s \rangle$) are not strictly equivalent, but can be thought to be hardly distinguishable even with future cosmological data. For instance, the low-temperature reheating model analyzed in [130, 131] leads to a distribution of the form

$$f(p) = \frac{\chi p}{e^{p/T_\nu} + 1} \ . \tag{5.78}$$

This model would in principle deserve a specific analysis, but in good approximation we can expect that by only exploring the parameter space of thermal models (or equivalently, of DW models), we will obtain some very generic results, covering in good approximation most possibilities for the non-thermal distorsions.

5.6.2 Data for the Analysis

In the following sections, we will present the results of various runs based on the Boltzmann code CAMB [138] and cosmological parameter extraction code CosmoMC [139]. We modified CAMB in order to implement the proper phase-space distribution $f(p)$ of the thermal or DW model. For simplicity, we assumed in all runs that the three active neutrinos can be described as massless particles. In order to obtain a Bayesian probability distribution for each cosmological parameters, we ran CosmoMC with flat priors on the usual set of six parameters ω_b, $\omega_{\rm dm} = \omega_s + \omega_{\rm cdm}$, θ, τ, A_s, n_s (see e.g. [140]), plus two extra parameters describing the sterile neutrino sector, that will be described in the next sections. We choose the following data set: WMAP5 [33] plus small-scale CMB data (ACBAR [141], CBI [142], Boomerang [113]), the galaxy power spectrum of the SDSS LRG [112] with flat prior on Q [143, 144], SNIa data from SNLS [145] and conservative Lyman-α data from VHS [146]. We do not include more recent Lyman-α data sets, which have much smaller errorbars, but for which the deconvolution of the non-linear evolution is strongly model-dependent.

5.6.3 General analysis

Our first goal is to obtain simple results with a wide range of applications. Hence, we should not parametrize the effect of sterile neutrinos with e.g. their mass or temperature: in that case, our results would strongly depend on underlying assumptions for $f(p)$. It is clear from section 5.6.1 that nearly "universal" results can be obtained by employing two combinations of the "observable parameters" $\Delta N_{\rm eff}$, ω_s and $\langle v_s \rangle$ (and eventually of other parameters of the ΛCDM model). Here we choose to vary the current density fraction $f_s = \omega_s / (\omega_s + \omega_{\rm cdm})$ and the current velocity dispersion $\langle v_s \rangle$. As will be clear from our results, these two parameters capture the dominant observable

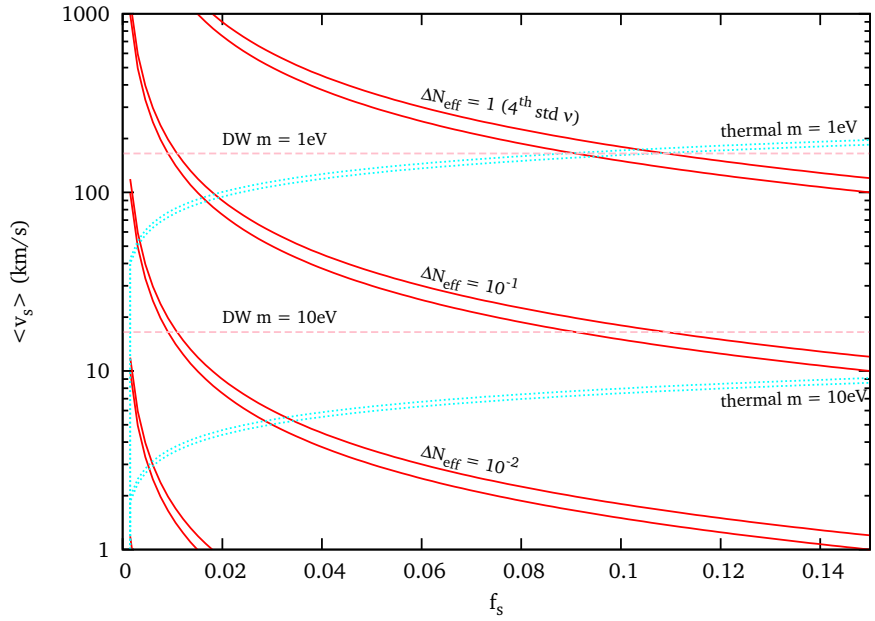

Figure 5.3: The parameter space $(f_s, \langle v_s \rangle)$ chosen in our general analysis. The thin bands delimited by solid lines show regions of equal $\Delta N_{\rm eff}$ (assuming $\omega_{\rm dm} = 0.11 \pm 0.01$); these bands are fully model-independent. We also show the model-dependent regions of equal mass, delimited by dotted lines for the case of early decoupled thermal relics, and consisting in horizontal dashed lines for Dodelson-Widrow sterile neutrinos.

effects, and lead to very clear bounds, since their correlation with other ΛCDM model parameters is insignificant. Our limits on f_s and $\langle v_s \rangle$ apply exactly to the thermal case and DW case, and approximately to most other cases (modulo the caveat described in the second footnote of section 5.6.1).

Our parameter space is represented in figure 5.3. We adopt a logarithmic scale for $\langle v_s \rangle$ and display the interesting range

$$1 \text{ km/s} < \langle v_s \rangle < 1000 \text{ km/s} \, . \tag{5.79}$$

Indeed, with out dataset, particles with smaller velocities would be indistinguishable from cold dark matter; instead, particles with larger velocities would either have $\Delta N_{\rm eff} > 1$ (a case beyond the motivations of this work, and anyway very constrained by the data) or $f_s < 0.02$ (being indistinguishable from extra relativistic degrees of freedom). Assuming a particular value for $\omega_{\rm dm} = \omega_s + \omega_{\rm cdm}$ and for $\Delta N_{\rm eff}$, it is possible to compute the velocity dispersion $\langle v_s \rangle$ as a function of f_s. Since the CMB and LSS data give precise constraints on $\omega_{\rm dm}$, regions of equal $\Delta N_{\rm eff}$ correspond to thin bands in the $(f_s, \langle v_s \rangle)$ plane. We show these bands in figure 5.3 for $10^{-3} < \Delta N_{\rm eff} < 1$ under the assumption that $\omega_{\rm dm} = 0.11 \pm 0.01$, which correspond roughly to the 95%

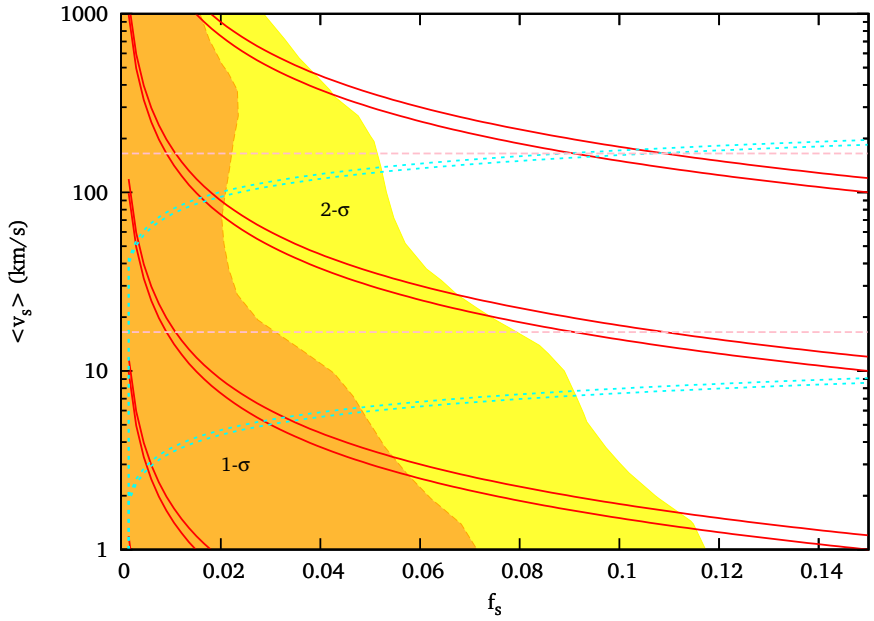

Figure 5.4: Same to figure 5.3 with, in addition, the regions allowed at the 68.3% (1σ), 95.4% (2σ) and 99.7% (3σ) C.L. by our cosmological data set, in a Bayesian analysis with flat priors on f_s and $\log_{10}\langle v_s\rangle$ within the displayed range.

confidence limits (C.L.) from all our runs. These iso-$\Delta N_{\rm eff}$ bands are completely model-independent.

Instead, regions of equal mass can only be plotted for a particular model. In figure 5.3, we show the bands corresponding to $m = 1$ eV and 10 eV, either in the case of early decoupled thermal relics (dotted lines) or in the DW case (dashed lines). For any given mass, these bands intersect each other in a location corresponding to the case of one fourth standard neutrino species with $\Delta N_{\rm eff} = 1$.

We ran CosmoMC with top-hat priors on f_s (in the physical range $[0, 1]$) and on $\log_{10}[\langle v_s\rangle/1\text{km/s}]$ (in the range $[0, 3]$ motivated by the previous discussion). Our results are summarized in figure 5.4. We see that the upper bound on f_s decreases smoothly as the velocity dispersion increases: when the particles have a larger velocity dispersion, their free-streaming wavelength is larger, so the step-like suppression in the power spectrum (which amplitude depends on f_s) is more constrained. For $\langle v_s\rangle \sim 1$ km/s, we find $f_s \lesssim 0.1$ at the 2σ C.L., while for $\langle v_s\rangle \sim 100$ km/s, we find $f_s \lesssim 0.06$ at the 2σ C.L. When the velocity dispersion becomes larger than 100 km/s, the upper bound on f_s decreases even faster as a function of $\langle v_s\rangle$. This is the case of a HDM component with significant contribution to the number of relativistic d.o.f., for which the observational bounds derive from a combination of the first and second effects described in section 5.6.1: in this limit, in addition to being sensitive to the free-streaming effect, the data disfavor a significant increase of the total radiation density corresponding to $\Delta N_{\rm eff}$ of

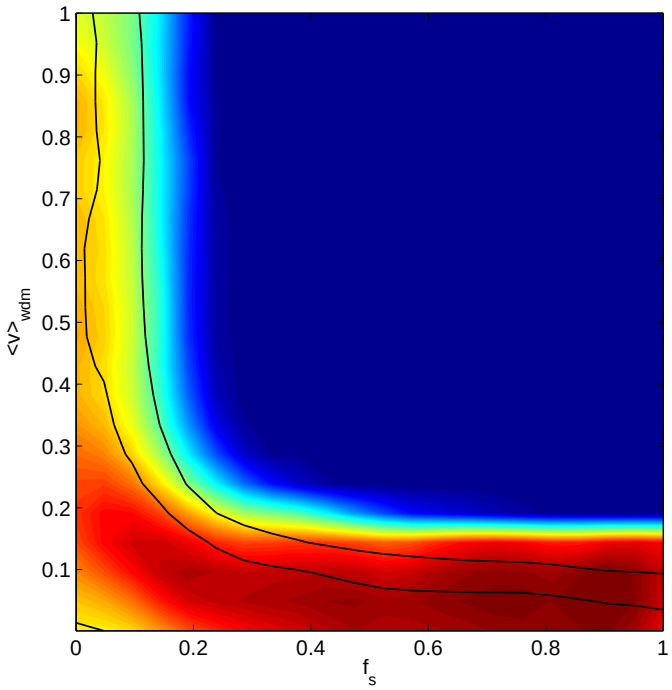

Figure 5.5: 1σ, 2σ and 3σ contours of the marginalized likelihood for the two parameters (f_s, $\langle v_s \rangle$), with different priors than in previous figures. As explained in the text, this plot shows the region where the sterile neutrino is heavy and behaves like warm dark matter, in complement to Figure 1, which is based on a different range/prior for $\langle v_s \rangle$ adapted to the case of a light, hot sterile neutrino.

order one or larger.

We should stress that the details of our results depend on the underlying priors. For instance, one could use a flat prior on $\langle v_s \rangle$ instead of its logarithm. Running in the range $0 < \langle v_s \rangle < 1000$ km/s with such a prior would give more focus on the large-$\langle v_s \rangle$ allowed region of figure 5.4. However, it would be more interesting to focus on small velocities, in order to understand how our results can be extended without any discontinuity to the case of warmer and heavier dark matter. For this purpose, we ran CosmoMC with a top-hat prior on $0 < \langle v_s \rangle < 1$ km/s, and obtained the results shown in figure 5.5. These results are identical to those published in reference [147] (figure 7). By gluing figure 5.4 on top of 5.5, one can obtain a full coverage of the parameter space of ΛCDM models completed by one extra (hot or warm) dark matter species. Figure 5.5 shows the transition from the region in which this extra species is indistinguishable from cold dark matter (when $\langle v_s \rangle \leq 0.1$ km/s, the fraction f_s is unconstrained) to the region in which it is warm (for $0.4 \leq \langle v_s \rangle \leq 1$ km/s, there is a nearly constant bound $f_s \lesssim 0.1$ at the 2-σ level). Figure 5.4 shows instead the transition from warm particles to hot particles (with velocities comparable to those of

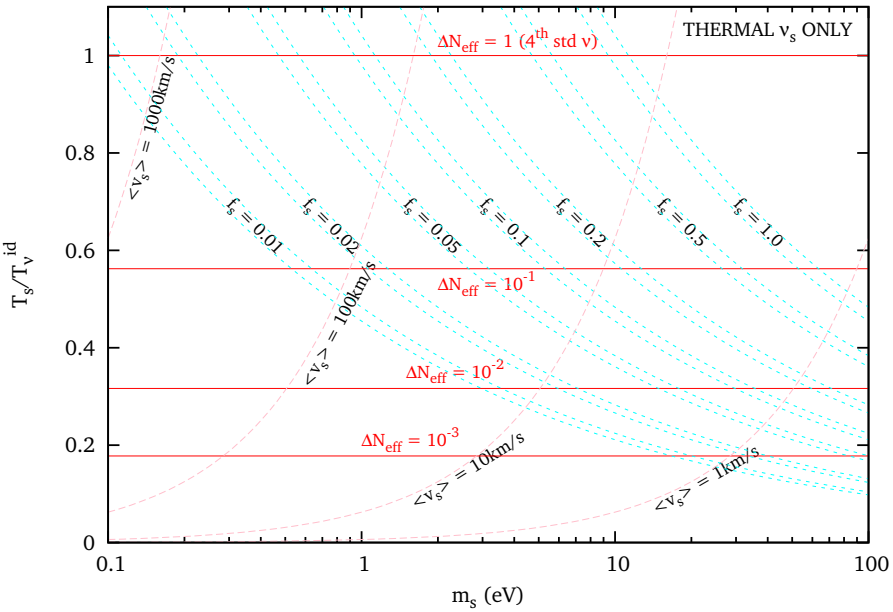

Figure 5.6: The parameter space (m_s,$T_s/T_\nu^{\rm id}$) used in the particular case of early decoupled thermal relics of temperature T_s (with $T_\nu^{\rm id} \equiv (4/11)^{1/3} T_\gamma$). The thin bands delimitated by dot-dashed lines show regions of equal f_s (assuming $\omega_{\rm dm} = 0.11 \pm 0.01$); the dotted lines correspond to fixed values of the velocity dispersion today; horizontal solid lines to fixed $\Delta N_{\rm eff}$.

active neutrinos). The two plots perfectly match each other along the $\langle v_s \rangle = 1$ km/s axis, on which the sterile neutrino fraction is bounded by $f_s \lesssim 0.1$ (2-σ).

5.6.4 Mass/temperature bounds in the thermal case

We now focus on the particular case of early decoupled thermal relics, with a Fermi-Dirac distribution and a temperature T_s. These models can be parametrized by the mass m_s and the temperature in units of the neutrino temperature, $T_s/T_\nu^{\rm id}$. Our parameter space – and the correspondence with the previous parameters $\Delta N_{\rm eff}$, f_s, $\langle v_s \rangle$ – is shown in figure 5.6. In this analysis, we want to focus on light sterile neutrinos rather than WDM; hence we are not interested in velocities smaller than 1 km/s today. We are not interested either in the case of enhanced particles with $\Delta N_{\rm eff} > 1$. Then, as can be checked in figure 5.6, the ensemble of interesting models can be covered by taking a top-hat prior on $\log_{10}(m_s/1\ {\rm eV})$ in the range $[-1, 2]$, and on $T_s/T_\nu^{\rm id}$ in the range $[0, 1]$.

The likelihood contours obtained for this case are shown in figure 5.7. They are consistent with our previous results: when $\Delta N_{\rm eff} \sim 10^{-2}$ (and hence $T_s/T_\nu^{\rm id} \sim 0.3$), the upper bound on the sterile neutrino fraction is $f_s < 0.1$ at the 2σ C.L.; then this

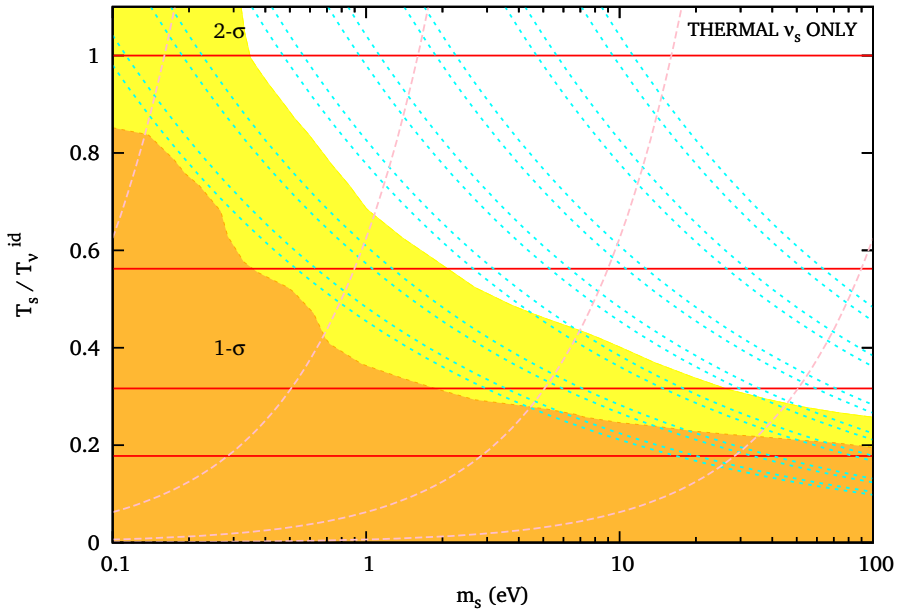

Figure 5.7: Same to figure 5.6 with, in addition, the regions allowed at the 68.3% (1σ), 95.4% (2σ) and 99.7% (3σ) C.L. by our cosmological data set, in a Bayesian analysis with flat priors on $\log_{10}(m_s)$ and $T_s/T_\nu^{\rm id}$ within the displayed range.

bound decreases smoothly when T_s increases. For a fourth standard neutrino with $T_s = T_\nu^{\rm id}$, the 2σ C.L. (resp. 3σ C.L.) bound is $m_s \lesssim 0.4$ eV (resp. 0.9 eV).

This figure can be conveniently used for model building: for a given value of the mass, it shows what should be the maximal temperature of the thermal relics in order to cope with cosmological observations; knowing this information and assuming a particular extension of the particle physics standard model, one can derive limits on the decoupling time of the particle. For instance, for a mass of $m_s = 0.5$ eV one gets $T_s/T_\nu^{\rm id} \lesssim 0.9$; for $m_s = 1$ eV, $T_s/T_\nu^{\rm id} \lesssim 0.7$; while for $m_s = 5$ eV, $T_s/T_\nu^{\rm id} \lesssim 0.5$. This figure can also be applied to thermally produced axions, like in references [148, 149].

5.6.5 Mass bounds in the DW case

Finally, for Dodelson-Widraw relics with a distribution function equal to that of standard neutrinos suppressed by a factor χ (which is equal by definition to $\Delta N_{\rm eff}$), we can parametrize the ensemble of models by m_s and χ.

Our parameter space – and the correspondence with f_s, $\langle v_s \rangle$ – is shown in figure 5.8. Like in the previous section, we are not interested in a current velocity dispersion smaller than 1 km/s today. Then, as can be checked in figure 5.8, the ensemble of interesting models can be covered by taking a top-hat prior on $\log_{10}(m_s/1\ {\rm eV})$ in the range $[-1, 2]$; in this range, values of χ smaller than 10^{-2} would correspond to tiny

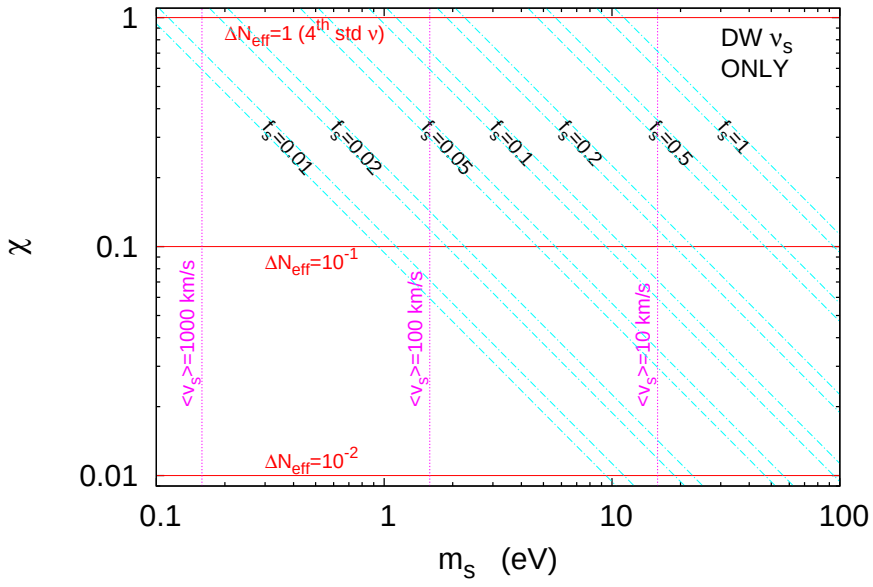

Figure 5.8: The parameter space (m_s,χ) used in the particular case of DW relics. The thin bands delimited by dot-dashed lines show regions of equal f_s (assuming $\omega_{\rm dm} = 0.11\pm0.01$); the dotted lines correspond to fixed values of the velocity dispersion today; horizontal solid lines to fixed $\Delta N_{\rm eff}$.

values of f_s, i.e. to particles indistinguishable from massless particles; so, we can take a flat prior on $\log_{10}(\chi)$ in the range $[-2, 0]$.

The likelihood contours obtained for this case are shown in figure 5.9. We are not surprised to find once more an allowed region corresponding to $f_s \lesssim 0.1$ at the 2σ C.L. when $\Delta N_{\rm eff} = \chi \sim 10^{-2}$ is negligible with respect to one, or less when $\Delta N_{\rm eff}$ grows closer to one. For a fourth standard neutrino with $T_s = T_\nu^{\rm id}$, the two definitions of the mass (following from the thermal or from the DW cases) are equivalent, and indeed we find $m_s \lesssim 0.4$ eV (2σ C.L.) or $m_s \lesssim 0.9$ eV (3σ C.L.) like in section 5.6.4.

This figure can also be useful for model building: for a given value of the mass, it shows what should be the maximal value of χ compatible with cosmological observations; in turn, this information can be used to put bounds on the mixing angle between this relic and active neutrinos in non-resonant production models *à la* Dodelson & Widrow. For instance, for a mass of $m_s = 1$ eV, the 2σ C.L. gives $\chi \lesssim 0.5$; for $m_s = 2$ eV, we get $\chi \lesssim 0.2$; while for $m_s = 5$ eV, we get $\chi \lesssim 0.1$.

5.6.6 Comparison with previous work

The ensemble of cosmological models that we are exploring here is not different from that studied by Dodelson, Melchiorri & Slosar [126] (called later DMS) or by Cirelli

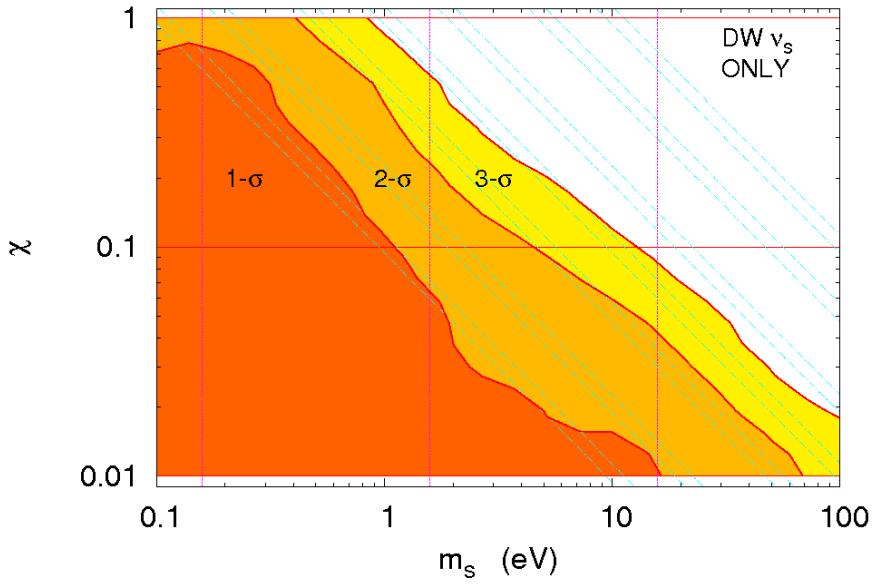

Figure 5.9: Same to figure 5.8 with, in addition, the regions allowed at the 68.3% (1σ), 95.4% (2σ) and 99.7% (3σ) C.L. by our cosmological data set, in a Bayesian analysis with flat priors on $\log_{10}(m_s)$ and $\log_{10}(\chi)$ within the displayed range.

& Strumia [125] (called later CS); the difference between these works and the present analysis consists in a different choice of parameters, priors, data set, and also methodology in the case of CS.

For instance, figure 6a of CS presents constrains in the space $(\log_{10}\Delta N_{\rm eff}, \log_{10} m_s)$ assuming a DW scenario. Hence, their parameter space is identical to the one we used in section 5.6.5, excepted for the prior range (which is wider in their case). As far as the data set is concerned, CS use some CMB and galaxy spectrum measurements which are slightly obsolete by now; on the other hand, they employ some additional information derived from BAO experiments, and use SDSS Lyman-α data points that we conservatively excluded from this analysis, since they assume a ΛCDM cosmology (this last difference is only relevant in the WDM limit). Finally, CS performed a frequentist analysis, and their bounds are obtained by minimizing the χ^2 over extra parameters (while in the present Bayesian analysis, we marginalize over them given the priors).

In order to compare our results with CS, we performed a run with top-hat priors on $\log_{10}\chi = \log_{10}(\Delta N_{\rm eff})$ in the range $[-3, 1]$, and on $\log_{10}(m_s/1\ {\rm eV})$ in the range $[-1, 3]$. In this particular run we compute the 90%, 99% and 99.9% C.L., following CS. Our results are shown in figure 5.11, and are consistent with those of our general analysis.

In spite of the different data set and methodology, the 90% and 99% contours are

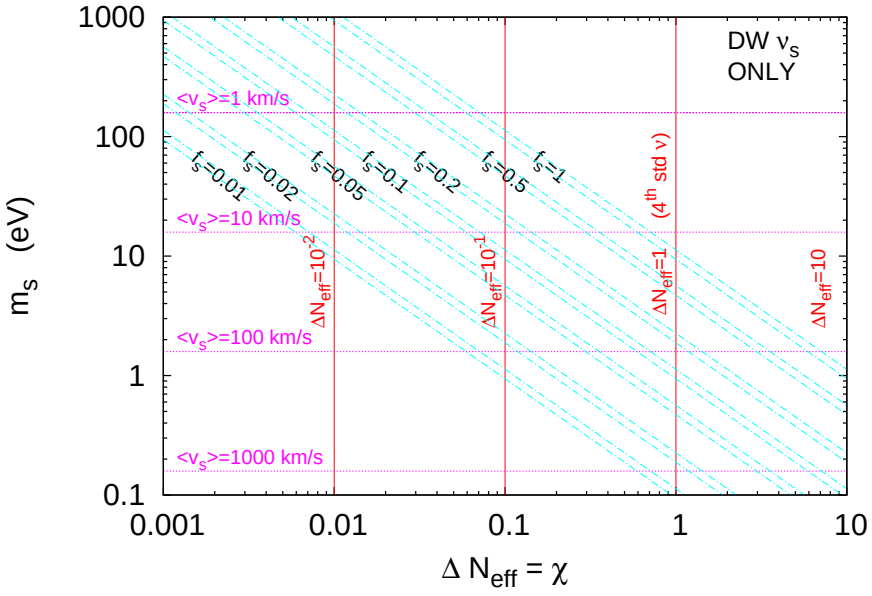

Figure 5.10: The parameter space ($\Delta N_{\rm eff}$,m_s) used for comparison with Cirelli & Strumia in the particular case of DW relics. The thin bands delimited by dot-dashed lines show regions of equal f_s (assuming $\omega_{\rm dm} = 0.11 \pm 0.01$); the dotted lines correspond to fixed values of the velocity dispersion today; horizontal solid lines to fixed $\Delta N_{\rm eff}$.

found to be in very good agreement with CS in most of the parameter space. The major difference lies in the small mass region, for which CS get more conservative limits on $\Delta N_{\rm eff}$ than we do, and find a preference for non-zero values of the effective neutrino number $0.5 < \Delta N_{\rm eff} < 4$ (at the 90% C.L.). This qualitative behavior has been nicely explained in references [143, 144]. It is due to the non-linear corrections applied to the theoretical linear power spectrum before comparing it with the observed SDSS and 2dF galaxy power spectra.

The approach used in this work (and in the default version of CosmoMC) consists in marginalizing over a nuisance parameter Q (describing the scale-dependence of the bias) with a flat prior. Instead, following reference [116], CS impose a gaussian prior on Q. This results in biasing the results towards larger values of $N_{\rm eff}$, and finding marginal evidence for $\Delta N_{\rm eff} > 0$. Of course, this assumption might turn out to be correct; however, it is argued in references [143, 144] that our knowledge on Q (based essentially on N-body simulations for some particular cosmological models) is still too uncertain for getting definite predictions.

The analysis of DMS is Bayesian, like ours. The authors use top-hat priors on the two parameters $-3 < \log_{10}(m_s/1\ {\rm eV}) < 1$ and $0 < \omega_s < 1$, roughly the same data set as CS, and employ the distribution function of early decoupled thermal relics.

Our results based on the same priors (but a different data set) are shown in fig-

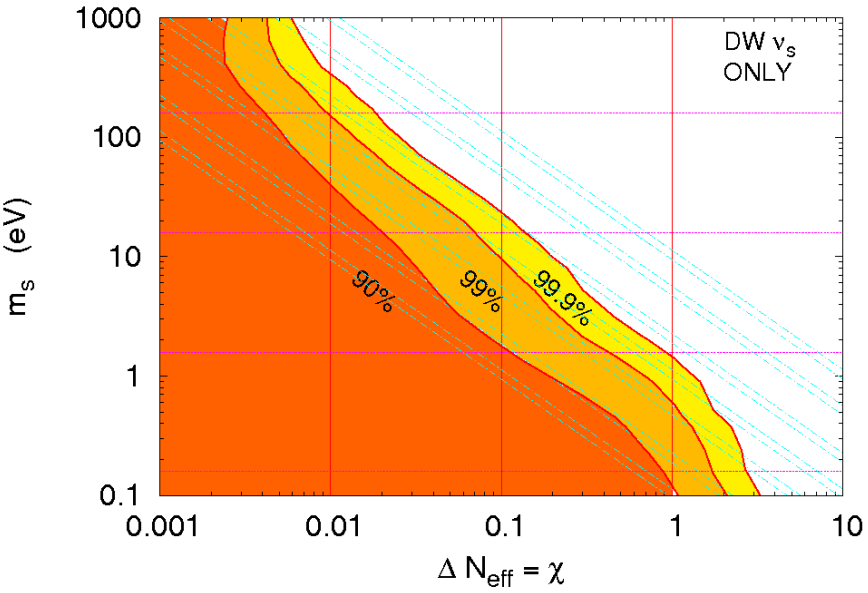

Figure 5.11: Same to 5.10 with, in addition, the regions allowed at the 90%, 99% and 99.9% C.L. by our cosmological data set, in a Bayesian analysis with flat priors on $\log_{10}(\Delta N_{\rm eff})$ and $\log_{10}(m_s)$ within the displayed range.

ure 5.13, and are consistent with the previous sections: at the 2σ level, ω_s is such that $f_s \lesssim 0.1$ for $\Delta N_{\rm eff} \sim 10^{-2}$; then, the bound on f_s (and therefore on ω_s) decreases smoothly when m_s decreases (and therefore $\langle v_s \rangle$ increases).

These results differ significantly from those of DMS, who find that the upper bound on ω_s peaks near $m_s \sim 0.25$ eV and then decreases quickly. We do not observe such a behavior: our upper bound on ω_s increases (not so smoothly, but still monotonically) when m_s increases, in agreement with all previous results in this paper. This difference is most likely due to the use made by DMS of more aggressive Lyman-α data from SDSS, of different galaxy power spectrum data, and of a prior on Q, as in CS. This data set puts stronger limits on a possible suppression of the small scale power spectrum.

Actually, in absence of sterile neutrinos, the same combination of data is known to produce very strong bounds on neutrino masses, and to prefer $\Delta N_{\rm eff}$ slightly larger than one [116]; in presence of light sterile neutrinos, the results of DMS show that this data also imposes a strong bound $\omega_s < 0.001$ for 1 eV $< m_s <$ 10 eV, due to its sensitivity to the sterile neutrino free-streaming effect. Our large scale structure data set (conservative Lyman-α data from VHS, SDSS-LRG and flat prior on Q) is not able to exclude this region.

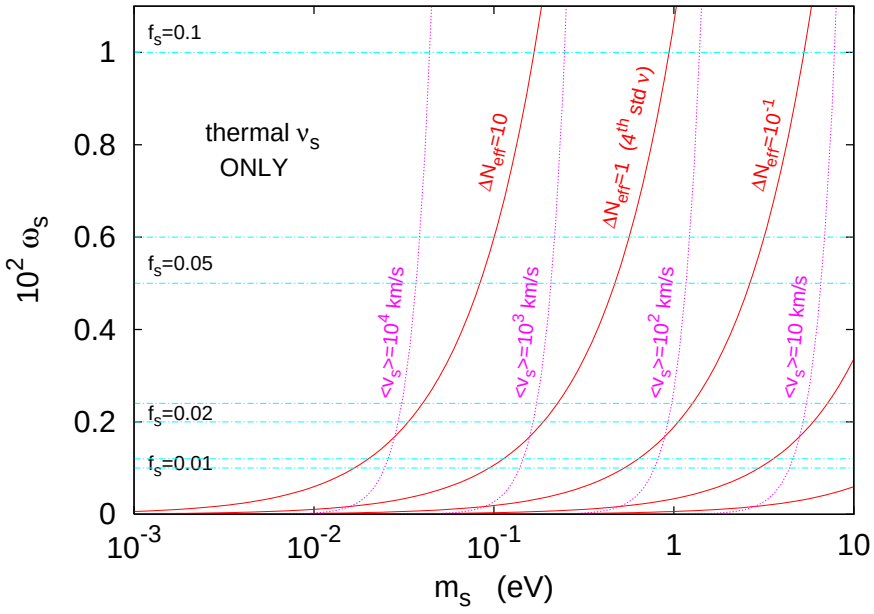

Figure 5.12: The parameter space (m_s,ω_s) used for comparison with Dodelson, Melchiorri & Slosar in the particular case of thermal relics. The thin bands delimited by dot-dashed lines show regions of equal f_s (assuming $\omega_{\rm dm} = 0.11 \pm 0.01$); the dotted lines correspond to fixed values of the velocity dispersion today; horizontal solid lines to fixed $\Delta N_{\rm eff}$.

5.7 Summary

We studied the compatibility of cosmological experimental data with the hypothesis of a non-thermal sterile neutrino with a mass in the range $0.1 - 10$ eV (or more), and a contribution to $N_{\rm eff}$ smaller than one.

We computed Bayesian confidence limits on different sets of parameters, adapted to the case of thermal relics (section 5.6.4), of non-resonantly produced sterile neutrinos *à la* Dodelson & Widrow (DW, section 5.6.5), or of generic parameters leading to nearly model-independent results (section 5.6.3). In each case, we performed a specific parameter extraction from scratch, in order to obtain reliable results assuming flat priors on the displayed parameters. For simplicity, we assumed that the masses of the three active neutrinos are negligible with respect to that of the sterile neutrino.

For a cosmological data set consisting in recent CMB and LSS data, as well as older but very conservative Lyman-α data, we found the conditional probability e.g. on the mass of a thermal relic given its temperature, or on the mass of a DW neutrino given its density suppression factor, etc. These proabilities are such that if the fourth neutrino is a standard one (with $\Delta N_{\rm eff} = 1$), it should have a mass $m_s \lesssim 0.4$ eV (2σ C.L.) or $m_s \lesssim 0.9$ eV (3σ C.L.).

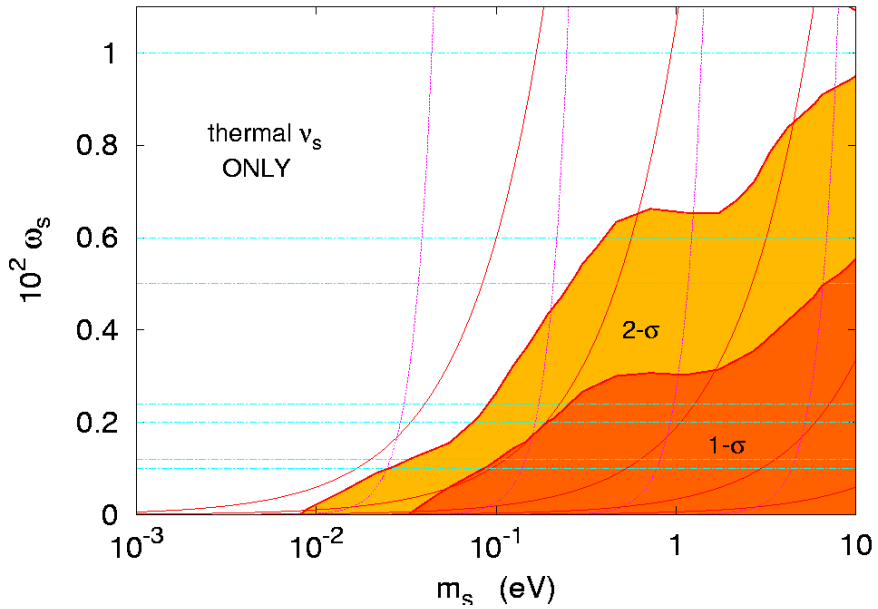

Figure 5.13: Same to figure 5.12 with, in addition, the regions allowed at the 68.3% (1σ) and 95.4% (2σ) C.L. by our cosmological data set, in a Bayesian analysis with flat priors on $\log_{10}(m_s)$ and ω_s within the displayed range.

At the 3σ C.L., a mass $m_s = 1$ eV can be accommodated with the data provided that this neutrino is thermally distributed with $T_s/T_\nu^{\rm id} \lesssim 0.97$, or non-resonantly produced with $\Delta N_{\rm eff} \lesssim 0.9$. The bounds become dramatically tighter when the mass increases.

At the same confidence level, a mass of just $m_s = 2$ eV requires either $T_s/T_\nu^{\rm id} \lesssim 0.8$ or $\Delta N_{\rm eff} \lesssim 0.5$, while a mass $m_s = 5$ eV requires $T_s/T_\nu^{\rm id} \lesssim 0.6$ or $\Delta N_{\rm eff} \lesssim 0.2$.

Our bounds can hopefully be used for constraining particle-physics-motivated models with three active and one sterile neutrinos, as those investigated recently in order to explain possible anomalies in neutrino oscillation data. Many of these models can be immediately localized in our figures 5.7 or 5.9. For sterile neutrinos or other particles which do not fall in the thermal or DW category, a good approximation consists in computing their velocity dispersion and localizing the model in our figure 5.11 [6].

Future neutrino oscillation experiments are expected to test the self-consistency of the standard three-neutrino scenario with increasing accuracy. If anomalies and indications for sterile neutrinos tend to persist, it will be particularly useful to perform joint analysis of oscillation and cosmological data, using the lines of this work for the latter part.

[6] However, this approximation could be not so good when the distribution $p^2 f(p)$ of the non-thermal relic peaks near $p = 0$, as if part of these relics were actually cold, see [135].

CHAPTER 6

CONCLUSIONS

In this Thesis we interpreted the deficit observed in the Gallium radioactive source experiments as a possible indication of the disappearance of electron neutrinos. In the framework of two-neutrino mixing, we found that there is an indication of electron neutrino disappearance due to neutrino oscillations with $\sin^2 2\theta \gtrsim 0.03$ and $\Delta m^2 \gtrsim 0.1\,\mathrm{eV}^2$.

Studying the compatibility of the data of the Gallium radioactive source experiments with the data of the Bugey and Chooz reactor antineutrino disappearance experiments, we found that the Bugey data present a hint of neutrino oscillations with $0.02 \lesssim \sin^2 2\theta \lesssim 0.08$ and $\Delta m^2 \approx 1.95\,\mathrm{eV}^2$, which is compatible with the region of the mixing parameters allowed by the analysis of the data of the Gallium radioactive source experiments.

The different combined analyses of the Gallium, Bugey and Chooz experimental data show compatibility between the two nuclear reactor experiments, between Gallium and Bugey experiments, and a marginal compatibility between Gallium and Chooz. The weak indication in favor of neutrino oscillations found in the analysis of the Bugey data persists in the combined analyses of the Bugey data with the Gallium and Chooz data. Nevertheless, the no oscillations hypothesis cannot be excluded.

The squared-mass difference $\Delta m^2 \approx 1.95\,\mathrm{eV}^2$ is too large to be compatible with the three-neutrino mixing scheme inferred from the observation of neutrino oscillations in solar, very-long-baseline reactor, atmospheric and long-baseline accelerator experiments, in which there are only two independent squared-mass differences, $\Delta m^2_{\mathrm{sol}} \approx 8 \times 10^{-5}\,\mathrm{eV}^2$ and $\Delta m^2_{\mathrm{atm}} \approx 3 \times 10^{-3}\,\mathrm{eV}^2$. Therefore, the results of our analysis indicate the possible existence of at least one light sterile neutrino ν_s.

We also analyzed the data of the I.L.L. nuclear reactor experiment in terms of $\overline{\nu}_e$ disappearance due to effective two–neutrino oscillations. We found that the combination of these data with the Bugey data show a very low compatibility. The 1σ allowed regions obtained from the I.L.L. data are almost completely inside the exclusion region

given by the Bugey analysis, showing the tension between them. Then, we decided not to use the I.L.L. nuclear reactor experimental data for additional analyses.

From the analysis of the S.R.S. reactor experiment, we found very small values of the goodness-of-fit for the oscillations and no oscillations hypotheses, indicating that the S.R.S. data are incompatible with neutrino oscillations, as well as with no oscillations. We do not have any explanation for the behavior of the data.

The analysis of the Gösgen nuclear reactor experimental data gives only upper limits for the mixing parameters, excluding the region with $\sin^2 2\theta \geq 0.3$ and $\Delta m^2 \geq 0.05$ eV^2 at 3σ.

When combined with the Gallium data, we found a 1σ allowed region in the $(\sin^2 2\theta, \Delta m^2)$ plane, mainly coming from the Gallium data, around $\sin^2 2\theta \sim 0.1$ with $\Delta m^2 \gtrsim 1$ eV^2, with a parameter goodness-of-fit indicating a good compatibility of the data, and giving a hint in favor of neutrino oscillations compatible with the results presented in chapter 3.

The inclusion of the Gösgen data to the Bugey ones gives similar results to those we got from Bugey data alone (chapter 3). The effect of the Gösgen data is that of making weaker the hint in favor of neutrino oscillations, without changing the best fit values of the oscillation parameters. In this case, the parameter goodness-of-fit also indicates an acceptable compatibility of the data.

Then, the combined fit of Gallium, Bugey and Gösgen experiments has similar results to those of the Gallium+Bugey analysis. The best fit remains the same, with $\Delta m^2 \sim 1.9$ eV^2. We found a rather good compatibility of the data sets, and the results are consistent with the others presented here. Although the no oscillation hypothesis cannot be excluded, we found a hint in favor of neutrino oscillations with $0.03 \lesssim \sin^2 2\theta \lesssim 0.07$ and $\Delta m^2 \approx 1.9$ eV^2.

We have also studied the compatibility of cosmological experimental data with the hypothesis of a non thermal sterile neutrino with a mass in the range 0.1 – 10 eV and a contribution to $N_{\rm eff}$ smaller than one. We computed Bayesian confidence limits on different sets of parameters, adapted to the case of thermal relics, of non-resonantly produced sterile neutrinos *à la* Dodelson & Widrow (DW), or of generic parameters leading to nearly model-independent results. In each case, we performed a specific parameter extraction from scratch, in order to obtain reliable results assuming flat priors on the displayed parameters. For simplicity, we assumed that the masses of the three active neutrinos are negligible with respect to that of the sterile neutrino.

For a cosmological data set consisting in recent CMB and LSS data, as well as older but very conservative Lyman-α data, we found the conditional probability on the mass of a thermal relic given its temperature and the mass of a DW neutrino given its density suppression factor. These proabilities are such that if the fourth neutrino is a standard one (with $\Delta N_{\rm eff} = 1$), the limit on its mass is $m_s \lesssim 0.4$ eV at 2σ C.L. and $m_s \lesssim 0.9$ eV at 3σ C.L.

At the 3σ C.L., a mass $m_s = 1$ eV can be accommodated with the data provided that this neutrino is thermally distributed with $T_s/T_\nu^{\rm id} \lesssim 0.97$ ($T_\nu^{\rm id}$ being the temperature of neutrinos in the *instantaneous decoupling* limit), or is non-resonantly produced with $\Delta N_{\rm eff} \lesssim 0.9$. The bounds become dramatically tighter when the mass increases.

At the same confidence level, a mass of just $m_s = 2$ eV requires either $T_s/T_\nu^{\rm id} \lesssim 0.8$ or $\Delta N_{\rm eff} \lesssim 0.5$, while a mass $m_s = 5$ eV requires $T_s/T_\nu^{\rm id} \lesssim 0.6$ or $\Delta N_{\rm eff} \lesssim 0.2$.

Future neutrino oscillation experiments are expected to test the standard three-neutrino scenario with increasing accuracy. If anomalies and indications for sterile neutrinos tend to persist, it will be particularly useful to perform joint analysis of oscillation and cosmological data.

LIST OF TABLES

LIST OF FIGURES

BIBLIOGRAPHY

[1] H. Pietschmann, (2006), arXiv:physics/0603106.

[2] W. Pauli, Phys. Today **31N9**, 27 (1978), Open letter to the group of radioactive people at the Gauverein meeting in Tübingen, December 1930.

[3] G. Marx, Nucl. Phys. Proc. Suppl. **38**, 518 (1995).

[4] C. L. Cowan, F. Reines, F. B. Harrison, H. W. Kruse, and A. D. McGuire, Science **124**, 103 (1956).

[5] F. Reines, Rev. Mod. Phys. **68**, 317 (1996).

[6] B. Pontecorvo, Sov. Phys. JETP **6**, 429 (1957).

[7] S. L. Glashow, Nucl. Phys. **22**, 579 (1961).

[8] S. Weinberg, Phys. Rev. Lett. **19**, 1264 (1967).

[9] P. W. Higgs, Phys. Rev. Lett. **13**, 508 (1964).

[10] P. W. Higgs, Phys. Lett. **12**, 132 (1964).

[11] P. W. Higgs, Phys. Rev. **145**, 1156 (1966).

[12] T. W. B. Kibble, Phys. Rev. **155**, 1554 (1967).

[13] G. S. Guralnik, C. R. Hagen, and T. W. B. Kibble, Phys. Rev. Lett. **13**, 585 (1964).

[14] W.-M. Yao et al., Journal of Physics G **33**, 1 (2006).

[15] C. Giunti and C. W. Kim, *Fundamentals of Neutrino Physics and Astrophysics*, Oxford University Press, 2007.

[16] G. Altarelli and F. Feruglio, New J. Phys. **6**, 106 (2004), arXiv:hep-ph/0405048.

[17] S. F. King, Rept. Prog. Phys. **67**, 107 (2004), arXiv:hep-ph/0310204.

[18] A. Strumia and F. Vissani, (2006), arXiv:hep-ph/0606054.

[19] J. Lesgourgues and S. Pastor, Phys. Rept. **429**, 307 (2006), arXiv:astro-ph/0603494.

[20] M. C. Gonzalez-Garcia and M. Maltoni, Phys. Rept. **460**, 1 (2008), arXiv:0704.1800.

[21] G. Gelmini and E. Roulet, Rept. Prog. Phys. **58**, 1207 (1995), arXiv:hep-ph/9412278.

[22] S. Abe et al., Phys. Rev. Lett. **100**, 221803 (2008), arXiv:0801.4589.

[23] P. Adamson et al., Phys. Rev. **D77**, 072002 (2008), arXiv:0711.0769.

[24] C. Giunti, AIP Conf. Proc. **721**, 170 (2004), arXiv:hep-ph/0308206.

[25] S. Stoica, Phys. Atom. Nucl. **67**, 1786 (2004).

[26] S. M. Bilenky, S. Pascoli, and S. T. Petcov, Phys. Rev. **D64**, 053010 (2001), arXiv:hep-ph/0102265.

[27] S. M. Bilenky, S. Pascoli, and S. T. Petcov, Phys. Rev. **D64**, 113003 (2001), arXiv:hep-ph/0104218.

[28] J. D. Vergados, Phys. Rept. **361**, 1 (2002), arXiv:hep-ph/0209347.

[29] S. Pascoli, S. T. Petcov, and W. Rodejohann, Phys. Lett. **B558**, 141 (2003), arXiv:hep-ph/0212113.

[30] The NEMO experiment home page, http://nemo.in2p3.fr/.

[31] J. Argyriades, (2008), arXiv:0810.0248.

[32] E. Komatsu et al., (2008), arXiv:0803.0547.

[33] J. Dunkley et al., (2008), arXiv:0803.0586.

[34] G. Hinshaw et al., (2008), arXiv:0803.0732.

[35] S. Hannestad and G. Raffelt, JCAP **0404**, 008 (2004), arXiv:hep-ph/0312154.

[36] S. Hannestad, JCAP **0305**, 004 (2003), arXiv:astro-ph/0303076.

[37] P. Crotty, J. Lesgourgues, and S. Pastor, Phys. Rev. **D69**, 123007 (2004), arXiv:hep-ph/0402049.

[38] S. Hannestad and G. G. Raffelt, JCAP **0611**, 016 (2006), arXiv:astro-ph/0607101.

[39] S. Hannestad, (2007), arXiv:0710.1952.

[40] J. Lesgourgues, W. Valkenburg, and E. Gaztanaga, Phys. Rev. **D77**, 063505 (2008), arXiv:0710.5525.

[41] J. R. Kristiansen, O. Elgaroy, and H. Dahle, Phys. Rev. **D75**, 083510 (2007), arXiv:astro-ph/0611761.

[42] M. Fukugita and T. Yanagida, *Physics of Neutrino and Applications to Astrophysics*, Srpinger, 2003.

[43] M. Gell-Mann, P. Ramon, and R. Slansky, Complex spinors and unified theories, in *Supergravity*, edited by F. van Nieuwenhuizen and D. Freedman, page 315, North Holland, Amsterdam, 1979.

[44] R. N. Mohapatra and G. Senjanovic, Phys. Rev. Lett. **44**, 912 (1980).

[45] T. Yanagida, Horizontal symmetry and masses of neutrinos, in *Proceedings of the Workshop on the Baryon Number of the Universe and Unified Theories*, Tsukuba, Japan, 13-14 Feb, 1979.

[46] B. T. Cleveland et al., Astrophys. J. **496**, 505 (1998).

[47] Q. R. Ahmad et al., Phys. Rev. Lett. **89**, 011301 (2002), arXiv:nucl-ex/0204008.

[48] K. Eguchi et al., Phys. Rev. Lett. **90**, 021802 (2003), arXiv:hep-ex/0212021.

[49] L. Wolfenstein, Phys. Rev. **D17**, 2369 (1978).

[50] S. P. Mikheev and A. Y. Smirnov, Sov. J. Nucl. Phys. **42**, 913 (1985).

[51] M. Altmann et al., Phys. Lett. **B616**, 174 (2005), arXiv:hep-ex/0504037.

[52] J. N. Abdurashitov et al., J. Exp. Theor. Phys. **95**, 181 (2002), arXiv:astro-ph/0204245.

[53] J. P. Cravens et al., Phys. Rev. **D78**, 032002 (2008), arXiv:0803.4312.

[54] B. Aharmim et al., Phys. Rev. Lett. **101**, 111301 (2008), arXiv:0806.0989.

[55] G. Bellini et al., (2008), arXiv:0808.2868.

[56] Y. Fukuda et al., Phys. Lett. **B335**, 237 (1994).

[57] R. Becker-Szendy et al., Phys. Rev. Lett. **69**, 1010 (1992).

[58] Y. Fukuda et al., Phys. Rev. Lett. **81**, 1562 (1998), arXiv:hep-ex/9807003.

[59] H. Sekiya, (2008), For the Super-Kamiokande Collaboration, arXiv:0810.0595.

[60] M. H. Ahn et al., Phys. Rev. **D74**, 072003 (2006), arXiv:hep-ex/0606032.

[61] P. Adamson et al., Phys. Rev. Lett. **101**, 131802 (2008), arXiv:0806.2237.

[62] LEP, Phys. Rept. **427**, 257 (2006), arXiv:hep-ex/0509008.

[63] C. Amsler et al., Phys. Lett. **B667**, 1 (2008).

[64] R. R. Volkas, Prog. Part. Nucl. Phys. **48**, 161 (2002), arXiv:hep-ph/0111326.

[65] C. Athanassopoulos et al., Phys. Rev. Lett. **77**, 3082 (1996), arXiv:nucl-ex/9605003.

[66] A. Aguilar et al., Phys. Rev. **D64**, 112007 (2001), arXiv:hep-ex/0104049.

[67] A. A. Aguilar-Arevalo et al., Phys. Rev. Lett. **98**, 231801 (2007), arXiv:0704.1500.

[68] S. M. Bilenky, C. Giunti, W. Grimus, and T. Schwetz, Phys. Rev. **D60**, 073007 (1999), arXiv:hep-ph/9903454.

[69] M. Maltoni, T. Schwetz, M. A. Tortola, and J. W. F. Valle, Nucl. Phys. Proc. Suppl. **114**, 203 (2003), arXiv:hep-ph/0209368.

[70] S. M. Bilenky, C. Giunti, and W. Grimus, Neutrino oscillation experiments and the neutrino mass spectrum, in *Helsinki 1996, Neutrino physics and astrophysics*, edited by K. Enqvist et al., page 174, World Scientific, Sigapore, 1996, arXiv:hep-ph/9609343.

[71] M. Maltoni and T. Schwetz, Phys. Rev. **D76**, 093005 (2007), arXiv:0705.0107.

[72] M. Sorel, J. M. Conrad, and M. Shaevitz, Phys. Rev. **D70**, 073004 (2004), arXiv:hep-ph/0305255.

[73] J. N. Abdurashitov et al., Phys. Rev. **C73**, 045805 (2006), arXiv:nucl-ex/0512041.

[74] M. Laveder, Nucl. Phys. Proc. Suppl. **168**, 344 (2007), NOW 2006.

[75] C. Giunti and M. Laveder, Mod. Phys. Lett. **A22**, 2499 (2007), arXiv:hep-ph/0610352.

[76] C. Giunti and M. Laveder, Phys. Rev. **D77**, 093002 (2008), arXiv:0707.4593.

[77] R. N. Mohapatra and P. B. Pal, *Massive Neutrinos in Physics and Astrophysics*, volume 72 of *World Sientific Lecture Notes in Physics*, World Scientific Publishing Co. Pte. Ltd., 3rd edition, 2004.

[78] V. A. Kuzmin, Sov. Phys. JETP **22**, 1051 (1966).

[79] P. Anselmann et al., Phys. Lett. **B342**, 440 (1995).

[80] W. Hampel et al., Phys. Lett. **B420**, 114 (1998).

[81] W. Hampel et al., Phys. Lett. **B447**, 127 (1999).

[82] J. N. Abdurashitov et al., Phys. Rev. **C59**, 2246 (1999), arXiv:hep-ph/9803418.

[83] J. N. Abdurashitov et al., Phys. Rev. **C60**, 055801 (1999), arXiv:astro-ph/9907113.

[84] J. N. Abdurashitov et al., Phys. Rev. Lett. **83**, 4686 (1999), arXiv:astro-ph/9907131.

[85] J. N. Bahcall, Phys. Rev. **C56**, 3391 (1997), arXiv:hep-ph/9710491.

[86] M. Cribier et al., Nucl. Instr. Meth. **A378**, 233 (1996).

[87] M. Cribier et al., Nucl. Instr. Meth. **A265**, 574 (1988).

[88] J. N. Bahcall, P. I. Krastev, and E. Lisi, Physics Letters B **348**, 121 (1995), arXiv:hep-ph/9411414.

[89] J. F. Cavaignac et al., Phys. Lett. **B148**, 387 (1984).

[90] Y. Declais et al., Nucl. Phys. **B434**, 503 (1995).

[91] Y. Declais, Private Communication, 2008.

[92] W. Grimus and T. Schwetz, Eur. Phys. J. **C20**, 1 (2001), arXiv:hep-ph/0102252.

[93] M. Maltoni and T. Schwetz, Phys. Rev. **D68**, 033020 (2003), arXiv:hep-ph/0304176.

[94] Y. Declais et al., Proposal to search for neutrino vacuum oscillations to $\delta m^2 = 10^{-3}\mathrm{eV}^2$ using a 1 km baseline reactor neutrino experiment, The Chooz Collaboration, http://duphy4.physics.drexel.edu/chooz_pub/, 1993.

[95] M. Apollonio et al., Phys. Lett. **B466**, 415 (1999), arXiv:hep-ex/9907037.

[96] M. Apollonio et al., Eur. Phys. J. **C27**, 331 (2003), arXiv:hep-ex/0301017.

[97] M. Apollonio et al., Phys. Lett. **B420**, 397 (1998), arXiv:hep-ex/9711002.

[98] S. M. Bilenky, C. Giunti, and W. Grimus, Prog. Part. Nucl. Phys. **43**, 1 (1999), arXiv:hep-ph/9812360.

[99] M. C. Gonzalez-Garcia and Y. Nir, Rev. Mod. Phys. **75**, 345 (2003), arXiv:hep-ph/0202058.

[100] H. Kwon et al., Phys. Rev. **D24**, 1097 (1981).

[101] A. Houmada et al., Appl. Radiat. Isot. **46**, 449 (1995).

[102] Z. D. Greenwood et al., Phys. Rev. D **53**, 6054 (1996).

[103] H. W. Sobel, Private Communication, 2008.

[104] N. Baumann et al., The uci mobile neutrino experiment, in 8^{th} *Warsaw Simposium on elementary particle Physics*, edited by Z. Ajduk, page 143, 1985.

[105] G. Zacek et al., Phys. Rev. **D34**, 2621 (1986).

[106] J. L. Vuilleumier et al., Phys. Lett. **B114**, 298 (1982).

[107] V. Cirkel-Bartelt, Living Reviews in Relativity **11**, 2 (2008).

[108] S. Hannestad, New J. Phys. **6**, 108 (2004), arXiv:hep-ph/0404239.

[109] S. Hannestad, Prog. Part. Nucl. Phys. **57**, 309 (2006), arXiv:astro-ph/0511595.

[110] A. D. Dolgov, Phys. Rept. **370**, 333 (2002), arXiv:hep-ph/0202122.

[111] T. Kahniashvili, E. von Toerne, N. A. Arhipova, and B. Ratra, Phys. Rev. **D71**, 125009 (2005), arXiv:astro-ph/0503328.

[112] M. Tegmark et al., Phys. Rev. **D74**, 123507 (2006), arXiv:astro-ph/0608632.

[113] C. J. MacTavish et al., Astrophys. J. **647**, 799 (2006), arXiv:astro-ph/0507503.

[114] U. Seljak et al., Phys. Rev. **D71**, 103515 (2005), arXiv:astro-ph/0407372.

[115] G. L. Fogli et al., Phys. Rev. **D78**, 033010 (2008), arXiv:0805.2517.

[116] U. Seljak, A. Slosar, and P. McDonald, JCAP **0610**, 014 (2006), arXiv:astro-ph/0604335.

[117] F. De Bernardis, P. Serra, A. Cooray, and A. Melchiorri, Phys. Rev. **D78**, 083535 (2008), arXiv:0809.1095.

[118] G. Mangano, G. Miele, S. Pastor, and M. Peloso, Phys. Lett. **B534**, 8 (2002), arXiv:astro-ph/0111408.

[119] S. Pastor, (2008, Varenna, Lake Como, Italy), *Cosmological Probes of neutrino masses (Neutrinos in Cosmology)*, Presented at the International School of Physics "Enrico Fermi" CLXX Course: 'Measurements of Neutrino mass'.

[120] J. N. Abdurashitov et al., Astropart. Phys. **25**, 349 (2006), arXiv:nucl-ex/0509031.

[121] M. A. Acero, C. Giunti, and M. Laveder, Phys. Rev. **D78**, 073009 (2008), arXiv:0711.4222.

[122] A. A. Aguilar-Arevalo et al., Phys. Rev. **D78**, 012007 (2008), arXiv:0805.1764.

[123] A. Cuoco, J. Lesgourgues, G. Mangano, and S. Pastor, Phys. Rev. **D71**, 123501 (2005), arXiv:astro-ph/0502465.

[124] N. F. Bell, E. Pierpaoli, and K. Sigurdson, Phys. Rev. **D73**, 063523 (2006), arXiv:astro-ph/0511410.

[125] M. Cirelli and A. Strumia, JCAP **0612**, 013 (2006), arXiv:astro-ph/0607086.

[126] S. Dodelson, A. Melchiorri, and A. Slosar, Phys. Rev. Lett. **97**, 04301 (2006), arXiv:astro-ph/0511500.

[127] P. Di Bari, Phys. Rev. **D65**, 043509 (2002), arXiv:hep-ph/0108182.

[128] K. N. Abazajian, Astropart. Phys. **19**, 303 (2003), arXiv:astro-ph/0205238.

[129] G. F. Giudice, E. W. Kolb, A. Riotto, D. V. Semikoz, and I. I. Tkachev, Phys. Rev. **D64**, 043512 (2001), arXiv:hep-ph/0012317.

[130] G. Gelmini, S. Palomares-Ruiz, and S. Pascoli, Phys. Rev. Lett. **93**, 081302 (2004), arXiv:astro-ph/0403323.

[131] G. Gelmini, E. Osoba, S. Palomares-Ruiz, and S. Pascoli, (2008), arXiv:0803.2735.

[132] C. E. Yaguna, JHEP **06**, 002 (2007), arXiv:0706.0178.

[133] S. Khalil and O. Seto, JCAP **0810**, 024 (2008), arXiv:0804.0336.

[134] M. Kawasaki, K. Kohri, and N. Sugiyama, Phys. Rev. **D62**, 023506 (2000), arXiv:astro-ph/0002127.

[135] A. Boyarsky, J. Lesgourgues, O. Ruchayskiy, and M. Viel, (2008), arXiv:0812.3256.

[136] S. Dodelson and L. M. Widrow, Phys. Rev. Lett. **72**, 17 (1994), arXiv:hep-ph/9303287.

[137] S. Colombi, S. Dodelson, and L. M. Widrow, Astrophys. J. **458**, 1 (1996), arXiv:astro-ph/9505029.

[138] A. Lewis, A. Challinor, and A. Lasenby, Astrophys. J. **538**, 473 (2000), arXiv:astro-ph/9911177.

[139] A. Lewis and S. Bridle, Phys. Rev. **D66**, 103511 (2002), arXiv:astro-ph/0205436.

[140] D. N. Spergel et al., Astrophys. J. Suppl. **170**, 377 (2007), arXiv:astro-ph/0603449.

[141] C. L. Reichardt et al., (2008), arXiv:0801.1491.

[142] J. L. Sievers et al., (2005), arXiv:astro-ph/0509203.

[143] J. Hamann, S. Hannestad, G. G. Raffelt, and Y. Y. Y. Wong, JCAP **0708**, 021 (2007), arXiv:0705.0440.

[144] J. Hamann, S. Hannestad, A. Melchiorri, and Y. Y. Y. Wong, JCAP **0807**, 017 (2008), arXiv:0804.1789.

[145] P. Astier et al., Astron. Astrophys. **447**, 31 (2006), arXiv:astro-ph/0510447.

[146] M. Viel, M. G. Haehnelt, and V. Springel, Mon. Not. Roy. Astron. Soc. **354**, 684 (2004), arXiv:astro-ph/0404600.

[147] A. Boyarsky, J. Lesgourgues, O. Ruchayskiy, and M. Viel, (2008), arXiv:0812.0010.

[148] S. Hannestad, A. Mirizzi, and G. Raffelt, JCAP **0507**, 002 (2005), arXiv:hep-ph/0504059.

[149] S. Hannestad, A. Mirizzi, G. G. Raffelt, and Y. Y. Y. Wong, JCAP **0804**, 019 (2008), arXiv:0803.1585.